

ELECTRONIC STRUCTURE PERTURBATIONS OF PEROVSKITE MATERIALS  
PHOTOVOLTAIC APPLICATIONS

by  
THOMAS W. KASEL

A DISSERTATION

Presented to the Department of Chemistry and Biochemistry  
and the Graduate School of the University of Oregon  
in partial fulfillment of the requirements  
for the degree of  
Doctor of Philosophy

September 2020

DISSERTATION APPROVAL PAGE

Student: Thomas W. Kasel

Title: Electronic Structure Perturbations of Perovskite Materials

This dissertation has been accepted and approved in partial fulfillment of the requirements for the Doctor of Philosophy degree in the Department of Chemistry and Biochemistry by:

Jeffrey A. Cina

Chair

Christopher H. Hendon

Advisor

Mark C. Lonergan

Core Member

Benjamín J. Alemán

Institutional Representative

and

Kate Mondloch

Interim Vice Provost and Dean of the Graduate  
School

Original approval signatures are on file with the University of Oregon Graduate School.

Degree awarded September 2020

© 2020 Thomas W. Kasel

## DISSERTATION ABSTRACT

Thomas W. Kasel

Doctor of Philosophy

Department of Chemistry and Biochemistry

September 2020

Title: Electronic Structure Perturbations of Perovskite Materials

The necessity of implementing sustainable renewable energy sources to meet energy demands over the next century is rapidly becoming clearer. An overabundance of solar radiation hits the earth every day, a significant portion of which is not utilized by humans or by natural biological processes, and instead goes to waste. Solar energy is a unique form of renewable energy as its conversion efficiency is readily tunable and improvable through augmentation of the light absorbing material. 3<sup>rd</sup> generation solar materials, or emerging photovoltaic materials, have seen rapid progress towards improving efficiencies over the past half-century. Perovskites, a 3<sup>rd</sup> generation solar material, have demonstrated a 20 % increase in efficiency in under a decade and are currently a propitious solution to current and future energy demands. Although perovskites boast favorable electronic properties for superior photovoltaic performance (such as light effective masses, long charge carrier diffusion lengths, a resistance to defects, and fabrication using roll-to-roll processing techniques), the best performing devices suffer from several instabilities (heat, moisture, and redox reactivity when illuminated in the presence of O<sub>2</sub>) as well as the obviously health concern of their lead based components. These instabilities result in decreased photovoltaic performance as the structure degrades. It is generally accepted that the organic motifs in the perovskite organic-inorganic hybrid champion devices are responsible for their instabilities. This thesis uses computational techniques (primarily density function theory) to investigate

the electronic properties of perovskites to offer plausible new solutions and implications of current solutions aimed at addressing the moisture instability of these photovoltaic materials. Additionally, this thesis investigates the electronic properties of the degraded lattice, as well as exotic new properties of a novel architecture in the perovskite family.

This dissertation includes previously published and unpublished co-authored material.

## CURRICULUM VITAE

NAME OF AUTHOR: Thomas W. Kasel

### GRADUATE AND UNDERGRADUATE SCHOOLS ATTENDED:

University of Oregon, Eugene, OR, USA  
California Lutheran University, Thousand Oaks, CA, USA  
Moorpark College, Moorpark, CA, USA

### DEGREES AWARDED:

Doctor of Philosophy, Chemistry, 2020, University of Oregon  
Master of Science, Chemistry, 2017, University of Oregon  
Bachelor of Science, Chemistry, 2016, California Lutheran University  
General Associate Arts Degree, 2011, Moorpark College

### AREAS OF SPECIAL INTEREST:

Computational Chemistry  
Density Functional Theory (DFT)  
Ab Initio Molecular Dynamics (AIMD)  
  
Photovoltaics  
Perovskites  
  
Electronic Properties of Semiconductors

### PROFESSIONAL EXPERIENCE:

Graduate Employee - Hendon Lab, University of Oregon, 2017-2020  
Graduate Employee, Physical Chemistry Lab, University of Oregon, 2016  
Graduate Employee, General Chemistry Lab, University of Oregon, 2016-2019

### PUBLICATIONS:

T. W. Kasel, A. T. Murray, and C. H. Hendon, *J. Phys. Chem. C*, 2018, **122**, 2041  
T. W. Kasel and C. H. Hendon, *J. Mater. Chem. C*, 2018, **6**, 4765  
T. W. Kasel, Z. Deng, A. M. Mroz, C. H. Hendon, K. T. Butler, and P. Canepa, *Chem. Sci.*, 2019, **10**, 8187  
G. Skorupskii, B. A. Trump, T. W. Kasel, C. M. Brown, C. H. Hendon, and M., Dincă, *Nat. Chem.*, 2020, **12**, 131  
D. M. Hamann, D. Bardgett, S. R. Bauers, T. W. Kasel, A. M. Mroz, C. H. Hendon, D. L. Medlin, and D. C. Johnson, *Chem. Mater.*, 2020, **13**, 5802  
T. W. Kasel and C. H. Hendon, *J. Mater. Chem. A*, 2020, \*In Preparation

## ACKNOWLEDGEMENTS

I would like to take this space to thank and acknowledge those who have helped me along the way. I want to thank my family for all their unconditional support and unwavering commitment. I thank Dr. Hendon for his mentoring and guidance in this processes and I'd like to thank Dr. Butler, Dr. Scanlon, and Dr. Canepa for their educational guidance. I thank Dr. Cina, Dr. Lonergan, and Dr. Boettcher for their words of wisdom and mentorship. I thank my colleagues for their intellectual discussions and the Hendon Materials Simulations group for their camaraderie. I thank my best friend Bradley Allen for being a void into which I can scream my frustration. I thank my four fur children, Houdini (R.I.P.), Tanner, Franky, and Chester for their unconditional love. And I would like to thank the University of Oregon for this opportunity.

## TABLE OF CONTENTS

Chapter	Page
I INTRODUCTION	1
I.1 Solar Energy . . . . .	3
I.1.1 Converting Light-to-Electricity and the Shockley-Queisser Limit . . . . .	5
I.2 Solar Devices . . . . .	9
I.2.1 First Generation Solar Cells . . . . .	10
I.2.2 Second Generation Solar Cells . . . . .	11
I.2.3 Third Generation Solar Cells . . . . .	12
I.3 Perovskites . . . . .	14
I.3.1 Beyond the Oxide: the Halide analog . . . . .	15
I.3.2 Perovskites in Photovoltaics: Promising Properties . . . . .	17
I.3.3 Factors Limiting Commercialization: Lead . . . . .	22
I.3.4 Factors Limiting Commercialization: Structural Instability . . . . .	23
I.4 Investigating Perovskites . . . . .	26
II SOLVING CHEMICAL PROBLEMS WITH COMPUTERS	28
II.1 Fundamentals of Electronic Structure: Schrödinger's Equation . . . . .	30
II.1.1 The Born-Oppenheimer Approximation . . . . .	32
II.1.2 The Method of Hartree-Fock and the Slater Determinate . . . . .	33
II.2 Density Functional Theory . . . . .	34
II.2.1 Functionals . . . . .	35
II.2.2 Basis Sets . . . . .	38
II.3 The Solid State and Periodic Imaging of the Infinite Solid . . . . .	39
II.3.1 Reciprocal Space . . . . .	41
II.3.2 System Optimization and the Variation Principle . . . . .	44
II.4 Tools to Analyze Solid State Properties . . . . .	46
II.4.1 Band Structure and Density of States . . . . .	46
II.4.2 Phonons . . . . .	48

Chapter	Page
II.4.3 Nonlinear Optics . . . . .	53
III CYCLOPROPENIUM (C <sub>3</sub> H <sub>3</sub> ) <sup>+</sup> AS AN AROMATIC ALTERNATIVE A-SITE CATION FOR HYBRID HALIDE PEROVSKITE ARCHITECTURES	57
III.1 Bridge & Introduction . . . . .	57
III.2 Results and Discussion . . . . .	62
III.3 Conclusions . . . . .	65
III.4 Computational Methods . . . . .	66
IV ELECTRONIC IMPLICATIONS OF ORGANIC NITROGEN LONE PAIRS IN LEAD IODIDE PEROVSKITES	68
IV.1 Bridge & Introduction . . . . .	68
IV.2 Results and Discussion . . . . .	70
IV.3 Conclusion . . . . .	73
IV.4 Computational Methods . . . . .	74
V A TYPE I HETEROINTERFACE BETWEEN AMORPHOUS PbI <sub>2</sub> OVERLAYERS ON CRYSTALLINE CsPbI <sub>3</sub> : OPPORTUNITIES FOR NANOCRYSTALS?	75
V.1 Bridge & Introduction . . . . .	75
V.2 Results and Discussion . . . . .	77
VI METAL-FREE PEROVSKITES FOR NON-LINEAR OPTICAL MATERIALS	81
VI.1 Bridge & Introduction . . . . .	81
VI.2 Results . . . . .	84
VI.2.1 Structure of ferroelectric metal-free perovskites . . . . .	84
VI.2.2 Birefringence activity of Metal-free Perovskites . . . . .	85
VI.2.3 NLO response in Metal-free Perovskites . . . . .	87
VI.3 Discussion . . . . .	90
VI.4 Conclusions . . . . .	92
VI.5 Linear and non-linear optic effects . . . . .	93
VI.6 First-principles calculations . . . . .	94
VII CONCLUSION	96
VII.1 Future Directions . . . . .	98

Chapter	Page
A APPENDIX	102
REFERENCES CITED	111

## LIST OF FIGURES

Figure	Page
<p>1.0.1 Depiction of the average global land and sea air temperature since 1900 to the turn of the current millennium. Projections suggest that at the current rate of temperature increase, 0.2°C (0.36 °F) per decade, average summer temperatures will reach 32 °C (89.6 °F) to 54 °C (129.2 °F) worldwide by the year 3000. Notable scientific achievements relevant to topics and discussion contained within this thesis, alongside the foundation of the IPCC and the Paris Agreement, are labeled. . . . .</p>	2
<p>1.0.2 Solar irradiance spectrum of our sun. The magnitude of radiation that hits the earth's upper atmosphere is greater than the radiation that makes it to sea level. A fraction of incoming light is reflected and absorbed by the ozone, atmospheric water, and other high altitude particulates in the atmosphere while passing through the atmosphere towards sea level. . .</p>	3
<p>1.1.1 a) Basic example of a solar cell architecture. b) Simplified depiction of the photovoltaic effect. Light is absorbed by an electron in the active material (A) promoting it to an unfilled orbital of higher energy. The electron is then transported (B) to an unfilled orbital of lower energy in a connecting transport material and then finally to the drain where it goes to power a load (C). The electron then returns to the solar cell at the opposite drain (D) where it combines with a hole. The amount of energy made available by the solar cell to perform external work is the difference in potential of the two drains. The difference in energy between the highest filled orbital and the lowest unfilled orbital in the active material is the band gap (<math>E_g</math>). . . . .</p>	5
<p>1.1.2 The maximum achievable efficiency for a single junction solar cell as determined by the Shockley-Queisser limit (dashed line). Notable achievements in solar materials development are shown. The range of band gaps is given for materials with a variable band gap. . . . .</p>	7

Figure	Page
1.1.3a) Simulated short circuit current density ( $J_{SC}$ , red) and open circuit voltage ( $V_{OC}$ , blue) obtainable as dependent upon a materials band gap. Both a larger $J_{SC}$ and $V_{OC}$ lead to higher maximum efficiency. b) Various losses of the energy contained in the solar spectrum depending on the band gap of the absorbing material. . . . .	8
1.3.1 Various phases of $ABO_3$ and $ABX_3$ perovskites. In general, as temperature increases most perovskite lattices transition from orthorhombic to tetragonal and finally to cubic. . . . .	15
2.0.1 Relationship between system size and approximations made to atomic behavior. High level methods such as first principles quantum chemistry (bottom left) generally make few approximations to atomic behavior and represent atomic characteristics fairly well, for example, bonding. Moving to the top right systems include more atoms and can represent larger motifs, such as proteins, but trade off accuracy of atomic descriptions. For example bonds in proteins are treated as a rigid spring and follow Hooke's law instead of being comprised of electrons. . . . .	29
2.3.1a) Translation of the model, blue, along the lattice vectors, red and green, giving rise to periodic images, grey, returning the infinite solid. b) Translation of the triangular model gives rise to void space, colorless, and thus the model cannot be periodic. Redrawing the boundaries of the cell allows for the void space to be removed, making the model periodic. . . .	41
2.3.2a) Bonding and anti-bonding configurations for a 1D chain of s-orbitals. b) Corresponding band structure of the crystallographic unit cell containing two s-orbitals. . . . .	43

- 2.3.3 General optimization routine utilized to find the ground state geometry of a supplied model. The user starts by generating a model (coordinates, basis, list of program instructions, etc.), then an initial guess of the wavefunction is generated. This wavefunction is converged iteratively, then the forces on each atom are calculated. If the forces have not been minimized below a stipulated threshold, the process is repeated after the geometry is updated as guided by the calculated forces. Once the atomic forces are converged, the unit cell convergence is checked. If it is unconverged, the lattice parameters are updated, and the process repeats until unit cell convergence is met, at which point the process is complete and a ground state geometry is obtained. . . . . 44
- 2.3.4 Depiction of the variational principle. For a given state, the wavefunction is varied and the expectation value of the new state is calculated. If the energy of the new state is lower than the previous, it becomes the new ground state. This is continued until the change in energy is below a stipulated threshold. At this point, it is expected that the recovered wavefunction with the lowest energy is similar to that of the true ground state. . . . . 45
- 2.4.1 a) Cesium lead iodide ( $\text{CsPbI}_3$ ) shown in its cubic phase. b) Band structure and density of states for cubic  $\text{CsPbI}_3$  calculated using the HSE06 (PBE+43% HF) hybrid functional and spin-orbit coupling effects. The density of states is calculated at the high symmetry points only. c) High symmetry points of space group  $P_{m-3m}$  (#221) within the 1<sup>st</sup> Brillouin zone. Note that the nomenclature for the symmetry elements and high-symmetry k-points are taken from the Bilbao database of lattice symmetry and k-points. . . . . 47

Figure	Page
2.4.2a) Cubic (CH <sub>3</sub> NH <sub>3</sub> )PbI <sub>3</sub> . b) Phonon band structure and phonon density of states of (CH <sub>3</sub> NH <sub>3</sub> )PbI <sub>3</sub> . The negative phonon frequencies correspond to the phase transition of cubic (CH <sub>3</sub> NH <sub>3</sub> )PbI <sub>3</sub> to phases more stable at lower temperatures. The negative phonon frequency at the <i>X</i> q-point is representative of the phase transition depicted in (a) by the arrows. c) Space group for cubic (CH <sub>3</sub> NH <sub>3</sub> )PbI <sub>3</sub> . While technically (CH <sub>3</sub> NH <sub>3</sub> )PbI <sub>3</sub> has the <i>P1</i> symmetry (space group # 1), its space group is approximated as its parent structures space group <i>P<sub>m-3m</sub></i> (# 221). Typically structures that will undergo phonon calculations are converged with a very strict k-grid, force convergence criteria, and total energy convergence criteria; Here, these criteria were loosened to provide a simple but representative example. . . . .	49
2.4.3a) Second harmonic generation where two photons of the same frequency combine to generate a new photo of double the original frequency. b) Sum frequency generation where two photons of different frequencies generate a new photon who's frequency is the sum of the original two photon frequencies. c) Difference frequency generation where two photons of different frequency generate a new photon who's frequency is the difference of the original two photo frequencies. . . . .	54
3.1.1 Highlight of elements with appropriate charge to form the ABX <sub>3</sub> perovskite structure. Only elements with a suitable main oxidation state are highlighted. It can be seen that there is a limited number of combinations without turning to organic molecules. . . . .	58
3.1.2 Guide to perovskite formation when tolerance factors are a) < 0.8, b) 0.8 ≤ <i>tf</i> ≤ 1.0, or c) > 1.0. Arrows show the general forces felt by the nearest neighbor atoms for when the A-site cation is of incompatible size. . . . .	59
3.1.3a) Tolerance factors for commonly studied perovskites structures, including one suggested by our work (C <sub>3</sub> H <sub>3</sub> <sup>+</sup> ) for both Pb and Sn based halide perovskites. b) Limited lists of various charge appropriate components. . . . .	60
3.1.4 Some of the reported organic A-site cations found in PbI <sub>3</sub> <sup>-</sup> based perovskites. The cyclopropenium cation differs from the other cations as it is aprotic. . . . .	61

- 3.2.1(a) The electronic band structure and density of states of  $(C_3H_3)PbI_3$  as computed with HSE06sol+SOC (PBEsol with 43% HF exchange and spin-orbit coupling). (b,c) The conduction band minimum and valence band maximum orbital contributions at the R-point. Electron density isosurface is plotted in salmon at  $0.006 e/\text{\AA}^3$ . Density of states are plotted for special k-points, only\* . . . . . 63
- 3.2.2(a) Seven displacements of the A-site cation. The trajectory was obtained from an *ab initio* molecular dynamic simulation triplicate. (b) Corresponding energies of displacement suggest that  $C_3H_3^+$  ions are at least translation mobile at room temperature. (c) Examination of the phonon band structure shows no negative modes at  $\Gamma$ , and the usual negative modes - emphasized in the inset of panel c - associated with  $PbI_3^-$  cage deformation when sampling in the R-vector, similar to that observed in  $(CH_3NH_3)PbI_3$ . . . . . 64
- 4.1.1a) The organic motif in protic organohalide perovskites (orange) reacts with water to form methylamine,  $CH_3NH_2$  evaporates at low temperatures, forming  $PbI_2$  and residual HI. b) The addition of a hydrophobic passivation agent at either external device faces or at grain boundaries is thought to improve moisture stability. They also act as a physical barrier to imminent water. Lead and iodine are shown in grey and eminece respectively. . . . . 69
- 4.2.1a) The 3D perovskite  $PbI_3^-$  cage features similar inorganic connectivity to the 2D  $PbI_4^{2-}$  counterpart. The 2D dangling iodides are analogous to the (100), (010), and (001) surfaces of the 3D material. b) The electronic band structure of the 3D material features large band curvature in the conduction band, associated with delocalized Pb *p*-states. The valence band has less dispersion, and is comprised of a combination of Pb *s*- and I *p*-states. The reduction in Pb-I dimensionality in the 2D perovskite results in reduced curvature in both band extrema. Special points map to *Pm-3m* and *Pbca* space groups for the 3D and 2D structures, respectively. . . . . 71

Figure	Page
4.2.2 Electronic band structures and density of states (DOS) of 2D perovskites with their corresponding organic cations. The $\mathbf{k}$ -vectors map to space group $Pbca$ , and the first Brillouin zone is shown. All electronic structures were computed using PBEsol+SOC. DOS is reported for $\Gamma$ only. Organic molecules containing nitrogen lone pairs show nitrogen DOS near the VBM, which grows with increasing concentration of tertiary nitrogen.	73
5.1.1 Band edge diagram for $CsPbI_3$ and $PbI_2$ . The VBM of $PbI_2$ lies within the gap of $CsPbI_3$ suggesting that its existence results in mid gap states. The work function for $CsPbI_3$ was obtained from literature. . . . .	76
5.2.1 a) Models used to recover the electronic effects of the decomposition of a pristine $PbI_3^-$ lattice to $\alpha$ - $PbI_2$ . b) $\alpha$ - $PbI_2@CsPbI_3$ and its charge density calculated at the valence band maximum and conduction band minimum. Charge densities were plotted with an isosurface value of $10^{-5} e^-/\text{\AA}^3$ . c) Fermi aligned density of states were calculated using HSE06sol+SOC (PBEsol + 43% Hartree-Fock exchange + spin-orbit coupling). The $\alpha$ - $PbI_2$ region has an $\sim 950$ meV and an $\sim 1250$ meV energy barrier associated with hole transport and electron transport from the core to the surface, respectively. . . . .	78
6.1.1 Polyhedra representation of a metal-free $ABX_3$ -type perovskite, where $A$ can be one of the four organic cations (also shown by the red ball), $B$ is $NH_4^+$ (grey ball) and $X$ the halide ion, i.e. $Cl^-$ , $Br^-$ and $I^-$ (purple balls). The nature of the $A$ cation is also shown. . . . .	82
6.2.1 Computed birefringence $\Delta n$ and $2V$ angle of metal-free perovskites at their experimental volume and lattice constants. $\Delta n$ is plotted on the radial axis and using the colour-bar, with red indicating positive $\Delta n$ . Values of $n$ are given in Table S3 of the SI. The $2V$ angles provide information about the nature of the birefringence in biaxial crystals. . . . .	85

Figure	Page
6.2.2 Computed static $d_{\text{norm}}$ (colour-bar) as function of the band gap (x-axis, eV) and average dielectric constant (y-axis) of the metal-free perovskites at the experimental volume. The $\epsilon$ values (in the static limit) computed for the metal-free perovskites are normalised against the $\text{LiNbO}_3$ ( $\sim 4.39$ ). Similarly, the values of $d_{\text{norm}}$ are rescaled to that of $\text{LiNbO}_3$ ( $\sim 17.91$ pm/V). The space group of each structure is also reported. . . . .	86
6.3.1 <b>a</b> Total and projected density of states of ODABCO- $\text{NH}_4\text{Br}_3$ , MDABCO- $\text{NH}_4\text{Br}_3$ and MDABCO- $\text{NH}_4\text{I}_3$ obtained with PBEsol0-D3. The red line (dash) is the Fermi energy, which is set at the top of the valence band of each material. <b>b</b> Variance of dipole moment for DABCO cations substituted with a number of organic groups (functions). . . . .	90

## LIST OF TABLES

Table	Page
<p>6.2.1 Computed static <math>d_{ijk}</math> components of the <math>\chi^{(2)}</math> tensor and their norm <math>d_{\text{norm}}</math> (in pm/V) of the metal-free perovskites at the experimental volumes. Spg. is the space group. . . . .</p>	88
<p>A.1 Tolerance factors for <math>\text{ABF}_3</math> perovskites. Tolerance factors were calculated using the Shannon radii. Combinations that theoretically result in a distorted perovskite structure (<math>\text{tf} &lt; 0.8</math>) are highlighted in yellow. Combinations that theoretically result in a cubic perovskite structure (<math>0.8 &lt; \text{tf} &lt; 1.0</math>) are highlighted in green. Combinations that theoretically do not result in a perovskite structure (<math>\text{tf} &gt; 1.0</math>) are highlighted in red. A-site cation radii were chosen as the smallest coordinated single charge ion whereas the B-site cation radii were chosen as the 6-coordinate radii. Not all combinations have been synthetically realized. . . . .</p>	103
<p>A.2 Tolerance factors for <math>\text{ABCl}_3</math> perovskites. Tolerance factors were calculated using the Shannon radii. Combinations that theoretically result in a distorted perovskite structure (<math>\text{tf} &lt; 0.8</math>) are highlighted in yellow. Combinations that theoretically result in a cubic perovskite structure (<math>0.8 &lt; \text{tf} &lt; 1.0</math>) are highlighted in green. Combinations that theoretically do not result in a perovskite structure (<math>\text{tf} &gt; 1.0</math>) are highlighted in red. A-site cation radii were chosen as the smallest coordinated single charge ion whereas the B-site cation radii were chosen as the 6-coordinate radii. Not all combinations have been synthetically realized. . . . .</p>	105

Table	Page
<p>A.3 Tolerance factors for <math>ABBr_3</math> perovskites. Tolerance factors were calculated using the Shannon radii. Combinations that theoretically result in a distorted perovskite structure (<math>tf &lt; 0.8</math>) are highlighted in yellow. Combinations that theoretically result in a cubic perovskite structure (<math>0.8 &lt; tf &lt; 1.0</math>) are highlighted in green. Combinations that theoretically do not result in a perovskite structure (<math>tf &gt; 1.0</math>) are highlighted in red. A-site cation radii were chosen as the smallest coordinated single charge ion whereas the B-site cation radii were chosen as the 6-coordinate radii. Not all combinations have been synthetically realized. . . . .</p>	107
<p>A.4 Tolerance factors for <math>ABl_3</math> perovskites. Tolerance factors were calculated using the Shannon radii. Combinations that theoretically result in a distorted perovskite structure (<math>tf &lt; 0.8</math>) are highlighted in yellow. Combinations that theoretically result in a cubic perovskite structure (<math>0.8 &lt; tf &lt; 1.0</math>) are highlighted in green. Combinations that theoretically do not result in a perovskite structure (<math>tf &gt; 1.0</math>) are highlighted in red. A-site cation radii were chosen as the smallest coordinated single charge ion whereas the B-site cation radii were chosen as the 6-coordinate radii. Not all combinations have been synthetically realized. . . . .</p>	109

## CHAPTER I

### INTRODUCTION

According to the United Nation's Intergovernmental Panel on Climate Change (IPCC), in 2017 the average air and sea temperature was 1.5 °C (2.7 °F) higher than pre-industrial temperatures of 1850-1900.<sup>1</sup> The IPCC further estimates that humans contributed 1 °C (1.8 °F, 66 %) of the 1.5 °C increase and that temperatures will continue to rise at a rate of 0.2 °C (0.36 °F) per decade, depicted in Figure 1.0.1. Over the next century, if temperatures continue to rise at predicted rates, areas near the equator will become uninhabitable (or at least very uncomfortable) for human life. While earth has been in its natural heating cycle for the last 20,000 years, evidence continues to mount that human consumption of organic based fuels (oil and coal) have a nonnegligible impact on the climate of the planet.

Regardless of the human impact on climate change, these naturally occurring organic fuel sources are nonrenewable on the time scale of human consumption. As a result, at the current rate of consumption, oil reserves will dwindle by 2052 and coal by 2090.<sup>2</sup> Therefore, there is a clear and present deadline to integrate, maximize, and optimize a nation wide (and worldwide) renewable energy grid.

Renewable energy sources include geothermal, hydro, nuclear,\* wind, and solar. Geothermal and hydropower, respectively, are geographically limited to areas with geothermal vents and water sources with strong enough currents capable of generating electricity at a rate that justifies upkeep costs. Historically, the exploitation, or lack-there-of, of nuclear power generation has been driven by political (and thus economic) concerns. Therefore, nuclear energy as a longer term solution and main component of a renewable energy grid is thus unlikely. While currently wind turbines are more efficient than solar energy generation, improvement in their efficiency is restricted to their engineering and design and thus, is limited. Solar, on the other hand,

---

\*While nuclear fuel rods are technically a limited commodity, the energy contained within far exceeds that of other nonrenewable sources (over six orders of magnitude more energy kg-per-kg with coal). In this regard, if nuclear energy gained and maintained a sizable foothold in energy generation, it is highly likely that by the time nuclear resources dwindle, other renewable sources will be trivial to integrate due to technological advances.

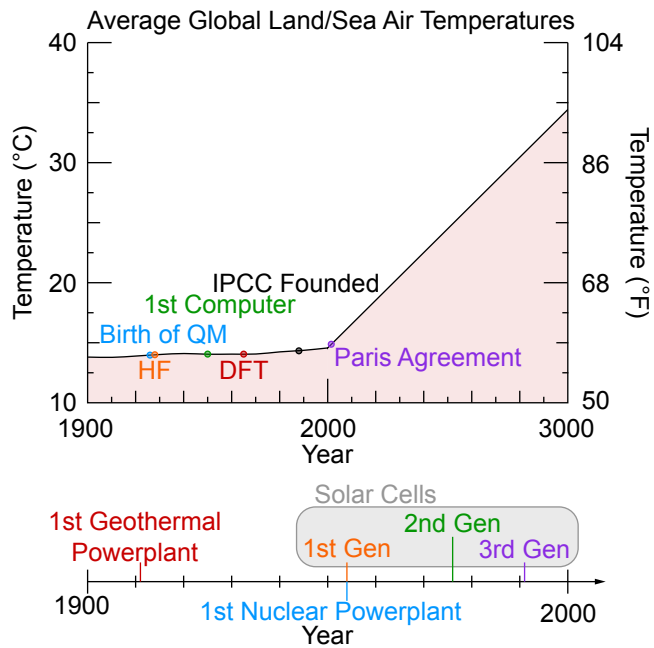


**Figure 1.0.1** Depiction of the average global land and sea air temperature since 1900 to the turn of the current millennium. Projections suggest that at the current rate of temperature increase, 0.2°C (0.36 °F) per decade, average summer temperatures will reach 32 °C (89.6 °F) to 54 °C (129.2 °F) worldwide by the year 3000. Notable scientific achievements relevant to topics and discussion contained within this thesis, alongside the foundation of the IPCC and the Paris Agreement, are labeled.

century.

At the current day, the National Renewable Energy Laboratory (NREL, a leading world expert in solar energy) calculates that more solar energy hits the earth each hour than is necessary to meet the global population’s energy demand for an entire year.<sup>4</sup> As seen by the solar radiation spectrum in Figure 1.0.2, of the light that hits the earth’s surface, 47.28 % comes directly from the visible portion of the solar spectrum. When including the available data for the near UV region, this number increases to ~ 50 % (49.52 %). Furthermore, silicon solar cells can absorb wavelengths up to approximately 1100 nm, in the near IR region, allowing them to absorb up to 78.40 % of the solar spectrum. It is thus readily calculated that there is approximately 22 % of the solar spectrum not utilizable by these silicon solar devices. For devices with band gaps larger than silicon, the portion of the solar spectrum not utilizable is even greater. To make matters worse, the calculations presented here have assumed that 100 % of the energy contained in each photon is directly converted to a usable form of energy,

at perfection, has the capability of bearing the burden of the world’s energy needs. In 2006, Sandia National Laboratories projected that at theoretical potential, the light harvestable from the sun alone would be more than double the projected need in 2100 (89,000 TW generated to 43,000 TW consumed).<sup>3</sup> It is therefore readily obvious that development of photon harvesting materials will play a large and important co-operational role (alongside other renewable energy sources) in generating a sustainable renewable energy grid before the turn of the

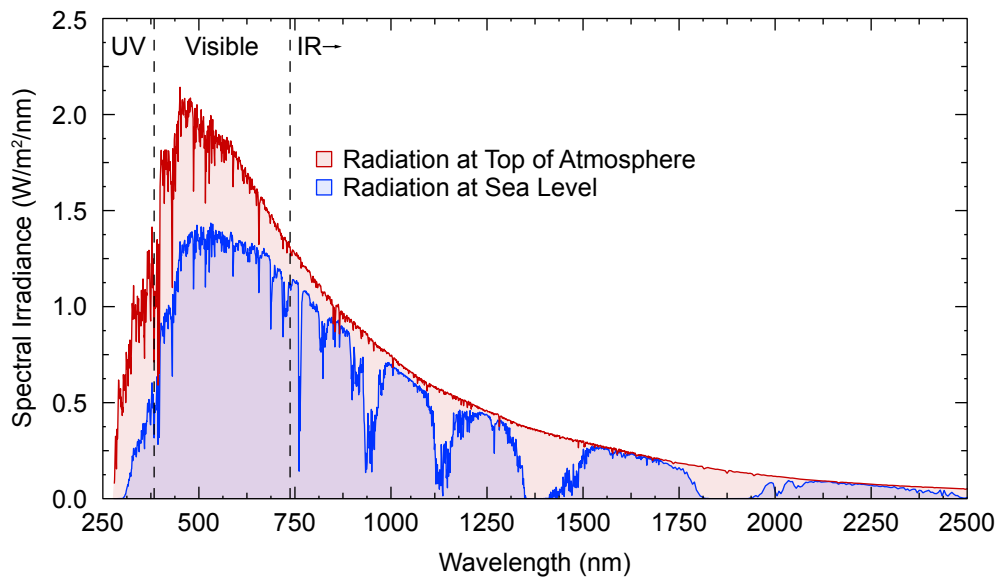


**Figure 1.0.2** Solar irradiance spectrum of our sun. The magnitude of radiation that hits the earth's upper atmosphere is greater than the radiation that makes it to sea level. A fraction of incoming light is reflected and absorbed by the ozone, atmospheric water, and other high altitude particulates in the atmosphere while passing through the atmosphere towards sea level.

and no losses have occurred. In reality, depending on the band gap of the material, much of the energy contained in high energy photons, such as those in the UV region, get lost through processes such as heat generation. As such, it is imperative to maximize the efficiency at which we convert sunlight to electricity. It is in this aspect that solar energy is unique compared to all other forms of energy generation; The efficiency of a high quality manufactured solar device depends more on the inherent electrical properties of the light absorbing material than on the engineering of the device as a whole.

### I.1 Solar Energy

The primary process of generating electricity in almost all modern forms of power generation involves the transformation of kinetic energy into stored potential energy through the rotation of a turbine. The turbine exploits the relationship between magnetism and current, electromagnetic induction, generating electricity by rotating a coiled conductive wire about a magnetic link (such as a piece of magnetized iron). The motion of the wire about the magnetic link pushes the electrons down the stream of the field (through the wire), where they are shuttled off to do work in appliances such as televisions, computers, phones, lights, etc. The trick is then to find an efficient way

to rotate the conductive wire about the magnetic link. This is typically accomplished by attaching long, tilted blades around a drive shaft (which is in-turn connected to the coiled wire) and using a physical object to push the blades much like the wind pushes the blades of a pinwheel. One of the most readily available physical objects to impart force on the blades is water, in both its liquid and gaseous forms. The idea of using water to do work is not a novel one, and historical examples are readily seen through watermills grinding grain using a nearby river. Burning coal, gas, or oil (hydrocarbon combustion) generates heat which is transferred to a body of water, bringing it to its boiling point, converting the liquid water to gaseous water (steam); The motion of the rising or pressurized steam is then used to turn a turbine. In geothermal, steam (or very hot water later vaporized through sudden pressure changes) produced deep within the earth using natural heat sources, is brought to the earth surface which again, is used to turn a turbine. Nuclear energy utilizes the immense amount of energy generated in nuclear fission to heat a pool of water, yet again generating steam to turn a turbine. Hydropower simply uses naturally moving liquid water in rivers and streams to push a turbine without the generation of heat. Wind, in a unique fashion, forgoes the use of water and instead uses wind currents to push the blades of the turbine, generating electricity. Solar is the only major form of energy generation that does not generate electricity through pushing the blades of a turbine. It is for this exact reason that maximization of electricity generation in solar cells is unique compared to every other electricity generating process, as previous stated.

Maximization of solar device efficiency does not solely depend upon the engineering of the device architecture as it does in other electricity generating process; For example the mechanical design of the turbine and its placement in a water stream. Instead it depends upon the intrinsic electrical properties of the materials contained in the solar device. No matter how well built a solar cell may be, even if it is exposed to high sunlight levels at all hours of the day, if the intrinsic electrical properties of the light absorber results in a poor photon-to-electricity conversion efficiency, then very little electricity will be generated. This is not necessarily a problem for all other forms of electricity generation, as long as the magnetic link generates a magnetic field and the device doesn't break, electricity will be generated when the device is placed in an appropriate location. As such, solar energy allows for a wide array of materials to be tested and utilized in electricity generation, allowing problems and shortcomings to be addressed in a myriad of ways. Therefore, it should not be surprising if over the next

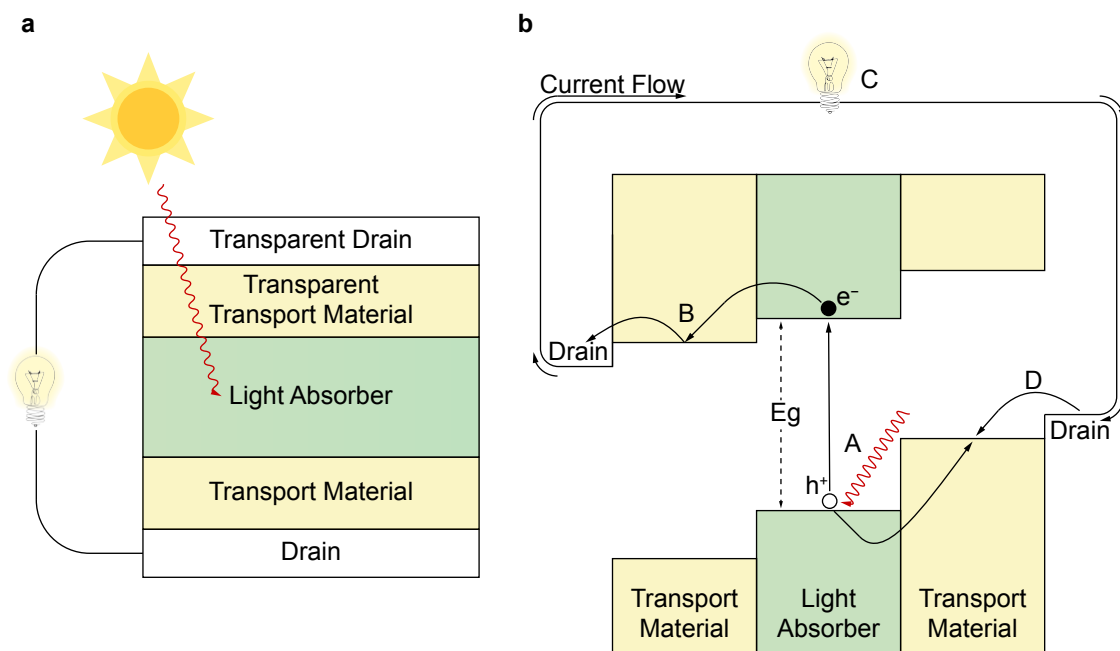


**Figure 1.1.1** a) Basic example of a solar cell architecture. b) Simplified depiction of the photovoltaic effect. Light is absorbed by an electron in the active material (A) promoting it to an unfilled orbital of higher energy. The electron is then transported (B) to an unfilled orbital of lower energy in a connecting transport material and then finally to the drain where it goes to power a load (C). The electron then returns to the solar cell at the opposite drain (D) where it combines with a hole. The amount of energy made available by the solar cell to perform external work is the difference in potential of the two drains. The difference in energy between the highest filled orbital and the lowest unfilled orbital in the active material is the band gap ( $E_g$ ).

half-century several chemically unique solar cells appear in consumer markets, giving customers a smorgasbord of device options to suit their individual needs. Such a scenario should be readily welcomed.

### 1.1.1 Converting Light-to-Electricity and the Shockley-Queisser Limit

The conversion of photons-to-electricity is highly dependent upon the inherent properties of the light absorbing material. A basic example of a solar cell architecture is presented in Figure 1.1.1a where a light absorbing material is sandwiched between two transport materials which are sandwiched between two drains (also referred to as electrodes) that are connected to an external load such as a light bulb. The process of using light to generate electricity is called the photovoltaic effect. In the photovoltaic effect, depicted in Figure 1.1.1b, a negatively charged electron in the light absorbing material absorbs a photon of light (A), promoting it to an unfilled orbital of higher energy. A positively charged hole, or lack of an electron, is left behind in the electrons place. The electron-hole pair, called an exciton, is still bound together through an attractive electrostatic Coulombic force. Once this attractive force is overcome, the

exciton dissociates, and the electron spatially separates from its respective hole by moving into a lower energy unfilled orbital in the neighboring transport material (B). Electron and hole separation typically occurs due to the inclusion of an electric field across the light absorbing material;<sup>5</sup> Since electrons and hole are charged particles, the electric field accelerates the electrons and holes to their respective drains. In the absence of an electric field, charge carriers move randomly throughout the lattice, until they eventually recombine before useful work can be done. In silicon based cells, non-native dopants, such as B or P,<sup>5</sup> are included to create an uneven potential barrier that generates the electric field, whereas in thin film devices the transport layers can form the electric field when the light absorbing material exhibits a strong dielectric potential. In silicon devices, the doped regions can be considered as the transport materials depicted in Figure 1.1.1, where in thin films materials such as TiO<sub>2</sub> make up the transport layers. From here, the electron moves into an unoccupied orbital of even lower energy in the drain where it is transported off to do work across a load (C), such as a light bulb, battery, computer, etc. The electron returns to the cell (D), where it recombines with a hole, and the process can start again.

Figure 1.1.1 can easily be extended to be representative of a solar farm connected to a city electrical grid if instead a) was not just a single cell, but rather an array of solar cells, and if in b) an electrical distribution center and grid were placed between between (B) and (D), while (C) was connected solely to the distribution center. It is also important to note that the amount of electricity that can be generated from the photovoltaic process is determined by the difference in potential of the two drains, and not by the difference in energy between the highest filled orbital (frontier valence orbital) and lowest unfilled orbital (frontier conduction orbital) of the light absorbing material, called the band gap ( $E_g$ ). This is where the significance of solar cell device design becomes apparent; It is important that not only does current flow in one direction, controlled by the relative heights of the frontier orbitals,<sup>†</sup> but also that sufficient energy is retained when moving charge carriers<sup>‡</sup> to their respective drain. If the potential difference between the drains is small, very little electrical power will be generated, regardless of the size of the band gap. It is therefore ideal, to have a drain be very close in energy to its respective frontier orbital in the light absorbing material as to minimize energy loss, *i.e.* ideally the difference in drain potentials is equal to the

---

<sup>†</sup>electrons will always try to move down in energy and holes will always try to move up in energy

<sup>‡</sup>Charge carriers refers to a particle carrying a charge and is often used to describe both electrons and holes.

band gap of the light absorbing material. Thus, the band gap, an intrinsic electrical property of a material, determines how much electrical power that device can generate; This is one of the origins of efficiency limitations in solar devices, called the Shockley-Queisser (SQ) limit.<sup>6</sup>

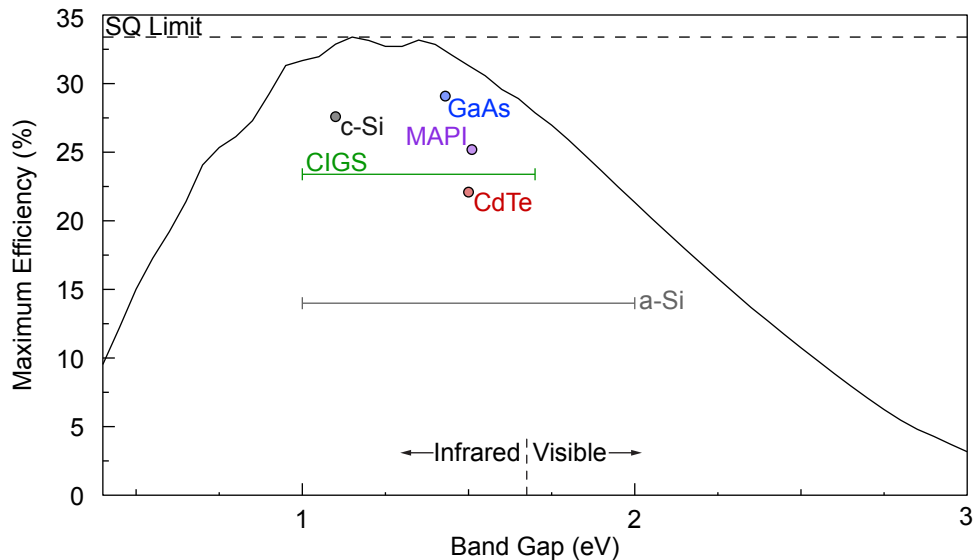


**Figure 1.1.2** The maximum achievable efficiency for a single junction solar cell as determined by the Shockley-Queisser limit (dashed line). Notable achievements in solar materials development are shown. The range of band gaps is given for materials with a variable band gap.

The SQ limit, plotted in Figure 1.1.2, is the maximum efficiency a photovoltaic material can obtain depending on its band gap. For a single material solar device, a maximum photon-to-electricity conversion efficiency of 33.7 % can be obtained when the material's band gap is 1.34 eV (the second highest efficiency being 30 % obtained with a band gap 1.1 eV). Therefore, to maximize the amount of electricity produced in a solar cell, the band gap (and thus the difference in drain potentials) should be 1.34 eV. The fundamental underpinning of the SQ limit is the trade off between the number of photons absorbed, their energy, and the number of radiative recombination events as a fraction of all recombination events.

It can readily be seen from Figure 1.0.2 that the number of photons available at any given wavelength is limited. As only photons with energy equal to or higher than the energy of the band gap can be absorbed, the band gap of a material automatically determines how much of the solar spectrum can be utilized. It is important to note that energy above the band gap is often lost to nonradiative processes such as heat generation. Generated charge carriers, therefore, typically have energy equal to the band gap. Efficiency is dependent upon both how many photons are being absorbed as

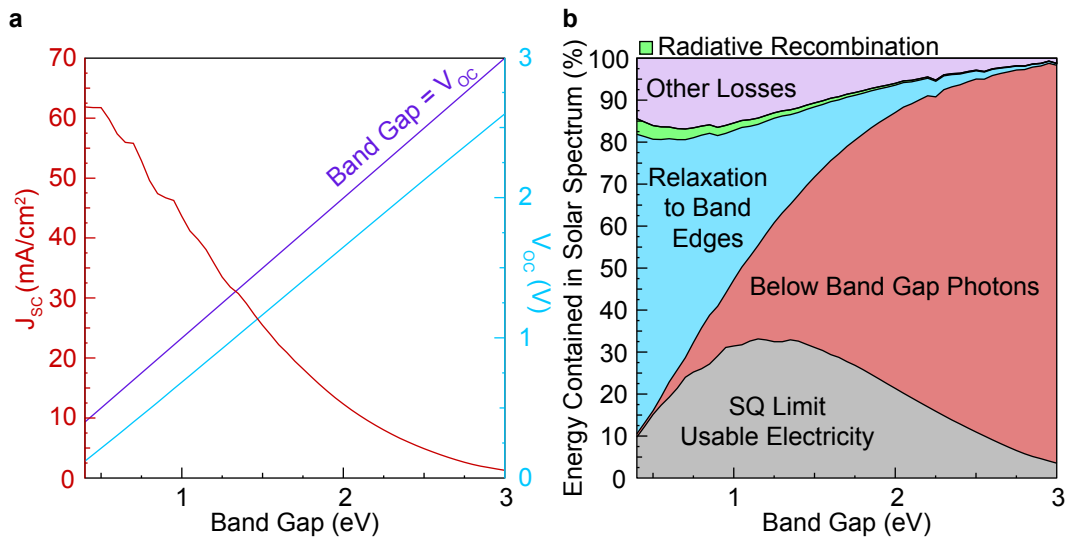


**Figure 1.1.3** a) Simulated short circuit current density ( $J_{sc}$ , red) and open circuit voltage ( $V_{oc}$ , blue) obtainable as dependent upon a materials band gap. Both a larger  $J_{sc}$  and  $V_{oc}$  lead to higher maximum efficiency. b) Various losses of the energy contained in the solar spectrum depending on the band gap of the absorbing material.

well as their energy. When the band gap is lowered, a larger portion of the solar spectrum can be utilized, and thus more photons can be absorbed, but they contain less energy. When the band gap is raised, a smaller portion of the solar spectrum has sufficient energy to traverse the band gap, and thus the number of photons absorbed is reduced, but each excited electron contains more energy. This interdependence is made readily apparent through the inverse relationship of the current density (number of photons absorbed) and the voltage (the working energy of the photon), presented in Figure 1.1.3a; It can therefore be regarded as a quantity (number of excited electrons) versus quality (energy of the excited electron) problem with the SQ limit giving the maximum obtainable efficiency. The argument so far, however, relies on the principle of detailed balance, which states that at equilibrium, all elementary processes are in equilibrium with their reverse processes. For solar devices, the generation of an excitation in the light absorbing material is in equilibrium with radiative recombination processes. As such, Shockley and Queisser optimistically assumed the only recombination events in solar devices (for the purpose of maintaining detailed balance) are radiative in nature. In this regard, as the ratio between radiative recombination events and all recombination events decreases (fewer radiative recombination events), the maximum efficiency achievable through the SQ limit simultaneously decreases. It is therefore heavily implied in the SQ limit that radiative recombination describes a majority of recombination in efficient solar devices.

The maximum obtainable efficiency is limited to  $\sim 33\%$  (instead of  $100\%$ ) due to the various energetic losses presented in Figure 1.1.3b. These processes include heat generation, exciton recombination, photons passing through the cell, and other recombinatorial losses. For materials with large band gaps, photons of energy below the band gap cannot be absorbed by the light absorbing material, and simply pass through the cell. Tandem solar cells, solar cells made with two or more light absorbing materials with differing band gaps, offer a simple way to address the large loss of efficiency. The idea is that one light absorbing material has a larger band gap to harness the large potential of high energy photons while a smaller band gap material absorbs the light of lesser energy that would normally pass right through the cell. Such devices need very careful alignment of their respective electrodes to ensure the large potential of high energy photons is maintained, and as such, single absorbing material devices are much easier to design. Relaxation to band edges, the highest energy loss for small band gap materials, is also addressed in tandem cells by the larger band gap material. In a single material solar cell of smaller band gap, much of the potential contained in high energy photons is lost in process such as heat generation as the high energy electron relaxes to the lower energy unoccupied orbital. Adding a larger band gap material in tandem reduces the energy loss of high energy photons. While tandem cells offer a way to surpass the SQ limit, it is important to maximize the efficiency of individual component so as to maximize the overall efficiency of all manufactured devices, tandem or single. A significant amount of work has been expended towards the goal of reaching the SQ limit for a single junction device. To date we have yet to reach the SQ limit, but an up-and-coming material (Perovskites), the focus of this thesis, has seen rapid growth in its conversion efficiency ( $> 20\%$ ) within the last decade.

## **I.2 Solar Devices**

The photovoltaic effect was first discovered by French physicist Edmon Becquerel in 1839.<sup>§</sup> Becquerel placed silver chloride into an acidic solution, and when it was illuminated, a voltage was recorded across two platinum electrodes.<sup>9</sup> Approximately 50 years later (1883) Charles Fritts constructed the first solid state solar device by coating a plate of copper with selenium, topping it with a thin semi-transparent layer

---

<sup>§</sup>Interestingly, Becquerel's discovery of the photovoltaic effect had an indirect hand in the formation of Quantum Mechanics. Becquerel's discovery was deemed instrumental to the discovery of the photoelectric effect,<sup>7,8</sup> which challenged the commonly accepted universality of the laws provided by Newton's Classical Mechanics, and later, in the hands of Einstein, provided some of the foundations of Quantum Mechanics.

of gold. While Fritts' device had an efficiency of only 1%, it was the first solar device ever installed on a New York rooftop in 1884.<sup>10</sup> Even though the efficiency of Fritts' device was low, it provided a starting point for solar cell research and showed that such devices could readily be implemented among modern cityscapes and consumer households. The creation and improvement of solar devices that exhibit the photovoltaic effect remains an active area of research to this day.

### **I.2.1 First Generation Solar Cells**

First generation solar cells, also named wafer-based solar cells, are comprised primarily of crystalline silicon. These crystalline devices are either monocrystalline (a single large crystal) or polycrystalline (many small crystals). Historically, consumers are generally more familiar with crystalline silicon wafer-based devices compared to newer generation solar devices. While other solar materials continue to emerge and develop, to date, first generation silicon solar cells remain dominant in the solar cell consumer market.

#### **Monocrystalline Silicon Solar Cells**

In 1954, over a century after Edmon Becquerel's discovery of the photovoltaic effect, Daryl Chapin, Calvin Fuller, and Gerald Pearson invented the first silicon based solar cell at Bell Laboratories,<sup>11</sup> marking the creation of the first modern solar device. This solar cell was made primarily of crystalline silicon wafers which defined first generation solar cells as wafer-based photovoltaics. Early first generation devices were made from cuts of large single crystal silicon, which later gave rise to the high efficiencies seen today (> 25%).<sup>12-16</sup> These devices, by definition, are synthetically difficult to obtain and thus expensive to manufacture as large single crystals do not naturally occur. These single crystals require an exceedingly pure form of silicon (99.9999% purity for solar applications) and thus the single crystal makes up the bulk of the solar cell cost.<sup>17</sup>

#### **Polycrystalline Silicon Solar Cells**

Another wafer-based photovoltaic material, polycrystalline silicon, is synthetically simpler to obtain than their monocrystalline predecessors as it is comprised of numerous small crystals, instead of one large continuous crystal. One result of the simpler synthetic conditions is that polycrystalline silicon devices are often cheaper than monocrystalline devices. Polycrystalline devices, however, are typically less efficient than their monocrystalline alternatives (23.3 %) <sup>12</sup> as they contain numerous grain boundaries which can interrupt charge carrier transport.

## **I.2.2 Second Generation Solar Cells**

Second generation solar cells, also referred to as thin-film solar cells, stretch beyond the crystalline silicon of wafer-based devices and include GaAs, CdTe, amorphous silicon, and  $\text{CuIn}_x\text{Ga}_{(1-x)}\text{Se}_2$  (CIGS). In thin-film devices the light absorbing material is thinner than its wafer-based predecessors, usually 1 - 10  $\mu\text{m}$  versus 100 - 350  $\mu\text{m}$  for first generation silicon based cells; In some cases this can permit thin-film devices to be flexible, creating roll-up solar panels useful for on-the-go electricity generation at remote locations. The thinness of the light absorbing material is accredited to their large absorption coefficients, enabling a thinner region of thin-film light absorbers to absorb an equivalent amount of light as thicker wafer-based silicon devices.

Regardless, first generation wafer-based silicon devices still dominate the current consumer market, and will likely continue to dominate in the near future as the architecture for manufacturing silicon devices as well as the consumer market for such silicon based devices is well established.

### **Amorphous Silicon Solar Cells**

Thin-film solar devices began appearing in the consumer market in the late 1970s as small amorphous silicon solar cells were being incorporated into pocket calculators. Due to the thinner size and amorphous nature, amorphous silicon solar devices are cheaper than their crystalline silicon counterparts. Amorphous silicon cells, however, are less efficient than their mono- and polycrystalline ancestors, with a highest NREL verified efficiency of only 14 % in 2016,<sup>12,18</sup> likely due to the random nature of amorphous solids inhibiting long-range charge transport. As such, the likelihood of large scale amorphous silicon solar devices being utilized for major power generation instead of in small hand held solar powered devices (calculators, watches, phones, etc.) is not promising.<sup>19</sup>

### **GaAs Solar Cells**

While amorphous silicon may have poor efficiency, other second generation solar devices show exceptional efficiency. GaAs in 2019 achieved a record efficiency of 29.1% and to date is the highest efficiency single junction solar cell.<sup>12,20</sup> GaAs, however, is costly, greatly limiting its commercial affordability by the average consumer household and as a result has primarily been used for power generation in satellites and other space faring crafts.<sup>21</sup> Thus, the consumer market for household application of GaAs solar cells is very limited.

## **CdTe Solar Cells**

On earth, CdTe remains a major competitor of silicon based photovoltaic devices in solar farms.<sup>22,23</sup> Currently, CdTe has a certified maximum efficiency of 22.1 %, <sup>12</sup> but proper disposal of CdTe remains a health concern as the extraordinary toxicity of Cd is problematic.<sup>24</sup> Additionally, the scarcity of Te presents a major problem to large scale incorporation of CdTe devices. It has been projected that at 2017 rates, it would take 1500 years to produce enough Te to meet world energy demands of 2050 using CdTe alone.<sup>19</sup> The real benefit of CdTe solar cells is their cost efficiency. CdTe devices have been able to match the efficiency of common silicon based cells, all while being more cost effective, partially due to its low cost manufacturing enabled by benign synthetic conditions.<sup>19,25</sup>

## **CuIn<sub>x</sub>Ga<sub>(1-x)</sub>Se<sub>2</sub> (CIGS) Solar Cells**

The other major competitor of modern silicon wafer-based solar devices is CIGS, with a highest verified efficiency of 23.4 % (2019).<sup>12,26</sup> Unlike CdTe, and GaAs, the band gap of CIGS solar materials is readily tunable by changing the ratio of In to Ga, ranging from 1.0 eV for CuInSe<sub>2</sub> (x = 1) to 1.7 eV for CuGaSe<sub>2</sub> (x = 0). This gives CIGS based devices versatility when it comes to manufacturing, allowing them to be incorporated in a wider array of devices to meet individual consumer needs.

### **1.2.3 Third Generation Solar Cells**

The latest generation of solar materials, third generation solar cells or emerging photovoltaic cells, are materials that are currently being rigorously researched and have yet to make it to consumer markets. It is hoped that third generation solar cells will be able to cheaply meet the inherent limit in efficiency for single junction devices as described by the SQ limit, Figure 1.1.2, as well as be able to cheaply surpass the SQ limit in tandem cells. While promising progress has been made, third generation solar materials have yet to meet the SQ limit. Third generation solar cells can be classified as any material being researched for its photovoltaic properties that is not already a first or second generational solar material. As such, the definition of third generation solar materials is wide and many materials can readily fit the description, but notable emerging photovoltaic materials include dye-sensitized solar cells (DSSC), organic based solar cells, quantum dots (QD), Cu<sub>2</sub>ZnSn(S/Se)<sub>4</sub> (CZTSSe), and perovskites.

#### **Dye-Sensitized Solar Cell (DSSC)**

The first third generation solar cell was a DSSC created in 1991.<sup>12,27</sup> Currently, these

cells have obtained a maximum efficiency of 12.3 %<sup>12</sup> and have several benefits associated with them: low manufacturing cost, flexibility, tunable transparency and color, and roll-to-roll printing capability.<sup>28</sup> DSSC are unique in their structure as the light absorbing material (the dye) is anchored on mesoporous TiO<sub>2</sub> bordered by an electrolyte. The dye undergoes a redox reaction with the electrolyte to pass photon generated charge carriers to the other side of the device, a process described as being similar to photosynthesis.<sup>29</sup> DSSC forgo the use of the prototypical internal electric field used to separate charge carriers, making their design very unique compared to first and second generation solar cells. The key to tuning the electrical properties of DSSC lies in the organic dye, the identity of which controls the band gap and electrical transport properties. DSSC have yet to meet their goal of 15 % efficiency, and are limited by recombination losses between TiO<sub>2</sub> and the electrolyte.<sup>28</sup>

### **Organic Molecular Solar Cells**

Organic based solar cells utilize photoactive polymers or large organic molecules as the light absorbing material, obtaining a maximum verified efficiency of 17.4 % in 2019.<sup>12</sup> Historically, organic solar cells had poor efficiency (< 1 %), due to the extreme localization of charge carriers due to their organic nature, in stark contrast to inorganic scaffolds which boast strong delocalization. Organic based solar materials are well suited for small portable devices (similar to amorphous silicon) due to their exceptionally cheap manufacturing and extraordinary flexibility. Their efficiency, however, is limited by their morphology.<sup>29</sup> Current challenges to the increased efficiency of organic based devices include addressing the misalignment of polymers/large organic molecules within the light absorbing region on a microscopic scale. Misalignment creates areas of localization which boost recombination, thus lowering the conversion efficiency.

### **Quantum Dot (QD) Solar Cells**

The architecture of QD based solar cells is directly derived from DSSC,<sup>30</sup> where the organic dye of the DSSC is replaced with a QD. Here, the QD acts as the light absorbing material (in lieu of the organic dye) achieving a maximum verified efficiency of 16.6 % in 2019.<sup>12,31</sup> QD based solar devices are versatile as they can readily absorb across the entire visible spectrum by varying their band gap using quantum confinement effects. As such, these materials excel in multijunction devices, enabled by their tunable electric properties. The development of QD solar devices, however, has lagged behind

other devices; There is still a need to improve QD loading onto  $\text{TiO}_2$  surfaces, suppress charge recombination, improve long term stability, and explore additional electrolyte materials.<sup>30</sup>

### **$\text{Cu}_2\text{ZnSn(S/Se)}_4$ (CZTSSe) Solar Cells**

The structures of  $\text{Cu}_2\text{ZnSnS}_4$  (CZTS),  $\text{Cu}_2\text{ZnSnSe}_4$  (CZTSe), and their alloy,  $\text{Cu}_2\text{ZnSn(S/Se)}_4$  (CZTSSe), are based upon chemical substitutions to their parent material,  $\text{CuIn}_x\text{Ga}_{(x-1)}\text{Se}_2$  (CIGS). From the CIGS structure, a second Cu is added, the trivalent In and Ga are substituted with divalent Zn and Sn. Se is either fully, partially, or not substituted with S to form CZTS, CZTSSe, and CZTSe, respectively. CZTSSe has achieved a verified maximum efficiency of 12.6 %, however, NREL has yet to verify a higher efficiency for CZTSSe since 2013.<sup>12,32</sup> The stumbling block in progress towards a better performing CZTSSe solar cell is likely caused by problematic conditions in the material, specifically defect regions and charge carrier recombination at interfaces.<sup>33</sup>

### **Perovskite Solar Cells**

Perovskites, the main focus of this thesis, have seen phenomenal growth in conversion efficiency in the past decade, starting at just 3.8 % in 2009<sup>34</sup> to a verified 25.2 % in 2019.<sup>12</sup> This ~ 20% increase in efficiency occurred within a decade of perovskites first being presented as a photovoltaic material, and their light-to-electricity efficiency growth rate is faster than any other solar material in history.

### **1.3 Perovskites**

The perovskite mineral,  $\text{CaTiO}_3$ , was originally discovered in the Ural mountains of Russia in 1839 by the German mineralogist Gustavus Rose.<sup>35</sup> He decided to name the mineral after Russian mineralogist Lev Perovski. While originally, the term perovskite was used as a name for the perovskite  $\text{CaTiO}_3$  mineral, it has been applied as a general term for minerals and compounds of similar structure.  $\text{CaTiO}_3$  is readily described by an  $\text{ABO}_3$  structure, where A is a dicationic metal ( $\text{A}^{2+}$ ), B is a tetracationic metal ( $\text{B}^{4+}$ ), and O is oxygen ( $\text{O}^{2-}$ ), see Figure 1.3.1; Specifically, B is encased in an octahedron made by O. These octahedra are connected through their corners (corner-sharing octahedra), creating a cage between eight separate octahedra, inhabited by A. In general, as long as B can form corner-sharing octahedra with O, and an A cation of appropriate charge can fit within the cage, then the perovskite structure can be obtained. While  $\text{CaTiO}_3$  was originally orthorhombic in structure, the general perovskite structure can also occur in the cubic and tetragonal phase, depicted in

Figure 1.3.1. In general, the phase of the perovskite material is controlled by its temperature. While the transition temperatures will vary based upon chemical composition, perovskites typically transition from orthorhombic to tetragonal and finally to cubic with increasing temperature. Which phase is the most stable at room temperature, however, is determined by the delicate balance of the size of the octahedron in relation to the A-site cation. In this regard, when components are chosen carefully, any phase can be obtained for a room temperature structure.

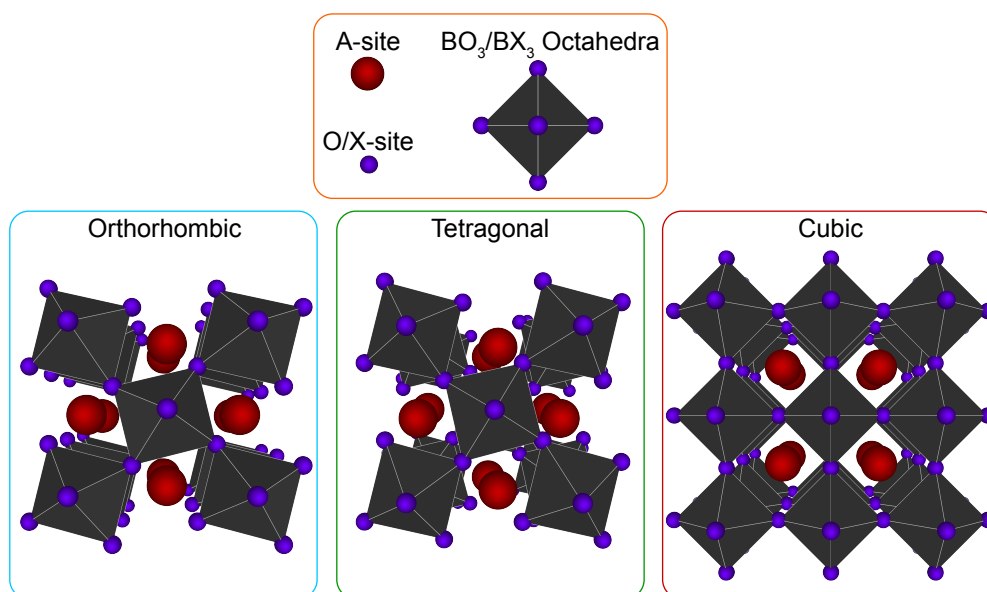


**Figure 1.3.1** Various phases of  $ABO_3$  and  $ABX_3$  perovskites. In general, as temperature increases most perovskite lattices transition from orthorhombic to tetragonal and finally to cubic.

### 1.3.1 Beyond the Oxide: the Halide analog

It wasn't long after the discovery of the perovskite mineral  $CaTiO_3$  that the first halide based perovskites analog was uncovered,  $APbX_3$  ( $A = K^+$ ,  $Cs^+$  and  $X = Cl^-$ ,  $Br^-$ ,  $I^-$ ).<sup>36</sup> The halide alternative takes the form  $ABX_3$ , where A is a singly charged cation, B is a divalent metal, and X is a halide. It is readily seen through charge comparison that the halide based structure ( $A^+B^{2+}X_3^-$ ) is the same as the oxide based mineral ( $A^{2+}B^{4+}O_3^{2-}$ ) with reduced charges. The halide alternatives exhibit the same structures depicted in Figure 1.3.1, as well as the same dependence on temperature and cation/octahedron size ratio.

In 2009, Kojima, Teshima, Shirai, and Miyasaka attempted to boost the efficiency of DSSC by utilizing a perovskite as the light sensitizer.<sup>34</sup> The solar cell only had an efficiency of 3.8 %, but it generated great interest in halide perovskite photovoltaics. Up to that point, oxide perovskites photovoltaics generated little interest, as metal

oxide perovskites had unfavorable semiconducting properties for photovoltaic applications.<sup>37</sup> Kojima and colleagues had no idea that they were about to create a new field in photovoltaics, as they had set out to improve the efficiency of DSSC which at the time had yet to reach 10 % efficiency. In the following year, the excellent electronic properties of halide based perovskites came to light,<sup>38-40</sup> and interest continued to grow as unstudied variations in perovskites structures and compositions were investigated for interesting new and improved photovoltaic properties.

Halide perovskites come in two general flavors. On one side are all-inorganic perovskites such as  $\text{CsPbX}_3$ ,<sup>41-43</sup> while on the other are the hybrid organic-inorganic perovskites, such as  $(\text{CH}_3\text{NH}_3)\text{PbX}_3$ .<sup>44</sup> Unlike their oxide predecessors, halide perovskites utilized small positively charged organic molecules as alternative A-site cations, increasing the diversity of plausible halide perovskite structures. A range of A-site cations have been tried, including ammonium,<sup>45</sup> acetamidinium,<sup>46</sup> guanidinium,<sup>47</sup> and various mixes of A-site cations.<sup>48-52</sup> However, cesium, formamidinium,<sup>53</sup> and methylammonium remain at the forefront of perovskite photovoltaic efficiency and research.

The diversity of the B-site divalent metal has been relatively limited compared to the diversity of the A-site, as the electronic properties of perovskites are primarily determined by the  $\text{BX}_3$  lattice.<sup>54-56</sup> As such, it is difficult to find a diverse array of feasible B-site metals that keep the important photovoltaic properties of the commonly researched perovskite lattices, primarily  $\text{Pb}$ <sup>34,41,44,53,57,58</sup> and  $\text{Sn}$ .<sup>59-61</sup> Fortunately, when it comes to the electrical properties of a given perovskite material, the role the halide plays has been determined to be straightforward, as its primary role is to tune the band gap.<sup>62</sup> Generally, the band gap decreases (red shift) as the radius of the halide increases. The A-site cation, however, does have some influence on the perovskite electrical properties. As previously stated, the ratio of sizes between the  $\text{BX}_3$  octahedron and the A-site cation determines the low temperature phase of the perovskite; the electrical properties of perovskite materials are indirectly influenced by the identity of the A-site cation, as they effect the tilting and orientation (and therefore B-X orbital overlap and thus bonding) of the  $\text{BX}_3$  lattice.<sup>63</sup> Therefore, if one wishes to fine tune the electrical properties of a perovskite, one should start with a perovskite with electrical properties similar to the desired outcome and make adjustments to the identity of the X-site halide and the size of the A-site cation through replacement or mixing. In practice, however, this is exceptionally difficult as not all combinations lead

to a perovskite (let alone in the desired phase), and currently there is no rational guideline when it comes to tuning electrical properties with regards to the B-site cation.

Even in the absence of detailed guidelines when changing the identity of the A-site and B-site cations to rationally augment electrical properties of the host, the favorable electronic properties of champion perovskite devices for photovoltaic applications persists. Tireless research in the field of perovskites photovoltaics, spurred by the interest generated from Kojima and coworkers 2009 work, has lead to a staggering increase in efficiency over the past decade. Hopefully the impressive progress made over the last decade will continue to generate more interest in the young field of perovskite photovoltaics, and if efficiency of perovskite photovoltaic devices continue to increase at current rates, the SQ limit will likely be reached prior to 2030. The importance that perovskite photovoltaics hold in the near future cannot be overstated.

### **I.3.2 Perovskites in Photovoltaics: Promising Properties**

Perovskites are host to several properties, electrical and physical, that make their application prospects in future photovoltaic devices promising. Perovskites exhibit, among other electrical properties, strong photon absorption in the visible spectrum, excellent charge carrier transport properties, as well as an unparalleled resistance to detrimental defects. These factors are responsible for the superior photovoltaic performance demonstrated by perovskite devices. Additionally, perovskites are capable of being cheaply and efficiently mass produced through roll-to-roll processing techniques. Overall, these factors support perovskites as a promising alternative in the future to silicon based devices.

#### **Absorption Properties**

One of the most important functional properties of a solar material is its ability to effectively transform photons into electricity. As previously mentioned, the maximum achievable efficiency for a material is determined by the SQ limit. Assuming a perfect interface with transport materials and a lack of inhibiting defect and recombination events, maximum efficiency is achieved when a balance is struck between the number of photons being absorbed and their energy. For a photon to be absorbed, it must have sufficient energy to overcome the band gap. As the portion of the solar spectrum with photons of sufficient energy to be absorbed is a constant for a given band gap, the only way to increase efficiency in a material with a perfect interface and devoid of defects and parasitic recombination is to increase the number of photons being absorbed. In

real materials, the likelihood of a photon of sufficient energy being absorbed is determined by its absorption coefficient and the directness of its band gap. The absorption coefficient is a general measure of how likely a photon of a given wavelength will be absorbed by a material, or rather, how far a photon of a given wavelength must penetrate into a material before it is absorbed. The higher the absorption coefficient for a wavelength, the more likely a photon of that wavelength will be absorbed as it penetrates the material, and thus, the penetration depth before absorption is smaller. As such, materials with large absorption coefficients in the visible spectrum appear darker in color as they get thicker as fewer visible photons escape the material without being absorbed. As the absorption coefficient increases, a thinner region is required to absorb incoming light. The absorption coefficient of GaAs is  $\sim 10^4 \text{ cm}^{-1}$  in the visible spectrum, whereas for crystalline silicon it is  $\sim 10^3 \text{ cm}^{-1}$ , which is one reason why thin-film materials such as GaAs incorporate light absorbing regions much thinner than their silicon counter parts; Similar to their thin-film predecessors, perovskites boast high absorption coefficients in the visible region,  $\sim 10^5 \text{ cm}^{-1}$  for the prototypical perovskite  $(\text{CH}_3\text{NH}_3)\text{PbI}_3$ .<sup>64,65</sup>

The second factor that determines how likely a photon of a given wavelength is to be absorbed is the directness of the band gap. Having an indirect band gap directly detracts from the absorption coefficients of photon wavelengths lower than the lowest direct band gap. An indirect band gap occurs when the highest energy occupied orbital and the lowest energy unoccupied orbital occur at different points in momentum space. Simply put, in order for a photon to be absorbed across an indirect band gap, a change in momentum within the crystal lattice (the absorption or emission of a phonon) must also simultaneously occur, as required by the law of conservation of momentum. This means two simultaneous events must occur (the absorption of a photon and the absorption or emission of a phonon), which is less likely than a single event, hence materials with indirect band gaps exhibit smaller absorption coefficients in energy regions equal to the width of the indirect gap. For example, crystalline silicon's smallest band gap ( $\sim 1.1 \text{ eV}$ ) is indirect while its smallest direct band gap is much larger ( $\sim 3 \text{ eV}$ ). This is why crystalline silicon has a lower absorption coefficient in the visible region than other solar devices and why the absorption coefficient of crystalline silicon spikes around 400 nm, or  $\sim 3.1 \text{ eV}$ .<sup>64</sup> Perovskites, on the other hand typically have direct band gaps, hence they exhibit larger absorption coefficients across all energies greater than the band gap. Thus, due to their larger absorption coefficients

and the direct nature of their band gaps, perovskites often exhibit excellent absorption properties pertinent to photovoltaic applications.

It is important to note that the absorption properties mentioned thus far often have a direct impact on the consumer cost of photovoltaic devices. As mentioned single crystalline silicon solar devices typically need thicker absorption regions compared to their thin film competitors as they have low absorption coefficients in the visible region. It's not hard to rationalize why this increase in required thickness increases the cost of single crystal silicon based devices, as single crystals are costly to grow. In this regard, a consumer may find it advantageous to compare the price per watt of a device rather than pure efficiency. The price per watt of solar devices inherently includes descriptors that relate efficiency to the cost of material production. For a consumer, the ideal value of \$ / Watt is as low as possible as it indicates that a device is either more efficient, cheaper, or both. Lawrence Berkeley National Laboratory reported that in 2018 the American national average installation price of solar devices for residential consumers was \$ 3.7 / Watt.<sup>66</sup> As such, a price per Watt lower than 3.7 (assuming identical device longevity and no additional hidden costs) suggests a better deal for the consumer. The end goal of solar device development, therefore, is to provide the lowest price per Watt while maximizing device longevity and minimizing device size.

### **Transport Properties**

Perovskite solar devices have demonstrated the presence of several key electrical transport properties of merit essential for high light-to-electricity conversion efficiency. It is the general consensus of the research community that these key properties inherent in perovskites play a decisive role in their superior photovoltaic performance. For example,  $(\text{CH}_3\text{NH}_3)\text{PbI}_3$  has exhibited small charge carrier effective masses,  $m_e^* = 0.23 m_0$  and  $m_h^* = 0.29 m_0$ , which are comparable to silicon ( $m_e^* = 0.19 m_0$  and  $m_h^* = 0.16 m_0$ ).<sup>67</sup> Small effective masses ( $< 1 m_0$ ) facilitate efficient transport of charge carrier towards their respective drains, increasing conversion efficiency compared to heavy effective masses ( $> 1 m_0$ ). Before free charge carriers can be transported towards their respective drains to do useful work, they must first be separated in the generated exciton. When an exciton is formed from the absorption of light, there is a remaining energy penalty that must be paid in-order to overcome the attractive Coulombic force keeping the charges in the exciton bound together. This energy is called the exciton binding energy. The larger the exciton binding energy, the more energy must be paid to separate charge carriers. As such, small exciton binding energies are desirable for

photovoltaic applications as charge carriers are then trivial to dissociate. Perovskites exhibit just that, small exciton binding energy, predicted to be likely as small as 5 - 15 meV for  $(\text{CH}_3\text{NH}_3)\text{PbI}_3$ .<sup>68</sup> This is much lower than thermal energy contributions at room temperature ( $\sim 26$  meV), suggesting that the exciton binding energy for  $(\text{CH}_3\text{NH}_3)\text{PbI}_3$  can easily be overcome from ambient energy in the surrounding environment alone, and little to no excess energy is required. Such a case supports excellent light-to-electricity conversion efficiency, and is likely one of the leading factors in the superior photovoltaic performance demonstrated by perovskites.

Once the exciton binding energy has been overcome, and charge carriers are separated, they must then move towards their respective drains to be collected for useful work. It is important that free charge carriers make it to their drain prior to recombination with their counterpart carrier. The average distance a charge carrier can travel before recombining with a charge carrier of opposite charge is known as the charge carrier diffusion length. Larger charge carrier diffusion lengths implies that a charge carrier can make it farther from their point of generation before recombining, and is typically thought to enhance the efficiency of solar devices. The diffusion length of a charge carrier is directly related to the charge carrier lifetime. The farther away a mobile charge carrier can make it from its point of generation, the longer it must last. Charge carrier lifetime, however, is not necessarily indicative of large charge carrier diffusion lengths, as charge carriers can get trapped in defect trap states and persist for a long time before recombining without moving any further away from their point of generation. However, in perovskites, this is not a common occurrence (see next section), and charge carrier lifetimes and diffusion lengths remain long despite the presence of defects.<sup>38,39,69</sup> Research has predicted diffusion lengths of  $> 175 \mu\text{m}$  in 3 mm thick perovskite single crystals.<sup>40</sup> While the diffusion lengths shown by Dong *et al.* are smaller than the thickness of their crystal, perovskite crystals in solar devices can be sub  $\mu\text{m}$ ,<sup>70,71</sup> suggesting that predicted diffusion lengths are more than sufficient to carry charge carriers across the entire length of the perovskite absorber towards their respective drains.

Heavy metals based perovskites (typically Pb) often exhibit the Rashba splitting effect, which is responsible for turning direct band gap semiconductors into indirect ones. In the Rashba splitting effect, strong spin-orbit coupling (prevalent in heavy metals such as Pb) combines with asymmetry present in a crystal lattice to remove degeneracy of degenerate orbital configurations. This effectively splits two overlapping

bands in the band structure by altering their moment component by:  $\pm|\Delta\text{RashbaSplitting}|$ . Such effects are readily seen in  $(\text{CH}_3\text{NH}_3)\text{PbI}_3$ , where the Rashba splitting causes the lowest unoccupied orbital to split across its high symmetry momentum point. The result is that the highest occupied orbital and the lowest unoccupied orbital no longer occur at the same point in momentum space. As such, the Rashba splitting results in an indirect band gap for  $(\text{CH}_3\text{NH}_3)\text{PbI}_3$ . While there is agreement that Rashba splitting is exhibited in Pb based perovskites, there is disagreement as to the extent of its effects. Some argue that the extent of Rashba splitting is large, resulting in long charge carrier lifetimes similar to the indirect band gap semiconductor Si which give rise to superior photovoltaic performance.<sup>72,73</sup> Others argue that the extent of splitting is small or negligible and the innate exceptional electronic properties of Pb based perovskites such as small charge carrier effective masses are to blame for superior photovoltaic performance.<sup>74</sup> Either way, Pb based perovskites continue to display superior photovoltaic properties.

## Defects

The presence of defects in a semiconductor often determines its function and usefulness. The most relevant example is the silicon solar cell. Without dopants present in some portion of the device, silicon solar cells do not actually generate large quantities of electrical power.<sup>5</sup> When implemented correctly, defects can improve photovoltaic performance, however, when implemented incorrectly they can also have counterproductive effects. The formation of counterproductive defects, such as defects that lie deep in the band gap, is by definition, unfavorable for photovoltaic applications. For example, deep defects often act as recombination centers for charge carriers prior to reaching the transport material, and thus charge carriers recombine before useful work can be performed. Thankfully, perovskites have shown exceptional resistance to the formation of deep defects.<sup>75</sup> Investigation of defects in perovskites finds that intrinsic defects readily form (Pb vacancies and MA interstitials), but are often shallow or contained within the band edge.<sup>76</sup> The absence of deep level defects suggests that charge carrier diffusion lengths and lifetimes will be relatively uninhibited by the presence of these shallow defects. In fact, it has been suggested the surface defects can possibly improve charge carrier transport across grain boundaries, improving photovoltaic properties.<sup>77</sup> Such defects can be readily implemented through controlling the ratio of  $\text{PbI}_2$  to  $(\text{CH}_3\text{NH}_3)\text{I}$  precursors.<sup>78</sup> Interestingly, this process can result in either n- or p-type perovskites using only intrinsic defects. As a result,

synthetically obtaining n- or p-type doped perovskites should be simple as additional synthetic constraints or conditions to incorporate nonnative dopants is unnecessary.

### **Roll-To-Roll Processing**

Perhaps one of the most promising aspects of perovskite photovoltaics is their ability to be manufactured using roll-to-roll processing. In roll-to-roll processing, a spool of plastic provides a flow of clean flexible plastic to a machine that deposits a solution containing perovskite directly onto the plastic.<sup>79</sup> The perovskite containing flexible plastic then moves through a heating element to remove solvent and promote perovskite crystal growth. The perovskite containing flexible plastic is finally spun onto a second spool as the final product, where it can then be cut into sheets of any desired shape or size to be incorporated into a solar device. This process can be viewed in a fashion similar to the mass printing of newspaper depicted in movies and television shows. While there are many techniques and nuisances to preparation of the perovskite solution, they generally involve mixing of precursors, such as  $(\text{CH}_3\text{NH}_3)\text{I}$  and  $\text{PbI}_2$ , into a solvent in the presence of heat.<sup>80,81</sup> When it comes to roll-to-roll processing methods, there are two ways to impart the perovskite solution onto the moving flexible plastic: slot-die coating and blade coating. In slot-die coating the perovskite solution is printed onto the plastic as an ink in a fashion similar to modern household printers. In blade coating, a blob of perovskite solution on the plastic is moved towards a tilted blade, which flattens out the solution as the plastic moves past the blade. The blade coating method is similar to a knife spreading butter on a piece of toast, however, the bread and butter move towards the knife while the knife remains stationary. Regardless of coating methods, a direct route to roll-to-roll processing of perovskite solar cells allows for cheap and efficient mass production (a tremendous benefit for any consumer product) of perovskite based devices. Such processes should aid in reaching a minimum in price per Watt, providing the cheapest and most efficient devices for the consumer.

#### **I.3.3 Factors Limiting Commercialization: Lead**

It's easy to rationalize the presence of lead being a barrier to commercialization as one can readily imagine the negative connotation and opinion a consumer would have towards a product whose primary component contains lead. However, some have suggested that simply containing lead should not be a limiting factor toward commercialization, as other products such as CdTe exist on the market with toxic

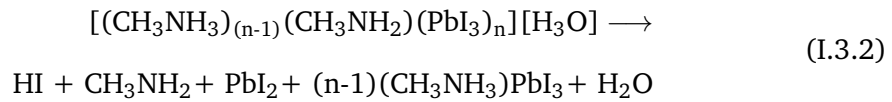
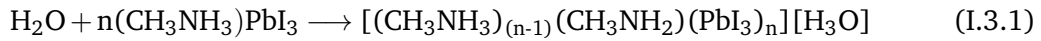
components and that there are other more significant sources of lead release into the environment than perovskite solar cells.<sup>82</sup> Still, the search for lead-free alternatives attracts interest from the research community.<sup>46,83–86</sup> Currently, one of the more promising alternatives is Sn; While Sn-based perovskites generally have electronic properties comparable to their Pb-based sisters, their band gaps are closer to the ideal values of the SQ limit ( $\sim 1.1$  eV -  $\sim 1.3$  eV), suggesting they may one day reach a higher maximum efficiency.<sup>61,87–89</sup> Presently, the main draw back to utilizing Sn over Pb in perovskite solar devices is the instability of  $\text{Sn}^{2+}$  species. While organic cation containing perovskite devices are still considered unstable (as discussed in the next section), the inclusion of Sn adds an additional instability to the mix.  $\text{Sn}^{2+}$  in  $\text{ASnX}_3$  architectures have a tendency to oxidize to  $\text{Sn}^{4+}$ , which results in unfilled mid gap states, p-type doping the material, lowering the efficiency.<sup>61,88</sup> Even so, Sn-based perovskites remains an attractive alternative to Pb,<sup>59,60,90,91</sup> and hopefully a solution will be found soon.

#### **1.3.4 Factors Limiting Commercialization: Structural Instability**

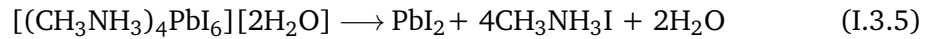
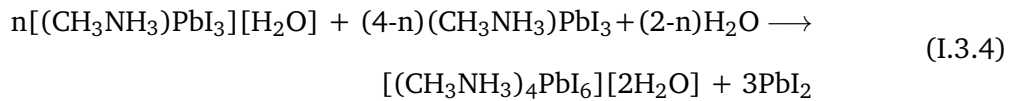
Unfortunately, the best performing perovskites are currently unsuitable for commercialization caused by their limited shelf life due to rapid degradation of the lattice in the presence of moisture, heat, and light/oxygen.<sup>92–100</sup> While there are other processes that affect the lattice and its performance, such as phase transformation<sup>99,101</sup> and hysteresis,<sup>85,102–105</sup> moisture, heat, and light/oxygen degradation remain key issues that must be addressed. Without any protective measures degradation can occur within minutes,<sup>96</sup> presenting an obvious barrier to real world application. Even when protective measures are introduced, champion perovskite solar devices still degrade decades quicker than commercially available silicon cells which have been projected to last over 25 years.<sup>106–111</sup> A sizable portion of this thesis has been aimed at offering new and investigating current proposed solutions to address the moisture degradation of the top performing perovskite materials, and is the main topic of Chapters 3 and 4.

The moisture instability of organic-inorganic hybrid halide perovskites is rooted in the chemical composition and physical properties of the organic A-site cations. These cations typically contain amines,  $\text{RNH}_3^+$  that, under the right conditions, act as Brønsted acids. While these amines are fairly basic ( $pK_b \leq 4$ ),<sup>112</sup> and the Brønsted acid/base reaction is heavily favored towards the protonated amine, the problem lies not in the acidity of the protic cations, but rather, in the volatility of the deprotonated amines. While the following degradation processes are often readily extendable to all

organic-inorganic hybrid halide perovskites containing a protic A-site cation,  $(\text{CH}_3\text{NH}_3)\text{PbI}_3$  is typically used as a representative example, and will be used here as such. At room temperature, methylamine,  $\text{CH}_3\text{NH}_2$ , (deprotonated methylammonium,  $\text{CH}_3\text{NH}_3^+$ ) has a vapor pressure of 2.63 bar compared to 0.21 bar for the volatile bench-top solvent acetone, calculated from the Antoine equation<sup>113</sup> using data available from the National Institute for Standards and Technology (NIST).<sup>114–117</sup> In general methylamine manages to escape its lattice position, leaving behind charged  $\text{PbI}_3^-$ . This makes it very difficult for the favored ammonium to reform, as it has traveled away from its lattice position. In-order to maintain charge neutrality, an  $\text{I}^-$  must be ejected from the  $\text{PbI}_3^-$  lattice, forming  $\text{PbI}_2$ . The exact physics of the decomposition pathway is still currently under debate, it may happen in a form similar to that just described, or may include a phase change of the  $\text{PbI}_3^-$  lattice at some point. The exact decomposition products are also currently under debate, and some researchers suggest that  $\text{I}^-$  leaves the lattice as  $\text{HI}$ :<sup>100</sup>



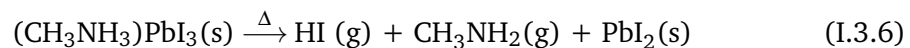
while others suggest it leaves as  $\text{CH}_3\text{NH}_3\text{I}$ :<sup>96</sup>



Regardless of decomposition pathway, there is universal agreement that  $\text{PbI}_2$  forms and a clear decrease in light-to-electricity conversion efficiency is observed. To make matters worse, as shown in both degradation pathways, at the end of a reaction cycle water regenerates, suggesting that a small amount of moisture can extensively degrade even a well sealed device. As a result, moisture degradation presents a major barrier to commercialization for volatile amine containing organic-inorganic hybrid halide perovskites. It has been proposed that the easiest way to prevent moisture degradation is to use an alternative moisture resistant A-site cation,<sup>41–43,55</sup> however, many

suggested alternatives lead to all inorganic devices that have yet to match the efficiency of the leading moisture sensitive organic devices. Another proposed option utilizes passivating agents at grain boundaries and surfaces of 3D and lower dimension perovskite architectures.<sup>106,108,118-120</sup> Again, devices utilizing these proposed methods have yet to achieve comparable efficiencies to leading moisture sensitive devices. In this thesis, a moisture-resistance alternative A-site cation is offered (Chapter 3) as well as an explanation as to why amine containing passivating agents should be avoided (Chapter 4).

A second degradation pathway for (CH<sub>3</sub>NH<sub>3</sub>)PbI<sub>3</sub> lattices is through heat, which can occur at temperatures as low as 60 °C,<sup>121</sup> well within the range of operating temperatures (-40 °C - +85 °C).<sup>111</sup> In thermal induced degradation, heat causes the organic components of the A-site cation to breakdown, which then vacate the system. Using thermal gravimetric analysis, two prominent decomposition pathways have been suggested:<sup>94,98,122</sup>

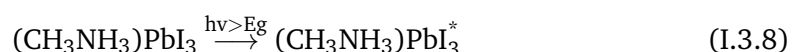


and

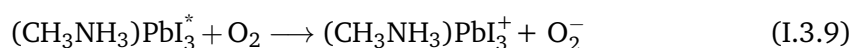


It is readily seen from both pathways that the main difference is the final decomposition product of CH<sub>3</sub>NH<sub>3</sub><sup>+</sup>. However, the most impactful product in both pathways is the PbI<sub>2</sub> lattice and its corresponding decrease in light-to-electricity conversion efficiency. In a fashion similar to that for moisture degradation, the inclusion of organic cations at grain boundaries and surfaces has been investigated as a strategy to bolster the thermal-resistance of perovskites.<sup>109</sup> It has also been suggested that self healing processes are necessary to undo the thermal damage sustained during operational hours.<sup>123</sup> Even so, the physics of thermal degradation is poorly understood, and further investigation is necessary to understand the efficacy of these solutions.

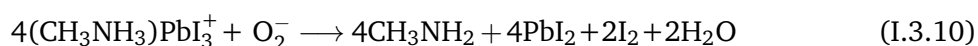
A third major form of (CH<sub>3</sub>NH<sub>3</sub>)PbI<sub>3</sub> lattice degradation occurs under illumination in the presence of O<sub>2</sub>. In the most accepted degradation pathway (CH<sub>3</sub>NH<sub>3</sub>)PbI<sub>3</sub> undergoes a redox reaction with O<sub>2</sub> initiated by the absorption of light. The degradation starts when light excites an electron in (CH<sub>3</sub>NH<sub>3</sub>)PbI<sub>3</sub>:



The excited electron is then transferred to O<sub>2</sub>:



The O<sub>2</sub><sup>-</sup> then reacts with the (CH<sub>3</sub>NH<sub>3</sub>)PbI<sub>3</sub><sup>+</sup> lattice forming PbI<sub>2</sub> and other gaseous products:<sup>92,93</sup>



It is unclear exactly the contents of the gaseous products,<sup>111</sup> but regardless, again, PbI<sub>2</sub> is formed, and a clear decrease in light-to-electricity conversion efficiency is observed. To make matters worse, one suggested degradation product is H<sub>2</sub>O, which could then feed back into the moisture decomposition pathway. As sunlight cannot be removed from the system for obvious reasons, the presence of O<sub>2</sub> must therefore be avoided. Such a task should be achievable when the device is vacuum sealed upon manufacturing.

While the exact form of the organic components, and how they mix with a third of halides, is unclear, it is clear that in all forms of degradation PbI<sub>2</sub> is present. As such, it is important to fully understand the electronic implications that PbI<sub>2</sub> has on an otherwise unperturbed lattice; This is investigated in Chapter 6. If significant headway can be made in addressing the current instabilities and the presence of lead in these devices, it would not be surprising to see perovskite solar cells gaining a sizable foothold in the consumer market in a rapid fashion.

#### **I.4 Investigating Perovskites**

It is clear from the above compendium that perovskite solar materials have a multitude of nontrivial hurdles to overcome before commercialization. The excellent electronic properties that give rise to their superior photovoltaic performance, however, makes finding solutions to these hurdles a worthwhile endeavor. The aim of this thesis is to help address some of these nontrivial issues, as well as bring to light other exceptional and unique electronic properties of the perovskite family. The computation methods used throughout act as a reference and a guide for understanding these unique properties as these methods excel at elucidating the atomic origins of the electronic properties of perovskites.

Here I propose that as the A-site cation only indirectly effects the electronic properties of organic-inorganic hybrid halide perovskites,<sup>63</sup> the key to addressing their

moisture instability while maintaining superior photovoltaic performance lies in engineering of alternative aprotic A-site cations. Furthermore, it is also proposed that the presence of  $\text{PbI}_2$  regions alone is insufficient to produce extensive erosion of the light-to-electricity conversion efficiency.

I start by offering an alternative aprotic organic A-site cation as a method to directly impede moisture based degradation. In-order for perovskites to be incorporated as a major component of a renewable energy grid as well as in the households of common consumers, it must exhibit a longevity and stability competitive with current high performing commercially available solar devices. In this regard, it has become necessary to address stability issues at a fundamental level to eradicate the problem, rather than dampen its effect. As such, the proposed alternative aprotic organic A-site cation should circumvent current moisture instability issues.

Next, the effect of commonly utilized passivation agents is investigated to determine their effect on the electronic properties of perovskite champion devices. While passivating agents offer a way to prolong the lifetime of perovskite devices, it is important that the inherent properties of the passivating agent do not interfere with device performance. As their electronic properties are dependent upon their chemical composition, special attention must be paid to problematic motifs that inhibit desirable electronic properties.

Following is an investigation of how the presence of  $\text{PbI}_2$  on an otherwise unperturbed lattice augments the electrical properties of the host. It is clear that when an organic-inorganic hybrid halide perovskite degrades, regardless of degradation pathway,  $\text{PbI}_2$  is always present. Detailed knowledge of the interaction between  $\text{PbI}_2$  and its host elucidates the effect  $\text{PbI}_2$  has on device performance. As  $\text{PbI}_2$  is unavoidable in degrading devices, a detailed understanding of the electronic interactions between the degradation product and the host is paramount.

Lastly, the optical properties of an exotic novel perovskite family is investigated. Originally, the intent was to investigate this novel family for its photovoltaic properties; However, it became readily apparent that this architecture is host to uncommon and desirable nonlinear optical properties. While they paint a negative picture for this exotic families future in photovoltaic applications, they hold hope as a potential novel material in the field of nonlinear optics. Additionally, they offer insight on the importance of current heavy metals used in the champion devices and their propensity for generating superior photovoltaic performance.

## CHAPTER II

### SOLVING CHEMICAL PROBLEMS WITH COMPUTERS

On the scale of daily life, the chemical processes that define reality as we know it are often hidden from plain sight. The advent of ever more advanced tools and theories accelerate the exploration and discovery of these processes and further our understanding of the chemical realm. Alongside experimental advances, the development of computer hardware has made available computing techniques and tools of increasing power used to compliment experimental understanding and guide materials synthesis. Some examples of atomic processes include exploring atomic motion and potential energy surfaces,<sup>104,124</sup> investigating electronic properties and transport in novel semiconductors,<sup>56,125,126</sup> determination of favorability of point defect formation,<sup>127,128</sup> and more. These processes and the methods that define them are distinguished by their underlying formulations that vary widely in their complexity and approximations, see Figure 2.0.1.

High level methods, such as those at the bottom left of Figure 2.0.1, use few to no approximations in the formulation of their underlying and applied theory, and are termed first principles methods. These methods, such as density functional theory (DFT) and *ab initio* methods, are based on quantum mechanical descriptions and provide solutions to Schrödinger's equation alongside a few approximations. In some cases (true *ab initio*) no approximations are used, but examples are exceedingly rare in the scientific literature due to their burdensome and often flat out insurmountable computational cost. DFT on the otherhand, calculates system properties to reliable accuracy, is widely available, and is extensively utilized by the scientific community in software packages such as the Vienna *ab initio* Simulation Package (VASP)<sup>129-132</sup> for solids and Gaussian for molecules.<sup>133</sup> In practice systems are limited by size, < 1000 atoms, and as their size increases solutions quickly become challenging to obtain.

Recovery of electronic properties in models too large for direct quantum chemical calculations can utilize semi-empirical methods that use approximations of interatomic interactions and a set of predetermined parameters. Semi-empirical methods are based

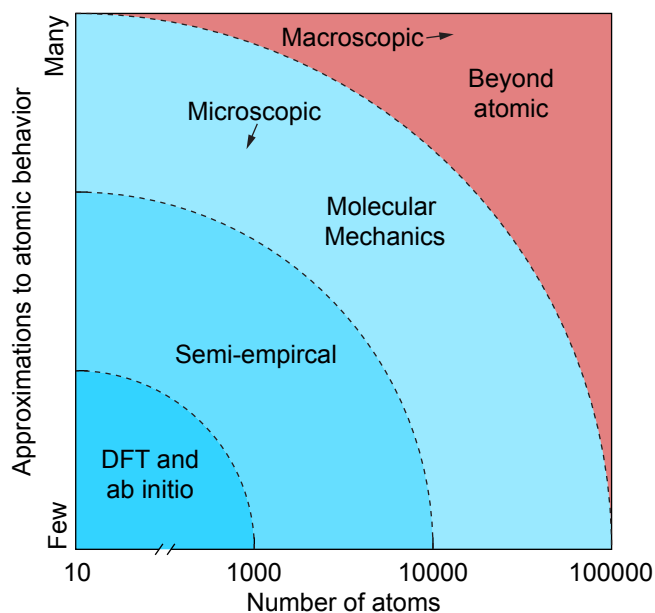


**Figure 2.0.1** Relationship between system size and approximations made to atomic behavior. High level methods such as first principles quantum chemistry (bottom left) generally make few approximations to atomic behavior and represent atomic characteristics fairly well, for example, bonding. Moving to the top right systems include more atoms and can represent larger motifs, such as proteins, but trade off accuracy of atomic descriptions. For example bonds in proteins are treated as a rigid spring and follow Hooke's law instead of being comprised of electrons.

upon the same Hartree-Fock formalism used in DFT but simplify or omit interactions. For example, the electron-electron interaction in Schrödinger's equation is omitted to reduce computational expense at the cost of accuracy. To correct for loss and approximations, semi-empirical methods are often parameterized to experimental data for a set of test molecules or desired properties. For even larger systems that are too cumbersome for semi-empirical methods, molecular mechanics methods can be employed. Here, parameterization results in a force field that when applied to a model, returns the potential energy. Force fields are comprised of analytical potentials parameterized from experimental data or high-level computational data, and are generally nontransferable and typically do not allow for the cleaving of bonds. They are however, exceptionally efficient at finding relaxed geometries and allow for the recovery of temperature dependent effects which aid in the quick determination of relative thermodynamic quantities such as structure stability. Such efficiency allows molecular mechanics methods to be applied to very large models, such as proteins, which are otherwise intractable in semi-empirical and first principles methods.

Beyond atomic descriptions are non-atomistic methods such as coarse graining and

simulation of macroscopic models. These methods generally have poor descriptions of atomic properties, if included. The work performed in this thesis utilizes exclusively DFT based methods, including *ab initio* molecular dynamics, for simulation of electronic and vibrational properties of solids in models that are less than a few hundred atoms in size. While DFT was originally conceived in the 1960's, less than 60 years ago, its origins stretch further back into the foundation of Quantum Mechanics. To date, applied DFT methods and software continues to evolve alongside computational hardware. Development of ever more powerful random access memory and central processing units allows high level methods to be utilized in systems of ever increasing size. As a result, DFT based methods continue to be honed and made more accessible to the scientific community.

## II.1 Fundamentals of Electronic Structure: Schrödinger's Equation

Prior to the advent of Quantum Mechanics, it was believed that Newton's descriptions in Classical Mechanics were capable of describing any observable phenomena that scientists could offer. There were growing suspicions throughout the 19<sup>th</sup> century that Classical Mechanics was not the finale of all physical science theory as scientists began to realize there were several notable phenomena that could not readily be rationalized by Classical Mechanics.<sup>134</sup> In the early 20th century, Max Planck, Albert Einstein, and others began crafting seemingly radical theories and descriptions in attempt to bridge the disconnect between seemingly inexplicable experimental findings and current theory. Such theories and descriptions, for instance the photoelectric effect and black body radiation descriptions, were fundamentally incompatible with the widely accepted Classical Mechanics explanations, and thus, Quantum Mechanics was born. At the heart of Quantum Mechanics is Erwin Schrödinger's many-body time dependent equation:<sup>135</sup>

$$\hat{H}\Psi(r,t) = i\hbar \frac{d\Psi(r,t)}{dt} \quad (\text{II.1.1})$$

where  $\hat{H}$  is the Hamiltonian operator,  $\Psi(r,t)$  is the wavefunction of the particle of interest,  $r$  is the particles position at time  $t$ ,  $i$  is the imaginary number, and  $\hbar$  is the reduced Planck's constant.

Schrödinger's many-body time dependent equation is often simplified to be time-independent to recover properties of static systems:

$$\hat{H}\Psi(r) = E\Psi(r) \quad (\text{II.1.2})$$

where  $\Psi(r)$ ,  $E$ , and  $\hat{H}$  are the ground state wavefunction, the ground state energy of an  $N$ -particle system, and again the Hamiltonian operator, respectively. Here, Schrödinger's equation takes the form of the eigenvector ( $\Psi$ ) eigenvalue ( $E$ ) problem, allowing the groundstate energy to be recovered using an appropriately defined Hamiltonian. In-order to generate the ground state energy of the system, the Hamiltonian must contain all relevant interactions describable within a system of interest through kinetic ( $T$ ) and potential ( $V$ ) energy terms:

$$\hat{H} = T_n + T_e + V_{ee} + V_{ne} + V_{nn} \quad (\text{II.1.3})$$

where  $T_n$  and  $T_e$  describes the kinetic energy of the nuclei and electrons, respectively,  $V_{ee}$  describes the potential energy interaction between two electrons,  $V_{ne}$  describes the potential energy interaction between a nuclei and an electron, and  $V_{nn}$  describes the potential energy interaction between two nuclei.

For a system comprised of nuclei,  $n$ , and electrons,  $e$ , potential energy terms are defined as:

$$\begin{aligned} V_{ee} &= \frac{1}{2} \sum_{e_1 \neq e_2}^i \frac{1}{|r_{ee}|} \\ V_{ne} &= - \sum_n^j \sum_e^i \frac{Z_n}{|r_{ne}|} \\ V_{nn} &= \frac{1}{2} \sum_{n_1 \neq n_2}^j \frac{Z_{n_1} Z_{n_2}}{r_{nn}} \end{aligned} \quad (\text{II.1.4})$$

where  $n$  and  $e$  are summed over their respective indexes,  $j$  and  $i$ , counting for the electron-electron ( $V_{ee}$ ), electron-nuclei ( $V_{ne}$ ), and nuclei-nuclei ( $V_{nn}$ ) pairwise electrostatic interactions. The strength of the electrostatic interaction is influenced by the distance,  $r$ , between the two interacting particles and the charge of the nuclei,  $Z_n$ , and electrons,  $-1$ . The Hamiltonian thus becomes:

$$\hat{H} = T_n + T_e + \frac{1}{2} \sum_{e_1 \neq e_2}^i \frac{1}{|r_{ee}|} - \sum_n^j \sum_e^i \frac{Z_n}{|r_{ne}|} + \frac{1}{2} \sum_{n_1 \neq n_2}^j \frac{Z_{n_1} Z_{n_2}}{r_{nn}} \quad (\text{II.1.5})$$

While the kinetic energy is still incompletely defined, Schrödinger's equation utilizing this Hamiltonian is in essence exact. There is one glaring problem however: as described, Schrödinger's equation is only mathematically solvable for a two particle system.<sup>136</sup> When there are only two particles in the system, the radial and angular functions of each particle that comprise the total wavefunction are separable. When more than two particles are present, the interdependence of particle interactions make

these functions inseparable. Therefore, Schrödinger's equation in its current form is mathematically unsolvable for systems with three or more particles. The solvable two particle system could take the form of two electrons, two nuclei, or a nuclei and an electron; The first two, however, are not representative of real world systems while the last describes the hydrogen atom. As a result, Schrödinger's equation is only exactly solvable for the hydrogen atom. As pretty much every single system of interest to chemists involves more than just a single hydrogen atom, approximations must be made.

### II.1.1 The Born-Oppenheimer Approximation

As the many-body Schrödinger equation is currently unsolvable for any system beyond a hydrogen atom, simplifying, relevant, and chemically intuitive approximations are required. Enter Born and Oppenheimer; In 1927 Born and Oppenheimer offered an approximation that decouples electronic and nuclear motion.<sup>137</sup> At its core, the approximation states that as the mass of the nuclei is significantly larger than that of an electron, electronic motion must occur on time scales much smaller than that of the nuclei. As a result, from the perspective of a moving electron, nuclei are essentially motionless, producing a static electromagnetic field for the electron to navigate.  $T_n$  therefore vanishes, and  $V_{nn}$  becomes some background constant. Additionally, the wave function ( $\Psi$ ) of the system can be separated into two components, a nuclear component ( $\Psi_n$ ) and an electronic component ( $\Psi_e$ ). Using only terms that are directly related to the electron, the Hamiltonian can be rewritten as the electronic Hamiltonian,  $\hat{H}_e$ :

$$\hat{H}_e = T_e + V_{ne} + V_{ee} \quad (\text{II.1.6})$$

Furthermore, the kinetics of the electron can be specified by the Laplacian,  $\nabla$ :

$$T_e = -\frac{1}{2} \sum_e^i \nabla^2 \quad (\text{II.1.7})$$

In the Born-Oppenheimer approximation, the electronic Schrödinger's equation takes the final form:

$$\hat{H}_e \Psi_e(r) = \left[ -\frac{1}{2} \sum_e^i \nabla^2 + \frac{1}{2} \sum_{e_1 \neq e_2}^i \frac{1}{|r_{ee}|} - \sum_n^j \sum_e^i \frac{Z_n}{|r_{ne}|} \right] \Psi_e(r) = E_e(r_n) \Psi_e(r) \quad (\text{II.1.8})$$

where the total electronic energy,  $E_e$ , is determined for a set of fixed nuclear coordinates,  $r_n$ .

Unfortunately, the Born-Oppenheimer approximation does not fully resolve the problem of inseparability of Schrödinger's equation. Only the contribution of the nuclear-nuclear and the nuclear-electron interactions to the problem have been addressed, the components of the electron-electron interaction remain inseparable in the Born-Oppenheimer approximation. Ergo, additional approximations are still necessary.

### II.1.2 The Method of Hartree-Fock and the Slater Determinate

In 1928, one year after Born and Oppenheimer introduced their approximation, Hartree presented an approximation that would help tackle the remaining inseparability of Schrödinger's equation.<sup>138</sup> At its core this approximation, also known as the Hartree-Fock (HF) approximation, treats a single electron in an  $n$ -electron system as being present in a mean field produced by both the nuclei and the  $n - 1$  electrons surrounding it. This circumvents the inseparability issue as each pairwise interaction instead contributes to a singular surrounding field. As a result when electrons are present in this field they interact with only the field. This result is of great importance as it implies that electrons move independently of one another, or in an uncorrelated fashion. Hartree originally introduced the approximate electronic wavefunction ( $\Psi_0$ ) as being constructed from the product of  $n$ -electronic wavefunctions,  $\varphi$ :

$$\Psi_0 = \varphi_0(e_1)\varphi_0(e_2)\varphi_0(e_3)\cdots\varphi_0(e_n) \quad (\text{II.1.9})$$

Not only are the electrons in the Hartree approximation uncorrelated, they are also without spin. The lack of spin in its own right is another large problem as systems with unpaired electrons cannot be described, and no magnetic properties can be calculated. In 1930, Fock<sup>139</sup> and Slater<sup>140</sup> introduced spin into the approximation by describing the single electron wavefunctions as spin-orbitals dependent upon the spatial coordinates of the electrons,  $x$ :

$$\Psi(x_1, x_2, x_3, \cdots, x_n) = \varphi_1(x_1)\varphi_2(x_2)\varphi_3(x_3)\cdots\varphi_n(x_n) \quad (\text{II.1.10})$$

This wavefunction is much closer to describing a real world system, but still lacks antisymmetry requirements. Without meeting antisymmetry requirements, the Pauli exclusion principle is violated as two electrons of the same spin can occupy the same orbital.

Slater showed that taking the linear combination of the single electron

wavefunctions resulted in a system wavefunction,  $\Psi$ , that fulfilled antisymmetry requirements. In a two electron system this takes the form:

$$\Psi(x_1, x_2) = \frac{1}{\sqrt{2}} [\varphi_1(x_1)\varphi_2(x_2) - \varphi_1(x_2)\varphi_2(x_1)] = \frac{1}{\sqrt{2}} \begin{vmatrix} \varphi_1(x_1) & \varphi_2(x_1) \\ \varphi_1(x_2) & \varphi_2(x_2) \end{vmatrix} \quad (\text{II.1.11})$$

where the matrix on the right-hand side is called the Slater determinate. The general form of the Slater determinate for an n-electron system is described by:

$$\Psi(x_n) = \frac{1}{\sqrt{n!}} \begin{vmatrix} \varphi_1(x_1) & \varphi_2(x_1) & \varphi_3(x_1) & \cdots & \varphi_n(x_1) \\ \varphi_1(x_2) & \varphi_2(x_2) & \varphi_3(x_2) & \cdots & \varphi_n(x_2) \\ \varphi_1(x_3) & \varphi_2(x_3) & \varphi_3(x_3) & \cdots & \varphi_n(x_3) \\ \vdots & \vdots & \vdots & \ddots & \vdots \\ \varphi_1(x_n) & \varphi_2(x_n) & \varphi_3(x_n) & \cdots & \varphi_n(x_n) \end{vmatrix} \quad (\text{II.1.12})$$

Such determinate described the exchange of electrons exactly, and has been termed 'Fock Exchange'. While Fock exchange is included at very high levels of theory, it comes at great computational expense, and thus cannot readily be used for any given system. As such, simplifying approximations are now required.\*

## II.2 Density Functional Theory

In 1964, roughly 30 years after Hartree, Fock, and Slater introduced the HF formalism, Hohenberg and Kohn showed that for an interacting electron gas in an external potential, using only the ground state electronic density,  $\rho_0$ , the ground state wavefunction can be recovered.<sup>141</sup> This concept is the heart of density functional theory (DFT). In essence, DFT is a first-principles method, as it is derived with no parameterization, and in principle, is exact. Problematically, under Hohenberg and Kohn the mathematical form of the DFT functional remains unknown.<sup>142</sup> Therefore, in practice, the formalism of Kohn and Sham is utilized. Kohn and Sham construct the ground state energy as a function of the electron density,  $\rho$ :

$$E_0[\rho_0] = V_{ne}[\rho_0] + V_{ee}[\rho_0] + G[\rho_0] \quad (\text{II.2.1})$$

where  $G[\rho_0]$  is a universal functional of the density. The nuclear-electron term,  $V_{ne}[\rho_0]$ , expressed as the classical electrostatic potential, the electron-electron interaction,

---

\*While there are Post-HF methods that address some of the shortcomings of HF, their discussion is excluded as they are not utilized in this thesis.

$V_{ee}[\rho_0]$ , and the universal functional of the density,  $G[\rho_0]$ , are defined as:

$$\begin{aligned} V_{ne}[\rho_0] &= \int V_{ext}(r)\rho_0(r)dr \\ V_{ee}[\rho_0] &= \frac{1}{2} \int \int \frac{\rho_0(r_1)\rho_0(r_2)}{|r_1 - r_2|} dr_1 dr_2 \\ G[\rho_0] &= T[\rho_0] + E_{xc}[\rho_0] \end{aligned} \quad (\text{II.2.2})$$

where  $r_1$  and  $r_2$  are the coordinates of electrons 1 and 2, respectively,  $T[\rho_0]$  is the kinetic energy associated with the density, and  $E_{xc}[\rho_0]$  is the exchange-correlation energy. Kohn and Sham used a reference electron density,  $\rho^{ref}$ , to represent the real electron density,  $\rho^{real}$ , however, the reference electron density is non-interacting and is constructed from the sum of one-electron wavefunctions:

$$\rho^{real} = \rho^{ref} = \sum_{e=1}^{2e} \varphi_e^{KS}(r)^2 \quad (\text{II.2.3})$$

where  $\varphi^{KS}$  are the Kohn-Sham spatial-spin orbitals. Consequently, the electron kinetics of the reference system and the quantum mechanical deviation of the classical Coulombic energy result in the exact mathematical form of  $E_{xc}[\rho_0]$  being unknown. As the exact mathematical form of  $E_{xc}[\rho_0]$  is unknown, Schrödinger's equation remains unsolvable, and further approximations are required. As such, empirically derived equations, called functionals, are utilized to calculate  $E_{xc}[\rho_0]$ .

## II.2.1 Functionals

Since the exact mathematical form of the exchange correlation energy is unknown, its form has been approximated through the manifestation of exchange-correlation functionals. The complexity of the functional depends upon the complexity of the components in its makeup. Given an arbitrary system, one can choose to treat its exchange-correlation energy to varying degrees of rigor.

One of the most basic approximation is that the electron density is evenly distributed through space, forming the homogeneous electron gas (HEG). The HEG approximation works well in tandem with the local density approximation (LDA), which uses an empirically derived function for the exchange and correlation,  $F_{xc}$ , in a HEG. This empirical function evaluates the electronic density at only the supplied coordinates,  $\rho(r)$ . For example, the Perdew-Wang functional PW92<sup>143</sup> utilizes LDA to

provide an estimate of the exchange and correlation defined as:

$$E_{xc}^{LDA} = \int \rho(r) F_{xc}[\rho(r)] dr \quad (\text{II.2.4})$$

LDA is great for describing materials with smoothly and slowly changing electron density, such as metals which act as a uniform sea of electrons, but for systems with unevenly distributed electrons or regions that lack density at all (polar materials, nonperiodic molecules, vacuous materials, etc.) this approximation falls short. As such, LDA based functionals see only occasional use in modern semiconductor and molecular modeling.

The next step up from LDA are functionals that utilize the generalized gradient approximation (GGA). Here, the exchange-correlation functional,  $F_{xc}$ , is evaluated at the electron density of the supplied coordinates,  $\rho(r)$ , in tandem with its local gradient,  $\nabla\rho(r)$ :

$$E_{xc}^{GGA} = \int \rho(r) F_{xc}[\rho(r), \nabla\rho(r)] dr \quad (\text{II.2.5})$$

These functionals are more capable of describing regions of quickly changing electron density than their LDA counterparts. As a result, GGA functionals such as PBE,<sup>144</sup> PBEsol,<sup>145</sup> and PW91<sup>146</sup> see more use in the community than pure LDA functionals. An extension of the GGA functionals are the meta-GGA functionals, which include the electron density of a coordinate alongside its first and second derivatives. Meta-GGA functionals include TPSSH<sup>147</sup> and the M06<sup>148</sup> suite of functionals.

A further expansion of the GGA functionals is to include a portion of HF exchange in the exchange-correlation functional taking advantage of the ability to describe the exchange and correlation separately:

$$E_{xc} = E_x + E_c \quad (\text{II.2.6})$$

Doing so gives rise to hybrid functionals, that are part GGA, part HF. One example of a hybrid functional, PBE0,<sup>149</sup> mixes a portion of HF exchange in with exchange of the PBE functional:

$$E_{xc}^{PBE0} = aE_x^{HF} + (1-a)E_x^{PBE} + E_c^{PBE} \quad (\text{II.2.7})$$

where  $a$  is a mixing parameter and has been found to be optimum at a value of 25% for PBE0. The idea behind hybrid functionals, as shown in Equation II.2.7, is to improve upon the pure GGA descriptions through the inclusion of HF exchange, which is in

essence, exact.

Another popular choice for hybrid functionals is the HSE functional.<sup>150</sup> HSE applies a screened Coulombic potential to the exchange of the exchange-correlation function, screening long-range interactions. All other Coulombic interactions within the Hamiltonian are not screened. The function is split into short-range and long-range components:

$$\frac{1}{r} = \frac{f_{error}^{SR}(\omega r)}{r} + \frac{f_{error}^{LR}(\omega r)}{r} \quad (\text{II.2.8})$$

where  $f_{error}^{SR}$  and  $f_{error}^{LR}$  are the error functions for the short-range (SR) and long-range (LR) components, respectively.  $\omega$  is an adjustable parameter that controls the short-rangeness: when  $\omega = 0$ , the long-range component drops out and terms become purely short ranged. When  $\omega \rightarrow \infty$ , the opposite is true. HSE06 is an extension of PBE0 where the correlation in PBE0 remains unaltered and the exchange is the main focus:

$$E_x^{PBE0} = aE_x^{HF} + (1-a)E_x^{PBE} \quad (\text{II.2.9})$$

Heyd, Scuseria, and Ernzerhof start their deviation from PBE0 by expanding all exchange terms into their short- and long-range components:

$$E_x^{PBE0} = aE_x^{HF,SR}(\omega) + aE_x^{HF,LR}(\omega) + (1-a)E_x^{PBE,SR}(\omega) + (1-a)E_x^{PBE,LR}(\omega) \quad (\text{II.2.10})$$

Numerical examination for realistic values of  $\omega$  indicate that when  $\omega = 0.15$  both the HF and PBE long-range exchange components are small, tend to cancel each other out, and can therefore be neglected:

$$E_{xc}^{HSE} = aE_x^{HF,SR}(\omega) + (1-a)E_x^{PBE,SR}(\omega) + E_x^{PBE,LR}(\omega) + E_c^{PBE} \quad (\text{II.2.11})$$

In reality,  $\omega = 0.207$  is used alongside  $a = 25\%$ , giving rise to HSE06. In this thesis, a combination of the GGA functional PBEsol and the hybrid functional HSE06 are used. Great success has been had using GGA functionals to compute geometric models followed by hybrid functionals to recover their corresponding electronic properties. Compared to hybrid functionals, GGA functionals offer a faster time to convergence for similar supplied structural parameters. Additionally, they have significantly lower memory requirements, allowing fewer computational resources to be used.

## II.2.2 Basis Sets

So far, various approximations to the Schrödinger equation, including the empirically derived estimates for the unknown exchange-correlation energy have been presented. The final approximations derive the energy, and therefore relevant properties of interest, as a function of the electron density. In DFT, the electron density is built from the sum of Kohn-Sham orbitals, see Equation II.2.3. The mathematical representation of such orbitals, and thus the mathematically workable form of the electron density, is called a basis set. Basis sets are formed through the sum of mathematical functions, again see Equation II.2.3, and can be as simple or complex as desired. The number of mathematical functions included is directly proportional to the size of the basis set, more functions result in a larger basis set. While a larger basis set generally results in more accurate outcomes, the accuracy gained does not always outweigh the additional computational expense required. Ergo there is an art related to choosing a basis set of sufficient size to ensure reliable outcomes, but not so large that time-to-solution becomes intractable. Previously, basis sets for molecular systems were constructed from either Slater- or Gaussian-type functions that were mathematically or analytically opportune.

For atomic systems, say the hydrogen atom, constructing a basis set from hydrogen orbits (1s, 2s, 2p, etc.) can provide quick and convenient solutions to Schrödinger's equation. For atomic and molecular systems larger than hydrogen (functionally this includes all other elements), filled hydrogen orbitals for atoms or a linear combination of atomic orbitals (LCAO) for molecules are used to form a basis set. The choice of which orbitals or additional functions to include has a direct impact on which outcomes can be sampled or which system properties can be included. For example, without polarization functions, polar systems cannot be completely described. A LCAO works well for molecular systems but for systems with periodic features a periodic description works better.

In contrast to atom-centered orbitals, periodic basis sets are comprised of periodic waves, described by periodic functions with repeating features. The recurrent features of periodic waves are more practical to represent a periodic solid. These periodic waves, also known as planewaves, are waves/oscillations of frequency:

$$\Psi = e^{ikr} = \cos(kr) + i \sin(kr) \quad (\text{II.2.12})$$

The sum of the planewaves within the model define the basis set for the periodic solid. Similar to atomic basis sets, including more functions (waves) in the planewave basis set increases the accuracy of solutions. Again, more functions (waves) also leads to longer time-to-solution. Typically, more waves are included by increasing the cut-off energy of the planewave, or the planewave cut-off. The planewave cut-off is given as an energy, and waves of energy higher than the cut-off are excluded from the basis set. The optimal value for a planewave cut-off is determined by varying the cut-off energy till the wavefunction, a property of interest, or the total energy exhibits minimal change, *e.g.* the difference in total energy between two cut-off values is less than a predetermined threshold. At this point the time-to-solution is minimized while the accuracy is maximized. This typically occurs between cut-off energies of 400 to 600 eV. For each element there also exists a minimum energy cut-off. The minimum energy is the energy required to describe that electron in the free atom model. Below the minimum, results, if obtainable, are unreliable.

One issue with planewaves that include functions for all electrons is that core electrons are described by high frequency waves which are computationally demanding. To reduce the computational demand of the core electrons, they are approximated by a single, static potential called a pseudopotential. The idea is that core electrons do not participate in bonding, and thus an accurate and full description adds little information on electronic properties. As such, the core is treated as a frozen core, described by a single potential that interacts with surrounding bodies. In this thesis, the projector augmented-wave (PAW) method<sup>151</sup> is extensively used. The PAW method is a way of addressing the high frequency problem of the core region: the overall wavefunction is simple to calculate between atoms and in the valence region, but the wavefunction in the core region is difficult due to strong oscillations. In the core region, also known as the augmentation region, a smooth wave is projected onto the strong oscillations through a linear transformation operator. This operator only augments the core waves as it is only non-zero within the core region. After augmentation, the overall wavefunction is more smoothly varying reducing the computational demand.

### **II.3 The Solid State and Periodic Imaging of the Infinite Solid**

At the atomic view, an ideal solid is infinite. Computationally this is problematic as representing an ideal solid in its entirety is impracticable. Taking advantage of the symmetry of crystalline solids allows the ideal to be compressed to a small repeating

image, called a unit cell. The unit cell is constructed through specifying atomic coordinates in relation to an origin and through addition of vectors that comprise a bounding box. In practice, for novel materials the unit cell is often obtained by a crystallographer through single crystal X-ray diffraction (XRD) or neutron diffraction. The computational chemist can then use DFT calculations to collect electronic information of the solid such as the total energy, the band structure, the density of states, optical properties, and more.

Mathematically, the unit cell is used to reconstruct the ideal solid through symmetry operations and unit cell translation. When translating the unit cell from point  $P$  with coordinates  $r$  by a lattice vector  $\bar{a}$ , any number of times,  $n$ , one returns to an identical location and cannot differentiate between the old and the new image. Mathematically this is shown as:

$$P(r + n\bar{a}) = P(r) \quad (\text{II.3.1})$$

The boundary that separate the unit cell and its images is called the periodic boundary condition (PBC). The unit cell when translated about its lattice vectors across the PBC *ad infinitum* returns the infinite solid, depicted in Figure 2.3.1a. Not all forms of symmetry lead to a unit cell, however. In general, odd sets of rotational symmetry, such as tri-, pent-, sept-, etc., leads to void space when tiling unit cells, shown in Figure 2.3.1b. In some cases this issue can be resolved by redrawing the unit cell. In practice, these unit cells contain anywhere from one to a few hundred atoms, depending on the symmetry of the system. For example, the unit cell of NaCl only contains two atoms, a single Na and a single Cl. Typically higher symmetry leads to lower atom count in the unit cell for chemical formulas with similar number of unique elements.

As the potential that is used to describe the electron density, and thus the wavefunction, is constructed from periodic planewaves, the same mathematical relationship holds for the wavefunction, as described by the Born-von Kármán equation:

$$\Psi(r + n\bar{a}) = \Psi(r) \quad (\text{II.3.2})$$

It is convenient for periodic solids to have periodic coordinates, a periodic potential, and a periodic wavefunction. The functional form of the repeating wavefunction is

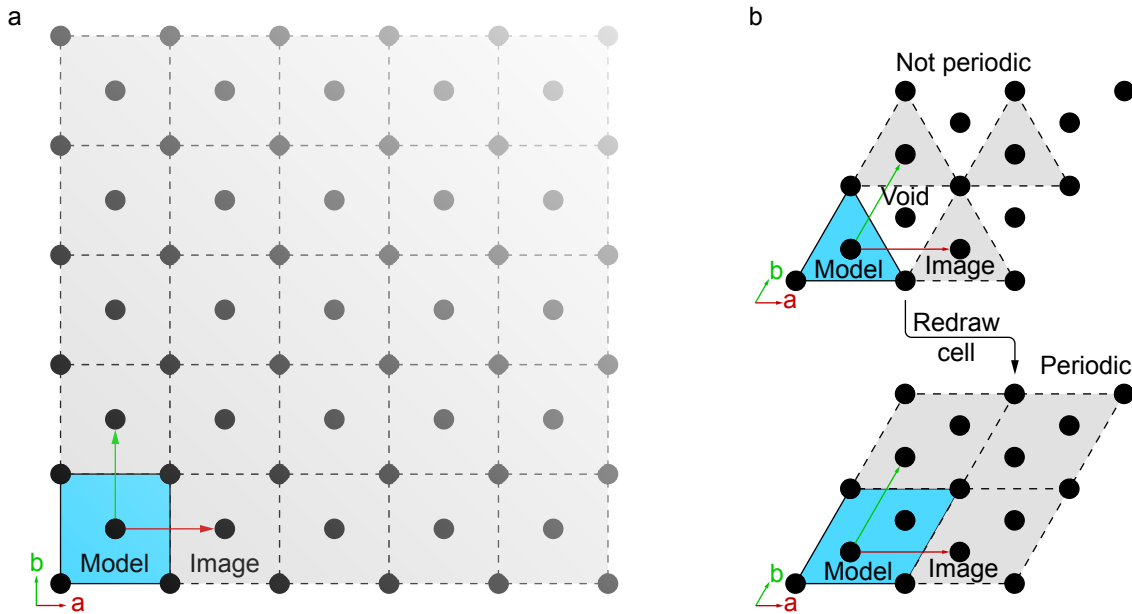


**Figure 2.3.1** a) Translation of the model, blue, along the lattice vectors, red and green, giving rise to periodic images, grey, returning the infinite solid. b) Translation of the triangular model gives rise to void space, colorless, and thus the model cannot be periodic. Redrawing the boundaries of the cell allows for the void space to be removed, making the model periodic.

described by a Bloch wave, presented by Felix Bloch in 1929:<sup>152</sup>

$$\Psi_{nk}(r) = e^{ikr} u_{nk}(r) \quad (\text{II.3.3})$$

where  $n$  is an index,  $k$  is the planewave vector,  $i$  is the imaginary number, and  $u$  is the periodic function.  $u$  sets the periodicity of the lattice while  $e^{ikr}$  describes the long-range interactions throughout the lattice.

### II.3.1 Reciprocal Space

Reciprocal space, sometimes called Fourier space, momentum space, k-space, or inverse space, is the Fourier transform of real space. Reciprocal space offers a convenient way to explore the electronic interactions between the unit cell and its surrounding medium. Waves in real space become points in reciprocal space, and vice versa. As such, the reverse Fourier transform of a point in reciprocal space yields a wave in real space. This real space wave has a phase which can constructively/destructively interact with its surrounding medium, yielding information on the longer range electronic interactions in the solid as a function of system energy. The understanding of reciprocal space and constructive/destructive wave interactions inherently finds a home in physics and mathematics. Roald

Hoffmann was very successful in translating these ideas into the language of chemists.<sup>153</sup> Hoffmann described the unit cell as being comprised of orbitals with their own phases. Each orbital in turn can be mathematically described by a wavefunction, and the sum of the orbital wavefunctions make up the total wavefunction of the unit cell. How these wavefunctions are augmented by their surrounding medium depends upon the wavefunctions produced by adjacent unit cells (phase, orbital orientation, orbital content, etc.). One can image the simplest case of a unit cell comprised of a single s-orbital. When two unit cells are placed side-by-side, if the cells are of different phase, then there will be an anti-bonding interaction which raises energy, see Figure 2.3.2a. Conversely, if the cells are the same phase, there will be a bonding interaction, lowering the energy. The energy for various interactions can be plotted to gain insight into material properties, which will be discussed in section II.4.1. A simple example is given in Figure 2.3.2b. For the more complicated case of a unit cell containing a p-orbital, the interactions are not the same. The direction and orientation of the p-orbitals within adjacent cells relative to one another will determine their bonding interactions. For example, p-orbitals aligned side-by-side without changing phase results in bonding behavior, whereas changing phase results in anti-bonding behavior. The opposite is true when looking p-orbitals aligned end-to-end. It can therefore be seen that orientation and relative symmetry plays a very important part in sampling orbital and cell interactions. For cells containing a multitude of complex orbitals (d-, f-, etc.) as well as hybridized orbitals, their interactions, and thus energy, is not readily apparent and is exceptionally difficult to discern without computational aid.

The important points in reciprocal space are determined by the symmetry elements of the real space model, and classify the model's space group. Reciprocal space points of very high symmetry, called k-points, exist within a Brillouin zone, and give shape to the unit cell in reciprocal space. The smallest Brillouin zone is called the 1<sup>st</sup> Brillouin zone and often, one only needs to look within the 1<sup>st</sup> Brillouin zone to gather all the desired information of interest. The k-points of the Brillouin zone allow for direction dependent interaction sampling in the real space model through  $k$  in Equation II.3.3. It is important to note that the coordinates of k-points are unique for each space group and its representation will sample different interactions in models of different symmetry. For example, the R point in the  $P_{nma}$  space group (#62) has a coordinate of (0.5, 0.5, 0.5), but in the  $P_{4/mnc}$  space group (#126) it has a coordinate of (0.0, 0.5, 0.5). There is only one k-point that is universally applicable in every space group, the  $\Gamma$

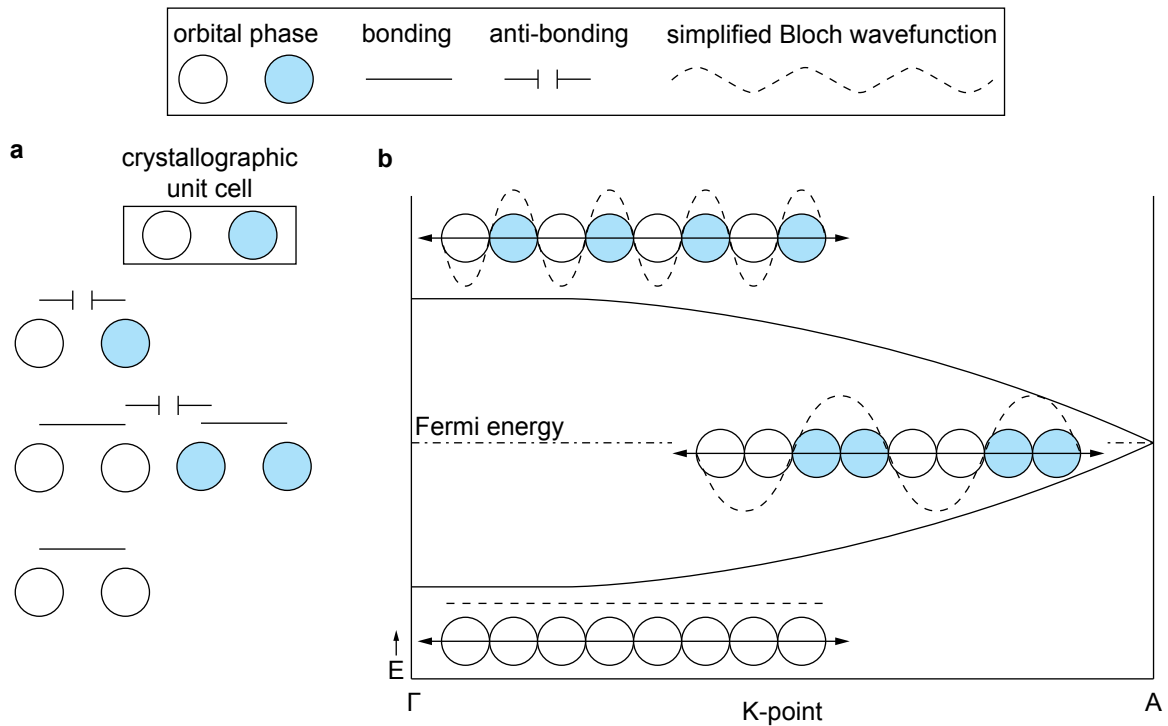


**Figure 2.3.2** a) Bonding and anti-bonding configurations for a 1D chain of s-orbitals. b) Corresponding band structure of the crystallographic unit cell containing two s-orbitals.

point with coordinates of  $(0,0,0)$ . The  $\Gamma$  point is at the Brillouin zone center for every space group and is always specified by the same symbol and coordinates.  $\Gamma$  is a unique k-point as it does not change the phase of the wavefunction for any interaction it samples. Rather, it treats all periodic images across the PBC as if they were in the same phase. There is no other k-point that does this and as a result,  $\Gamma$  should always be sampled. If  $\Gamma$  is not sampled it will be difficult to make reference to any direction dependent interactions as the total energy of the model will be ill defined.

Reciprocal space and real space are inversely related. As real space grows reciprocal space shrinks, as real space shrinks reciprocal space grows. As a result, very large models require only small samples of reciprocal space to yield pertinent long-range electronic information. This can be envisaged through the total number of interactions presented inside the unit cell. The larger the unit cell, the more interactions present within. Additionally, as the unit cell grows, the unit cell begins to incorporate interactions that are longer in range. One can imagine that modeling a cell of large size would encompass an interaction of long enough range to sufficiently describe the long-range interactions present in the material. As a result, only a very small portion of reciprocal space, specifically only  $\Gamma$ , would need to be sampled to

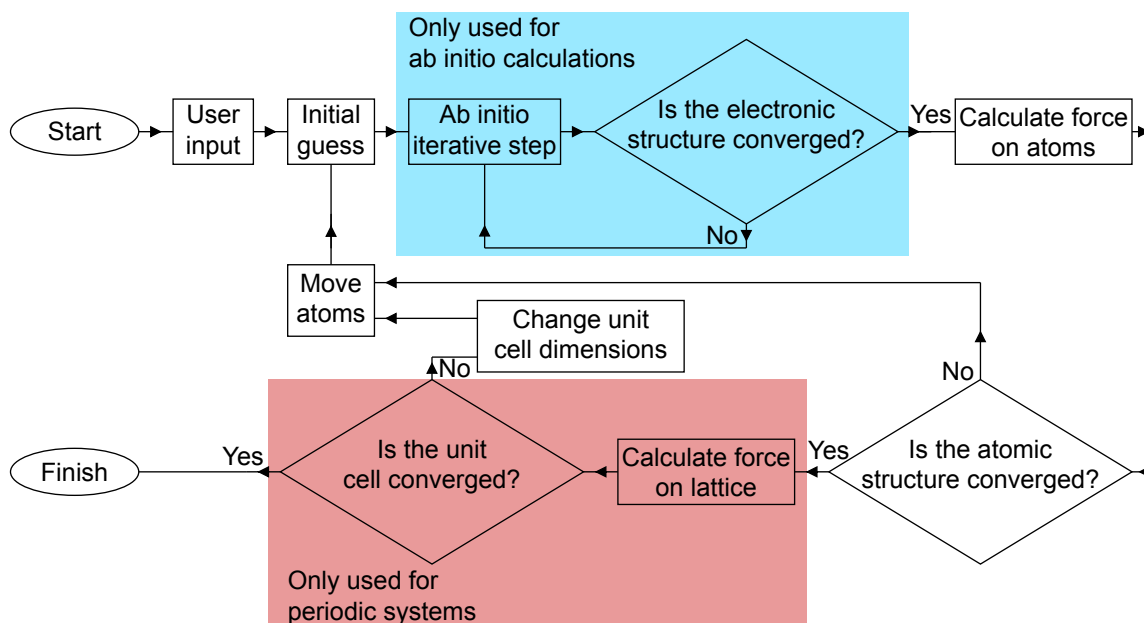


**Figure 2.3.3** General optimization routine utilized to find the ground state geometry of a supplied model. The user starts by generating a model (coordinates, basis, list of program instructions, etc.), then an initial guess of the wavefunction is generated. This wavefunction is converged iteratively, then the forces on each atom are calculated. If the forces have not been minimized below a stipulated threshold, the process is repeated after the geometry is updated as guided by the calculated forces. Once the atomic forces are converged, the unit cell convergence is checked. If it is unconverged, the lattice parameters are updated, and the process repeats until unit cell convergence is met, at which point the process is complete and a ground state geometry is obtained.

recover all the electronic information necessary. As such, only the interactions within the unit cell of very large size are required to describe long-range interactions within a solid.

### II.3.2 System Optimization and the Variation Principle

The acquisition of electronic properties (carrier transport, excited states, etc.), are dependent upon an accurate description of the ground state geometry. Typically, the starting geometry for a model is not the ground state geometry, meaning that the model must be optimized before relevant properties can be calculated. Generally, geometries are optimized following a routine close to that depicted in Figure 2.3.3. There are many different flavors of optimizers as well as parameters a user can play with (electron mixing, force scalers, induced pressure, etc.), generally however they all attempt to move the energy of the structure down the potential energy hill, *e.g.* minimize the system energy.

To minimize the systems electronic energy, and thus obtain an optimized (ground

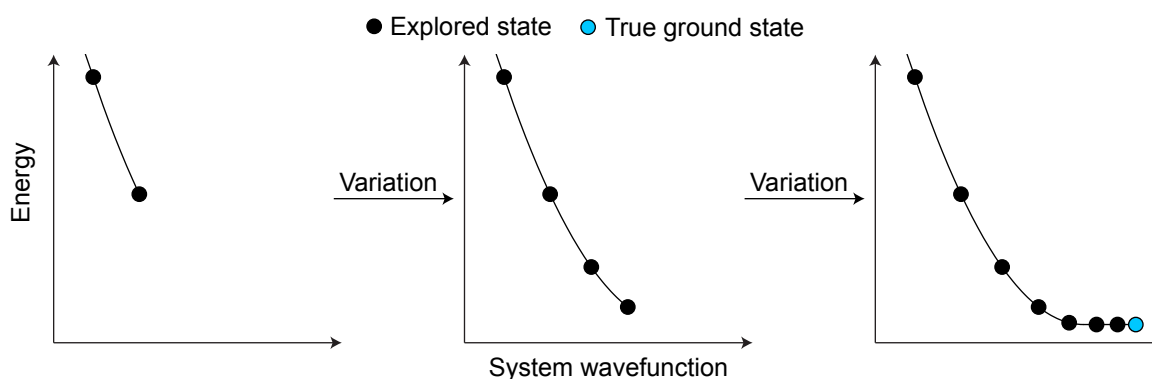


**Figure 2.3.4** Depiction of the variational principle. For a given state, the wavefunction is varied and the expectation value of the new state is calculated. If the energy of the new state is lower than the previous, it becomes the new ground state. This is continued until the change in energy is below a stipulated threshold. At this point, it is expected that the recovered wavefunction with the lowest energy is similar to that of the true ground state.

state) electronic structure for a given geometry, the variational principle is invoked.

The variational principle states that the true ground state energy,  $E_0$ , is always less than or equal to the expectation value of a trial Hamiltonian. The expectation value for the Hamiltonian ( $\hat{H}$ ) is the energy of the supplied wavefunction:

$$E = \frac{\langle \Psi | \hat{H} | \Psi \rangle}{\langle \Psi | \Psi \rangle} \quad (\text{II.3.4})$$

In the variational principle, when an initial guess wavefunction ( $\Psi_1$ ) with an expectation value of  $E_1$  is varied to a new wavefunction ( $\Psi_2$ ) with a new expectation value of lower energy ( $E_2 < E_1$ ), then  $\Psi_2$  is the new approximate ground state. This concept is depicted in Figure 2.3.4. In practice this is done by solving Schrödinger's equation using an initial guess wavefunction to produce a more accurate next guess. The wavefunction is thereby varied in a step-wise fashion ( $\Psi_1 \rightarrow \Psi_2 \rightarrow \Psi_3 \rightarrow \dots \rightarrow \Psi_n$ ) using the previous solution and expectation values of lower and lower energy ( $E_1 > E_2 > E_3 > \dots > E_n$ ) are returned. This is repeated until the difference between the newest guess and the previous guess is below a predetermined threshold ( $E_{(n-1)} - E_n < \text{threshold}$ ). Once this threshold is reached, the electronic structure is considered converged. This is called the self-consistent field (SCF) procedure. The atomic coordinates are then varied using the forces experienced by each atom as a guide, and the electronic structure minimization is restarted for the new geometry. This continues until the both the electronic structure and the atomic forces are simultaneously minimized, at which point the structure is considered optimized.

## II.4 Tools to Analyze Solid State Properties

At the core of solid state computational chemistry there are a multitude of functional tools used to analyze and understand complex properties of bulk solids. These tools typically rely on accurate ground state geometries. Presented are a few techniques utilized in publications present in this thesis, their theoretical underpinnings and noteworthy characteristics are given. The number of tools available to computational chemists are not limited to those presented here; On the contrary, libraries of text could be accumulated on just a few select methods. As hardware becomes more powerful and underlying theory continues to develop, the tools and methods available to computational chemists continue to expand.

### II.4.1 Band Structure and Density of States

The electronic band structure and density of states are the hallmark of electronic structure calculations and are used extensively in the scientific literature. At its core, electronic band structures measure how the energy of bands, comprised of orbital interactions, change throughout the material. Such descriptions are particularly useful in elucidation of semiconductor electronic properties at the atomic level.

A fundamental tool, the band structure, is a measure of how the orbital phases and interactions within a material change as a function of reciprocal coordinate. How quickly the energy changes, often described as curvature or dispersion, offers insight into the orbital interactions in real space directions. As orbital interactions raise and lower the energy of a system, the lack of energy change suggests that there is little to no interaction, depicted by a flat band in complex band structures such as that in Figure 2.4.1. As such, there is little orbital interaction in the corresponding real space direction. Conversely, the faster the energy changes, depicted by a curvy or disperse band, indicates very strong interaction in the real space direction. Therefore, how the energy changes is indicative of how charge carriers can move throughout the system. Intuitively, if there is no interaction (a flat band), charge carriers cannot easily move through noninteracting orbitals in the material. It is unlikely then, that the material will exhibit band transport, which is when a charge carrier moves through a seemingly continuous orbital throughout the material. One typically is interested in specific k-points or the pathway between a set of k-points. It is therefore generally considered good practice to construct a band structure from a series of predetermined k-points using interactions that are deemed important in the material as a guide.

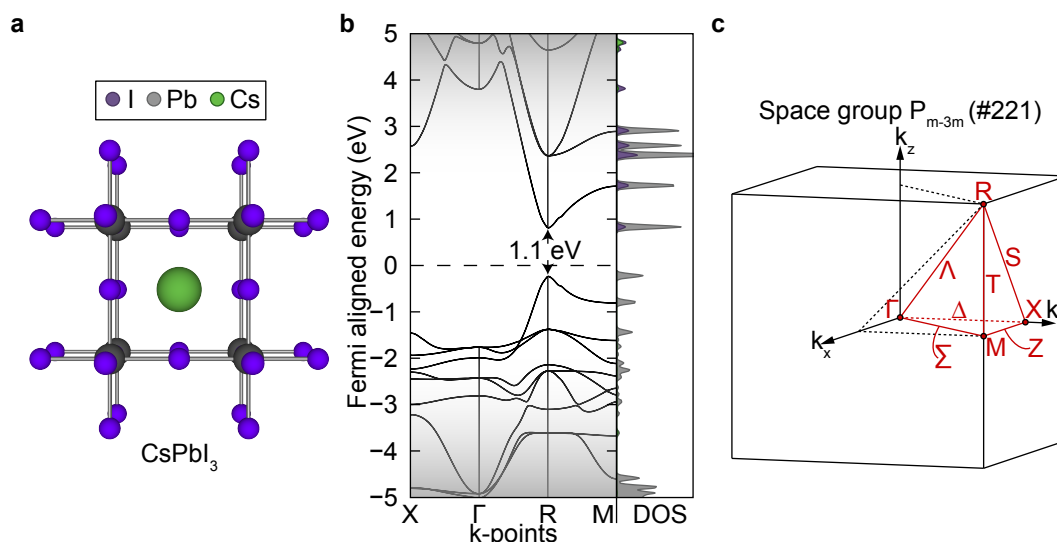


**Figure 2.4.1** a) Cesium lead iodide ( $\text{CsPbI}_3$ ) shown in its cubic phase. b) Band structure and density of states for cubic  $\text{CsPbI}_3$  calculated using the HSE06 (PBE+43% HF) hybrid functional and spin-orbit coupling effects. The density of states is calculated at the high symmetry points only. c) High symmetry points of space group  $P_{m-3m}$  (#221) within the 1<sup>st</sup> Brillouin zone. Note that the nomenclature for the symmetry elements and high-symmetry k-points are taken from the Bilbao database of lattice symmetry and k-points.<sup>154</sup>

The density of states is the summation of the number of states in bands at each energy level and is typically most useful when broken down to elemental contributions, such as those shown in Figure 2.4.1b. It gives a chemical interpretation of band composition, allowing the physics and chemistry of the material to be simultaneously understood. If desired, the density of states can be further broken down into orbital specific contributions for each element (s-orbital, p-orbital, d-orbital, etc.). Such representations are essential to understanding the chemistry inherent in band structures. For example, the density of states plot in Figure 2.4.1 shows that the frontier orbitals (the highest energy filled orbital and the lowest energy unfilled orbital) are comprised primarily of Pb and I. This knowledge tells chemists that to significantly augment the band gap (the difference in energy between the frontier orbitals where no electronic states can exist) the bonding between Pb and I must change, or Pb or I must be substituted for an alternative element with appropriate charge. Together, the band structure and density of states provide a comprehensive picture of the chemistry and physics of materials.

From the band structure, effective masses can be recovered. The effective mass is a numerical quantification of how well charge carriers can move through a material. Effective masses are calculated using the dispersion relation, which is a measure of the

change in energy with respect to the coordinates of the reciprocal lattice:<sup>155,156</sup>

$$\frac{1}{m^*} = \frac{1}{\hbar^2} \frac{\partial^2 E}{\partial k^2} \quad (\text{II.4.1})$$

where  $m^*$  is the effective mass,  $\hbar$  is the reduced Planck's constant,  $E$  is the energy, and  $k$  is the coordinate in reciprocal space. Equation II.4.1 originates from Newton's 2<sup>nd</sup> law of motion.<sup>157</sup> Essentially, the effective mass is a measure of how much effort is required to move a charged particle through the material, the lower the effective mass, the easier it will be to move the particle. As previously stated, points in reciprocal space represent waves (and directions) in real space. As such, the presentation of the effective mass through the change in energy as a function of reciprocal coordinates gives an indication of how easily charged particles will move in real space directions. The directional dependence of charge carrier effective mass is readily apparent in anisotropic materials and materials that have directions with no bonding, such as 2D sheets, 1D tubes, or 0D suspended materials. When measured in a direction of delocalized orbitals, the effective mass would be expected to be rather small whereas when measured in the direction of a vacuum or broken/dangling bonds the effective mass would be expected to be rather large. These results give good indication of charge transport in materials, which is critical for applications such as energy storage in batteries, conductive wiring, and solar materials.

## II.4.2 Phonons

Vibrations in solids, termed phonons, travel through the material in a concerted fashion. Similar to molecular vibrations, the mathematical origin of phonons is rooted at the fundamental level in Hooke's law of springs; Atoms vibrate as if attached to a spring, oscillating in a harmonic motion about their equilibrium position. In solids, when atoms vibrate with concerted motion, waves traveling through the solid begin to appear. These waves have a frequency,  $\omega$ , and a direction specified by a point in reciprocal space,  $q$ . This  $q$ -point is the vibrational equivalent to  $k$ -points in electronic structure theory. The decoupling of the electronic and nuclear motion within Schrödinger's equation proposed by Born and Oppenheimer<sup>137</sup> sets the stage for recovery of vibrational properties.

Just like electronic properties, vibrational properties are calculated from an equilibrium structure. An equilibrium structure is obtained when the forces,  $F$ , acting

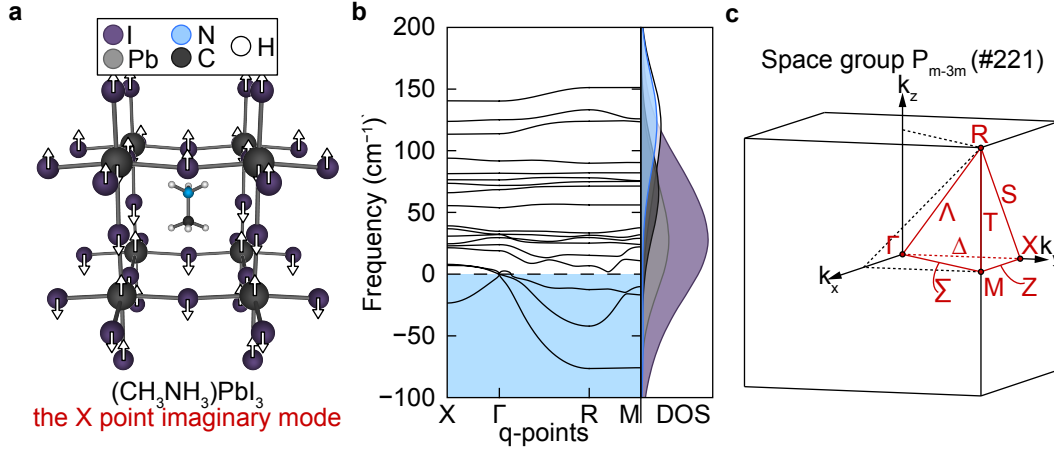


**Figure 2.4.2** a) Cubic  $(\text{CH}_3\text{NH}_3)\text{PbI}_3$ . b) Phonon band structure and phonon density of states of  $(\text{CH}_3\text{NH}_3)\text{PbI}_3$ . The negative phonon frequencies correspond to the phase transition of cubic  $(\text{CH}_3\text{NH}_3)\text{PbI}_3$  to phases more stable at lower temperatures. The negative phonon frequency at the  $X$  q-point is representative of the phase transition depicted in (a) by the arrows. c) Space group for cubic  $(\text{CH}_3\text{NH}_3)\text{PbI}_3$ . While technically  $(\text{CH}_3\text{NH}_3)\text{PbI}_3$  has the  $P1$  symmetry (space group # 1), its space group is approximated as its parent structures space group  $P_{m-3m}$  (# 221). Typically structures that will undergo phonon calculations are converged with a very strict k-grid, force convergence criteria, and total energy convergence criteria; Here, these criteria were loosened to provide a simple but representative example.

on individual nuclei vanish:<sup>158</sup>

$$F_I \equiv \frac{\partial E(R)}{\partial R_I} = 0 \quad (\text{II.4.2})$$

where  $R_I$  are the nuclear coordinates of the  $I^{\text{th}}$  atom. Vibrational frequencies are determined from the Hessian matrix of the coordinate dependent energy surface scaled by the nuclear mass:

$$\det \left| \frac{1}{\sqrt{M_I M_J}} \frac{\partial^2 E(R)}{\partial R_I \partial R_J} - \omega^2 \right| = 0 \quad (\text{II.4.3})$$

To obtain a functional form of the partial derivative, the Hellmann-Feynman theorem is invoked:<sup>159,160</sup>

$$\frac{\partial E_\lambda}{\partial \lambda} = \langle \Psi_\lambda | \frac{\partial H_\lambda}{\partial \lambda} | \Psi_\lambda \rangle \quad (\text{II.4.4})$$

which recovers the partial derivative of an expectation value,  $E$ , with respect to a parameter,  $\lambda$ , through the partial derivative of the Hamiltonian with respect to the same parameter. Using the Hellmann-Feynman theorem the force and change in energy with respect to nuclear coordinates can be directly determined from the system wavefunction:

$$F_I = -\frac{\partial E(R)}{\partial R_I} = -\langle \Psi(R) | \frac{\partial H(R)}{\partial R_I} | \Psi(R) \rangle \quad (\text{II.4.5})$$

For a ground state wavefunction,  $\Psi(r, R)$ , that depend on the ground state electron

density and electron-ion interaction, the Hellman-Feynman theorem returns:

$$F_I = - \int n_R(r) \frac{\partial V_R(r)}{\partial R_I} dr - \frac{\partial E_N(R)}{\partial R_I} \quad (\text{II.4.6})$$

where  $n_R(r)$  is the ground state electron density for a nuclear configuration,  $R$ , and  $V_R(r)$  is the electron-nuclei interaction:

$$V_R(r) = - \sum_{iI} \frac{Z_I e^2}{r_i - R_I} \quad (\text{II.4.7})$$

Here,  $e$  is the charge of an electron and  $Z_I$  is the charge of the nucleus. Equation II.4.6 forms the basis of the frozen phonons method,<sup>161–163</sup> sometimes called finite displacements. The problem is that Equation II.4.6 only gives the 1<sup>st</sup> order derivative while the Hessian matrix requires the 2<sup>nd</sup> order derivative. In practice, an atom in the equilibrium model is moved from its equilibrium position and the force on all the other atoms in response to this movement is then calculated. This gives a column of the Hessian matrix in Equation II.4.3. This is done in a step wise fashion where each atom is moved in the equilibrium structure and the force on all other atoms is then calculated to fill out all the columns of the Hessian matrix. This was the first and simplest method used to calculate phonon spectra, and excels at calculating phonon frequencies at the  $\Gamma$  point. In this regard, phonon frequencies at q-points other than  $\Gamma$  cannot be directly calculated. To calculate non- $\Gamma$  q-points the unit cell must be expanded to a supercell in a direction commiserate with the q-point of interest, and then the phonon frequencies must be extrapolated from the supercell using the unit cell. Ultimately, frozen phonons remain the simplest form of phonon calculations even when there is a need for supercell expansion as it requires no additional formulisms or complex mathematical algorithms beyond those already present within the DFT framework. As a result, frozen phonons, while not always the fastest, will often be the most reliable way to calculate phonons for tricky, difficult, or very large system.

To advance on the frozen phonon method, the derivative of Equation II.4.6 can be taken with respect to a second nuclear coordinate,  $R_J$ , to give form to the energy term of the Hessian matrix:

$$\frac{\partial^2 E(R)}{\partial R_I \partial R_J} \equiv - \frac{\partial F_I}{\partial R_J} = \int \frac{\partial n_R(r)}{\partial R_J} \frac{\partial V_R(r)}{\partial R_I} dr + \int n_R(r) \frac{\partial^2 V_R(r)}{\partial R_I \partial R_J} dr + \frac{\partial^2 E_N(R)}{\partial R_I \partial R_J} \quad (\text{II.4.8})$$

where  $E_N(R)$  is the electrostatic interaction between different nuclei:

$$E_N(R) = \frac{e^2}{2} \sum_{I \neq J} \frac{Z_I Z_J}{R_I - R_J} \quad (\text{II.4.9})$$

Equation II.4.8 shows that to calculate the Hessian matrix (sometimes called the matrix of interatomic force constants) in Equation II.4.3, the ground state electron density as well as its linear response to distortion of its geometry,  $\partial n_R(r)/\partial R_J$ , are required. This is the foundation for density functional perturbation theory (DFPT). In practice, atomic coordinates in Equation II.4.3 are labeled by a multi-unit cell index,  $I$ , which indicates a unit cell,  $l$ , in which atoms with atomic coordinates,  $s$ , are being investigated,  $I \equiv \{l, s\}$  and  $J \equiv \{m, t\}$ . Additionally, the change in energy is taken with respect to atomic displacements,  $u$ , instead of nuclear coordinates,  $R$ :

$$C_{st}^{\alpha\beta}(l, m) \equiv \frac{\partial^2 E}{\partial u_s^\alpha(l) \partial u_t^\beta(m)} \quad (\text{II.4.10})$$

where  $C$  is a matrix of interatomic force constants with Cartesian components  $\alpha$  and  $\beta$ . The Fourier transform of  $C_{st}^{\alpha\beta}(R)$  with respect to  $R$  can be taken, and now the displacements can be described in terms of wave vectors in reciprocal space,  $q$ :

$$\tilde{C}_{st}^{\alpha\beta}(q) \equiv \sum_R e^{-iq \cdot R} C_{st}^{\alpha\beta}(R) \quad (\text{II.4.11})$$

$\tilde{C}_{st}^{\alpha\beta}(q)$ , often denoted simply as  $D$ , is known as the dynamic matrix. Equation II.4.3 becomes the secular equation:

$$\det \left| \frac{1}{\sqrt{M_I M_J}} \tilde{C}_{st}^{\alpha\beta}(q) - \omega^2 \right| = 0 \quad (\text{II.4.12})$$

Equation II.4.12 is a powerful equation as interatomic force constants are more readily calculated in reciprocal space, and from Equation II.4.11 can readily be translated back to real space. Unlike the frozen phonon method, no extrapolation is required to find phonon frequencies at non- $\Gamma$  q-points. This means the unit cell can be used to recover the full phonon spectra. Additionally, as the linear response of the electron density is calculated, often times DFT programs also return dielectric information without any additional calculations. The problem with DFPT is its poor efficiency scaling; The effort required to calculate phonon frequencies is exponential with the number of atoms. For systems with  $> 100$  electrons, DFPT often becomes intractable. For small systems,

however, DFPT offers the fastest and more reliable method for calculating phonon frequencies.

A third method for calculating phonon frequencies uses molecular dynamics simulation to gather real time changes of atomic forces to construct the dynamic matrix. This is accomplished through the velocity auto-correlation function:<sup>164</sup>

$$\langle v(0) \cdot v(t) \rangle = \frac{1}{N} \sum_{i=1}^N v_i(0) \cdot v_i(t) \quad (\text{II.4.13})$$

where  $v(t)$  is the velocity at time  $t$  and  $N$  is the number of atoms. The Fourier transform of the velocity auto-correlation function provides a pathway to calculating the phonon density of states through:

$$f(\omega) = \frac{kT}{MD} \int_0^\infty \frac{\langle v(0) \cdot v(t) \rangle}{\langle v^2 \rangle} \cos \omega t dt \quad (\text{II.4.14})$$

where  $k$  is Boltzmann's constant,  $T$  is the temperature,  $D$  is the diffusion constant, and  $M$  is the mass. From the density of states the phonon frequencies at  $\Gamma$  can be computed. Unfortunately, only the frequencies at  $\Gamma$  can be determined. Unlike DFPT or frozen phonons, however, temperature is inherently included in this formalism, where it is absent in the others. DFPT and frozen phonon methods require additional effort to recover temperature effects. At the fundamental level, assuming the same approximations are made, all methods should produce the same vibrational frequencies. While additional correctional terms could be included, such as the non-analytical term correction, they are not utilized in this thesis and their discussion has been excluded for brevity.

Phonons, just like orbitals in electronic structure theory, form into bands that comprise a phonon band structure, depicted in Figure 2.4.2b. These bands represent the modes of the vibrating solid, and can be divided into normal modes and imaginary modes. Normal modes are comprised of three acoustic modes and  $n - 3$  optical modes. Acoustic modes approach zero at the  $\Gamma$  q-point, representing the translate of the unit cell in the three Cartesian directions, and have energies similar to sound waves. The remaining modes are the optical modes, which are vibrations often observed in spectroscopy. Imaginary modes are modes of negative frequency, brought about by the square of the imaginary number in the matrix of interatomic force constants (Equation II.4.10). While these modes are nonphysical, they represent instabilities present in the model. Negative frequencies at the  $\Gamma$  point mean the supplied model is not at a

minimum on the potential energy surface, and thus cannot exist as is. Negative frequencies at q-points other than  $\Gamma$  represent phase transitions. For example, in Figure 2.4.2 there is a lack of negative modes at  $\Gamma$ , showing the stability of  $(\text{CH}_3\text{NH}_3)\text{PbI}_3$  in its cubic phase, which has been observed at temperatures greater than 350 K. The negative frequencies at q-points other than  $\Gamma$  are likely phase transitions to the  $\alpha$  phase or the lower temperature tetragonal or orthorhombic phases. One such phase transition is depicted in Figure 2.4.2a, which maps to the  $X$  q-point. The evidence for phase transitions is furthered by the phonon density of states, which show that all imaginary modes are primarily made up of Pb and I character. In addition to stability and phase transition predictions, the phonon band structure can be used to calculate the phonon-electron coupling constants as well as provide a starting point for IR and raman spectra calculations. All these rely on determination of the phonon frequencies at the  $\Gamma$  point and are readily obtained from all methods described above, without the need to extrapolate q-points.

As the starting point for both the frozen phonon method as well as DFPT is an equilibrium structure described by Equation II.4.2. Residual forces still present in the model after optimization introduce errors into the dynamical matrix, and thus the phonon frequencies, proportional to the magnitude of the residual forces. As a result, it is often required that structures be optimized using convergence criteria orders of magnitude more strict than that for electronic structure calculations. The molecular dynamics method, on the other hand, relies on a statistic distribution of atomic forces to recover the average vibrations and thus does not require a converged structure. Calculation of phonon modes using DFPT methods is often made more difficult by the fact that not all softwares are readily equipped to utilize DFPT methods. Some software simply do not have the DFPT algorithms available, while other software that do, provide it in an all-or-nothing context, meaning the calculation cannot be restarted from a checkpoint. This makes calculation of phonons for large systems intractable using DFPT. Even in the frozen phonon method the poor scaling of model size alongside the requirement for the user to fully understand model symmetry makes the frozen phonon method not always a user friendly experience.

### II.4.3 Nonlinear Optics

In nonlinear optics, a nonlinear optical phenomena occurs when a material exhibits a response to an applied optical field that depends on the strength of the field in a nonlinear manner.<sup>165</sup> For example, the nonlinear polarization,  $P(t)$ , of a material over

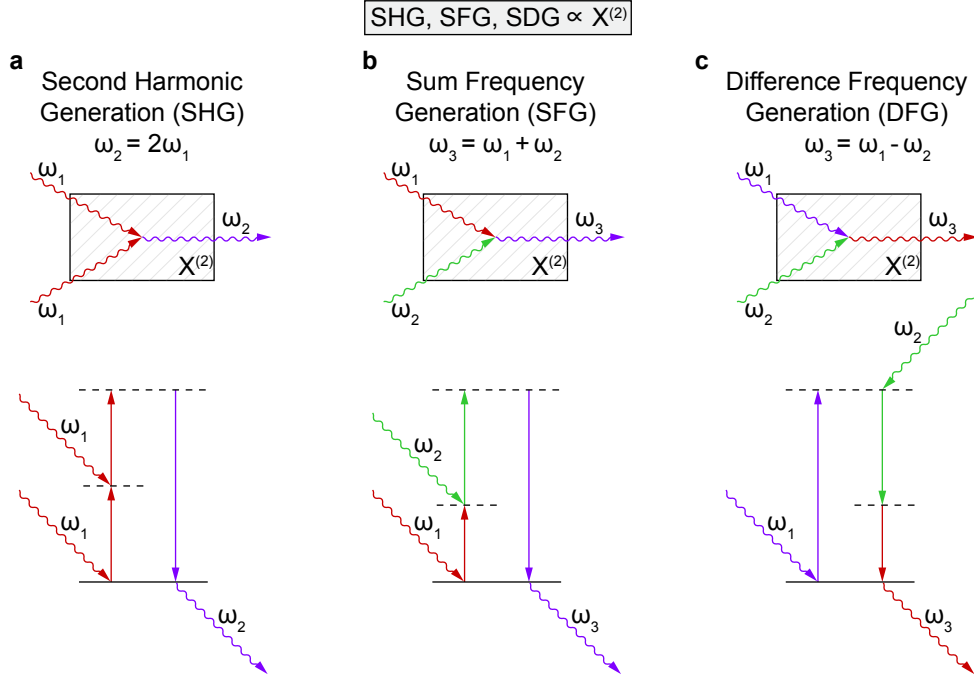


**Figure 2.4.3** a) Second harmonic generation where two photons of the same frequency combine to generate a new photon of double the original frequency. b) Sum frequency generation where two photons of different frequencies generate a new photon whose frequency is the sum of the original two photon frequencies. c) Difference frequency generation where two photons of different frequencies generate a new photon whose frequency is the difference of the original two photon frequencies.

time depends on the strength of an optical field,  $\epsilon(t)$ , which varies as a power series:

$$P(t) = \epsilon_0 \left[ \chi^{(1)} \epsilon(t) + \chi^{(2)} \epsilon^2(t) + \chi^{(3)} \epsilon^3(t) + \dots + \chi^{(n)} \epsilon^n(t) \right] \equiv P^{(1)}(t) + P^{(2)}(t) + P^{(3)}(t) + \dots + P^{(n)}(t) \quad (\text{II.4.15})$$

compared to the linear polarization, which varies linearly:

$$P(t) = \epsilon_0 \chi^{(1)} \epsilon(t) \quad (\text{II.4.16})$$

where  $\epsilon_0$  is the permittivity of free space,  $\chi^{(1)}$  is the linear susceptibility, and  $\chi^{(2)}$ ,  $\chi^{(3)}$ , and  $\chi^{(n)}$  are the second-, third-, and  $n^{\text{th}}$ -order non-linear optical susceptibilities, respectively. Equation II.4.15 assumes that the medium responds instantaneously to changes in the optical field and therefore only holds for a lossless and dispersionless medium. This also means that while generally the nonlinear susceptibility of a material is dependent on the frequency of the applied field, the susceptibilities can be treated as constants in this approximation.

Nonlinear optical phenomena has been utilized by the research community to diversify lasers through processes such as second-harmonic generation (SHG), sum-frequency generation (SFG), and difference-frequency generation (DFG), used to generate monochromatic light of visible, UV, and IR wavelengths, respectively, that are not normally accessible by the laser generating medium. To expand the range of wavelengths accessible to lasers, a myriad of materials that can produce SHG, SFG, and DFG effects are necessary. In these materials, the generation of monochromatic light of a new wavelength is proportional to  $\chi^{(2)}$ :

$$P^{(2)} = 2\epsilon_0\chi^{(2)}\epsilon^2 \quad (\text{II.4.17})$$

The optical field is split into various complex components, which has been excluded for brevity, based upon the number of unique frequencies present. These components are related to the frequency of the light source, and derivations can be made for a single source (SGH) or multiple sources (SFG and DFG), as depicted in Figure 2.4.3. It should be recognized, however, that Equation II.4.17 is proportional to  $\chi^{(2)}$ , which is medium dependent. As a result,  $\chi^{(2)}$  determines which materials will excel at producing SHG, SFG, and DFG effects.

To understand how a system changes in response to an applied optic field, we turn to perturbation theory. In perturbation theory the Hamiltonian becomes:

$$\hat{H} = \hat{H}_0 + \hat{V} \quad (\text{II.4.18})$$

where  $\hat{H}_0$  is the total energy of the free atom(also know as the unperturbed ground state) and  $\hat{V}$  is a quasi-static perturbation from an external field. For the problem at hand  $\hat{V}$  takes the form:

$$\hat{V} = -\hat{\mu}\epsilon \quad (\text{II.4.19})$$

where  $\hat{\mu}$  is the electric dipole moment operator and  $\epsilon$  is the applied quasi-static field. Equation II.4.18 can be inserted into Equation II.1.2 and the resulting system energy can be expanded in a Taylor expansion in some generalized perturbation,  $X$ :<sup>166</sup>

$$E(X) = E(0) + \left. \frac{\partial E}{\partial X} \right|_{X=0} \cdot X + \frac{1}{2!} \left. \frac{\partial^2 E}{\partial X^2} \right|_{X=0} \cdot X^2 + \frac{1}{3!} \left. \frac{\partial^3 E}{\partial X^3} \right|_{X=0} \cdot X^3 + \frac{1}{4!} \left. \frac{\partial^4 E}{\partial X^4} \right|_{X=0} \cdot X^4 + \dots \quad (\text{II.4.20})$$

The calculation of the electronic susceptibility of a medium requires an understanding

of the energy stored,  $W$ , by the polarized medium:

$$W = - \int_0^\varepsilon P(\varepsilon) d\varepsilon = -\frac{1}{2}\chi^{(1)}\varepsilon^2 - \frac{1}{3}\chi^{(2)}\varepsilon^3 - \frac{1}{4}\chi^{(3)}\varepsilon^4 - \dots \equiv W^{(2)} + W^{(3)} + W^{(4)} + \dots \quad (\text{II.4.21})$$

Comparison of Equation II.4.20 and II.4.21 when  $X = \varepsilon$  reveals that :

$$\begin{aligned} \chi^{(1)} &= -\frac{\partial^2 E}{\partial \varepsilon^2} \\ \chi^{(2)} &= -2\frac{\partial^3 E}{\partial \varepsilon^3} \\ \chi^{(3)} &= -6\frac{\partial^4 E}{\partial \varepsilon^4} \end{aligned} \quad (\text{II.4.22})$$

In practice  $\varepsilon$  gets split into the Cartesian directions of the electric field, and the nonlinear susceptibilities are normalized by the unit cell volume,  $V$ :

$$\chi_{ijk}^{(2)} = -\frac{2\pi}{V} \frac{\partial^3 E}{\partial \vec{\varepsilon}_i \partial \vec{\varepsilon}_j \partial \vec{\varepsilon}_k} \quad (\text{II.4.23})$$

typically expressed as:

$$\beta_{ijk} = -\frac{\partial^3 E}{\partial \vec{\varepsilon}_i \partial \vec{\varepsilon}_j \partial \vec{\varepsilon}_k} \quad (\text{II.4.24})$$

where  $\beta_{ijk}$  is the first hyperpolarizability. The recovery of the first hyperpolarizability is accomplished using the coupled perturbed Kohn-Sham theory<sup>167,168</sup> in software packages such as CRYSTAL17.<sup>169,170</sup> Here, starting from a converged ground state density, the perturbation matrices are calculated to be used as an input in a self consistent couple perturbed Kohn-Sham cycle. The perturbation matrices aids in the recovery of the variation in the crystal orbital coefficients, which are then used to calculate the perturbed density matrix. The derivative of the perturbed density matrix is taken with respect to the electric field components, which in essence yields Equation II.4.24. As the recovery of the susceptibility constants initially relies on the ground state density and geometry, tight convergence criteria are required to minimize error. In a fashion similar to that of phonon calculations, the convergence criteria are often orders of magnitude more stringent than basic electronic structure calculations.

CHAPTER III  
CYCLOPROPENIUM (C<sub>3</sub>H<sub>3</sub>)<sup>+</sup> AS AN AROMATIC ALTERNATIVE A-SITE CATION FOR  
HYBRID HALIDE PEROVSKITE ARCHITECTURES

*The contents of this chapter have been or are intended to be published in whole or in part.  
The text presented here has been modified from the publication below:*

Kasel, T. W., Murray, A. T., and Hendon, C. H., *J. Phys. Chem. C*, 2018, **122**, 2041.

### **III.1 Bridge & Introduction**

By design, materials studied by the research community are far from perfect. Next generation materials are often riddled with shortcomings and deficiencies. For example, perovskites, discussed thoroughly throughout this thesis, as previously mentioned are unstable and degrade in light/air, heat, and moisture.<sup>92-100</sup> As a result, it is often desirable to augment individual physical or electronic aspects of a material to make their properties more tenable to their desired applications. With the exception of using heterovalent oxidation states, electrical augmentation comes through physicochemical changes. Therefore, conclusions on electronic augmentation cannot readily be made in the absence of a discussion of the corresponding physical change. Such physical changes can have subtle or substantial impacts on the electronic properties of a material. The preferability of electronic augmented is highly dependent upon the inherent properties of the parent materials (band gap, effective mass, electron affinity, ionization potential, etc.). Aiming to change a given electronic property through physical changes, or make physical changes while avoiding electronic changes are both equally valid and desirable outcomes. The presentation and form of the electronic augmentation then falls on the motivation to address a physical or electrical limitation, for example: the moisture instability of organic-inorganic hybrid perovskites.

While there are many different avenues to address the moisture instability of organic-inorganic hybrid perovskite devices, one of the most straightforward is to



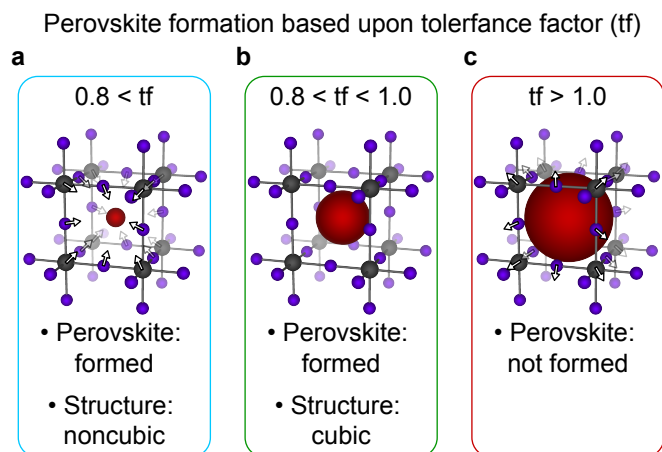


**Figure 3.1.2** Guide to perovskite formation when tolerance factors are a)  $< 0.8$ , b)  $0.8 \leq tf \leq 1.0$ , or c)  $> 1.0$ . Arrows show the general forces felt by the nearest neighbor atoms for when the A-site cation is of incompatible size.

halide counterparts. To form a perovskite in the cubic phase, the tolerance factor must fall between 0.8 and 1.0, indicating a perfect to a near perfect fit of the A-site cation in the cage formed by the surrounding  $BX_3$  octahedron (at the lower end of the range slight octahedral tilting and distortion is often observed). A tolerance factor  $> 1$ , suggests that a perovskite structure will not form at all, while a tolerance factor  $< 0.8$  suggests that a noncubic perovskite structure will likely form, depicted in Figure 3.1.2.

These rules are not hard set, on the contrary, the value of the tolerance factor highly depends upon the radii of the ion chosen, which can vary widely depending upon how the electron cloud is defined. Typically, the Shannon radii is used,<sup>173,174</sup> however, it has been suggested that the Shannon radii alone is insufficient to produce accurate tolerance factors as the radii of the B-site divalent metal can depend upon the identity of the halide with which it is paired.<sup>175</sup> In this regard, the size of the octahedron is therefore improperly calculated. As such, it is of great import to accurately know the size of the B-site divalent metal as it depends on its halide partner. Still, tolerance factors for the various combinations of charge appropriate elements has led to unique perovskite structures and has been rather successful. The tables in the appendix contain the tolerance factors calculated using the Shannon radii for various combinations of fully inorganic and common organic-inorganic hybrids (including cyclopropenium as suggested by our work). The tolerance factor is readily tunable based upon the components used, as seen by both the Tables in the appendix as well as Figure 3.1.3. Herein, again seen by Figure 3.1.1, lies a problem: the inherently limited

elements using the equation:<sup>172</sup>

$$tf = \frac{r_A + r_X}{\sqrt{2}(r_B + r_X)} \quad (\text{III.1.1})$$

where  $r_A$  is the radius of the A-site cation,  $r_B$  is the radius of the B-site divalent metal, and  $r_X$  is the radius of the halide. Originally, Goldersmith defined tolerance factors for predicting the structural phase when forming oxide based perovskites. This idea, however, is readily extendable to its

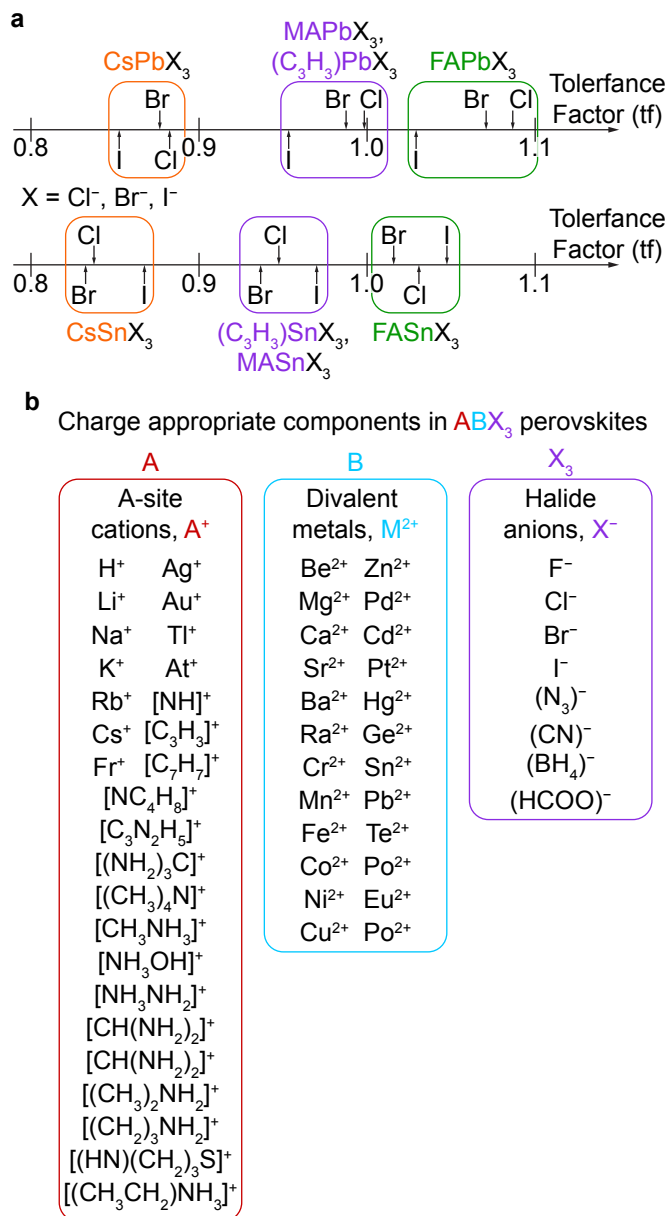


**Figure 3.1.3** a) Tolerance factors for commonly studied perovskites structures, including one suggested by our work ( $C_3H_3^+$ ) for both Pb and Sn based halide perovskites. b) Limited lists of various charge appropriate components.

number of unique inorganic perovskites that can form in the cubic phase. Thus there is motivation to find charge and size appropriate organic moieties to tune physical and electrical properties of perovskites beyond this limited list of inorganic elements.

Generally, the key advantages of using organic moieties in materials chemistry is the ability to electronically and sterically tune the compound of interest in a rational and controlled manner. When it comes to addressing the moisture instability of common protic A-site cations, the task thus becomes selecting an organic cation that is aprotic and of appropriate charge and size, all while augmenting the electronic properties of the parent material in a controlled, predictable, and desirable manner. As the champion

material ( $(CH_3NH_3)PbI_3$ , more specifically the  $PbI_3^-$  octahedron) already exhibits ideal characteristics for photovoltaic applications, perturbation of electronic properties, when possible, should be avoided. This is precisely the goal of the following publication: offer an alternative aprotic cation to methylammonium that does not significantly perturb the electronic properties of the parent material. However, this is also the origin of difficulty; How the electronic properties of the host are perturbed as the A-site cation is augmented into a novel form is not a readily apparent relation.

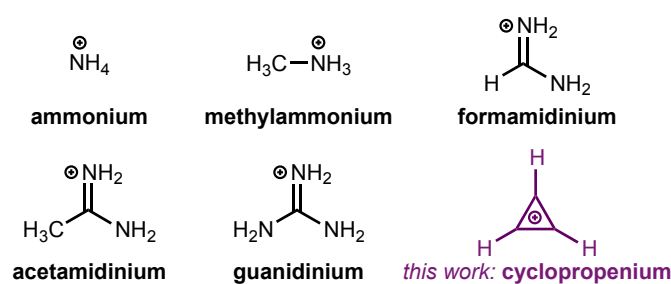


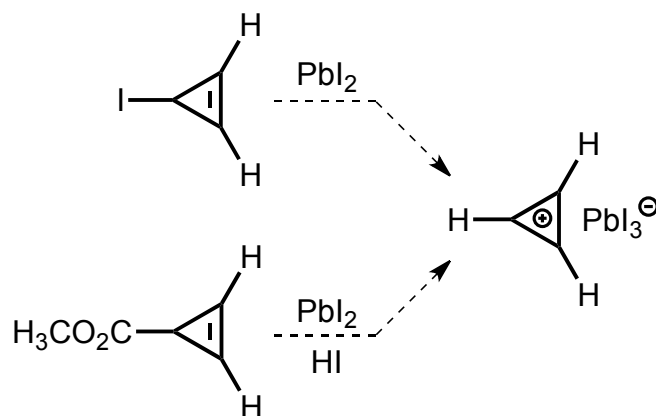
**Figure 3.1.4** Some of the reported organic A-site cations found in  $\text{PbI}_3^-$  based perovskites. The cyclopropenium cation differs from the other cations as it is aprotic.

Unlike the all-inorganic cesium analog,<sup>41–43</sup>  $\text{CsPbI}_3$ , the presence of a molecular dipole in methylammonium gives rise to a suite of unusual physical properties including ferroelectricity<sup>100,104,176,177</sup> and the occurrence of several crystallographically dissimilar

phases.<sup>178,179</sup> While the physical properties of the material are clearly dependent on the nature of the monovalent cation, the electronic structure is less obviously so. In essentially all reported hybrid halide structures composed of Pb and I the frontier electronic bands have I-p and Pb-s,p character,<sup>54</sup> as well as similar band gaps to one another.<sup>180</sup> Ammonium,<sup>45</sup> formamidinium,<sup>53</sup> acetamidinium,<sup>46</sup> and guanidinium<sup>47</sup> (depicted in Figure 3.1.4) have been incorporated as alternative cations into similar systems, all of which share comparable electronic structure and physical properties to their methylammonium analogue. Unfortunately, beyond those already mentioned, the chemical diversity of the A-site organic cation has been rather limited, generally the result of steric constraints of the  $\text{PbI}_3^-$  cage. While the compositional landscape is fairly limited for both the B and X-site ions,<sup>62,181</sup> (as determined by the redox potential of elements on the periodic table, again see Figure 3.1.1) the lack of diversity at the A-site is remarkable.

The organic A-site cations depicted in Figure 3.1.4 share two things in common: they are small enough to fit inside the  $\text{PbI}_3^-$  cage and they are singly charged. In the former, the size limitation is neatly summarized by comparison of the radius tolerance factors as described previously.<sup>172,175</sup> In the latter, there are only a limited number of ways to bestow a permanent positive charge on an organic (i.e. H, C, N, O-based) material; the most trivial being through protonation of a Lewis base lone pair. However, while acid/base chemistry is conceptually simple and allows rapid synthesis from common iodide salts the use of protic cations is detrimental for crystal stability (i.e. elimination of HI is thermodynamically favorable<sup>98</sup> and cation deprotonation or molecular disproportionation leads to gas formation and entropically motivated decomposition).<sup>94,97</sup> Therefore, the discovery of a novel organic cation that is both stable and small may mitigate some difficulties currently faced by  $(\text{CH}_3\text{NH}_3)\text{PbI}_3$  and

other protic hybrid halide perovskite architectures.



**Scheme III.1** Possible synthetic routes to  $(C_3H_3)PbI_3$ .\*

Here we describe an aprotic, all-hydrocarbon hybrid intercalator by drawing on non-benzenoid arene chemistry.<sup>182</sup> The  $C_3H_3^+$  cation possesses Hückel aromaticity and has been isolated in both the hydrogenic and halogenated forms.<sup>183–187</sup> The parent  $C_3H_3^+$  ion can be synthesized by Lewis acid-mediated chloride elimination from  $C_3H_3Cl$ ,<sup>188</sup> or elimination of carbon monoxide and methanol by the action of Brønsted acid on cyclopropenyl ester  $C_3H_3CO_2CH_3$ .<sup>183</sup> While these carbocations are remarkably stable in solution phase, the stability should not grossly differ as their stability depends on their surrounding dielectric medium. Although we did not attempt a synthesis here, we do offer two plausible synthetic routes, Scheme III.1, that involve either the treatment of iodocyclopropene,  $C_3H_3I$ <sup>188,189</sup> with  $PbI_2$ , or the decarbonylation of  $C_3H_3CO_2CH_3$  with hydrogen iodide<sup>183</sup> in the presence  $PbI_2$ .

Despite its aromatic nature  $C_3H_3^+$  has not been widely employed in functional materials, however, substituted derivatives have been used extensively for catalysis<sup>190–192</sup> and also as electrolyte components.<sup>193</sup> In the following work we use DFT calculations to demonstrate the electronic properties of the hypothetical target material  $(C_3H_3)PbI_3$  with aims of motivating research into the application of  $C_3H_3^+$  in hybrid halide perovskite architectures.

### III.2 Results and Discussion

First we assessed the feasibility of  $C_3H_3^+$  by examination of the revised tolerance factor.<sup>175</sup> Given  $C_3H_3^+$  is of comparable size to formamidinium, we estimate the tolerance factor to be 0.96, suggesting that its incorporation into the  $PbI_3^-$  lattice is

\*The Lewis acid-mediated iodide elimination is adapted from Ref. 188, while the decarbonylation is adapted from Ref. 183.

feasible. We constructed  $(\text{C}_3\text{H}_3)\text{PbI}_3$  by making an A-site substitution to the low temperature orthorhombic phase of  $(\text{CH}_3\text{NH}_3)\text{PbI}_3$ . Subsequent geometric and electronic optimization was performed using the procedure detailed in the Experimental Method. The resultant structure was found to be orthorhombic (lattice vectors;  $a = 6.305$ ,  $b = 6.201$ ,  $c = 6.374 \text{ \AA}$ ).

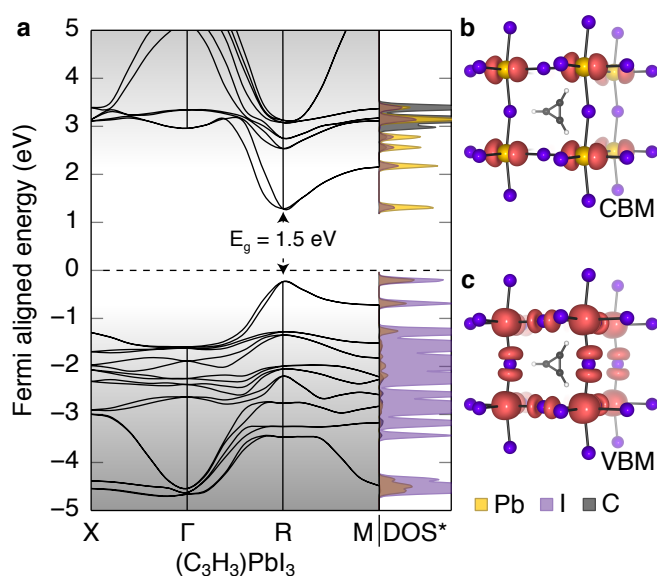


**Figure 3.2.1** (a) The electronic band structure and density of states of  $(\text{C}_3\text{H}_3)\text{PbI}_3$  as computed with HSE06sol+SOC (PBEsol with 43% HF exchange and spin-orbit coupling). (b,c) The conduction band minimum and valence band maximum orbital contributions at the R-point. Electron density isosurface is plotted in salmon at  $0.006 \text{ e/\AA}^3$ . Density of states are plotted for special k-points, only\*.

primarily Pb-p states (as evidenced by Figure 3.2.1b and the density of states). The VBM remains I-p and Pb-s centered, largely the same as  $(\text{CH}_3\text{NH}_3)\text{PbI}_3$  (Figure 3.2.1c). Furthermore, while the band gap is highly dependent on the computational approach, the inclusion of  $\text{C}_3\text{H}_3^+$  does not significantly alter the band gap compared to its methylammonium analogue, with  $(\text{C}_3\text{H}_3)\text{PbI}_3$  featuring an electronic gap ( $E_g$ ) = 1.5 eV (from HSE06sol+SOC with 43% HF exchange). PBEsol was also tested and produced  $E_g = 1.3 \text{ eV}$ .

Considering the desirable electronic properties of  $(\text{C}_3\text{H}_3)\text{PbI}_3$  we next assess the dynamic stability of the orthorhombic phase.

The role of hydrogen bonding in the methylammonium hybrid halide perovskite materials is still under investigation.<sup>194–196</sup> Given the nature of the N–H bond,

The electronic band structure of  $(\text{C}_3\text{H}_3)\text{PbI}_3$  shows the persistent characteristic features of most lead iodide-based perovskites (Figure 3.2.1a). Notably, the incorporation of  $\text{C}_3\text{H}_3^+$  retains a direct electronic transition at the R-point and reasonable curvature at the valence band maximum (VBM) and conduction band minimum (CBM). Effective masses of holes and electrons were found to be  $m_h^* = -1.27$  and  $m_e^* = 0.77$ , respectively. Like other hybrid halide perovskites, the conduction band is composed of

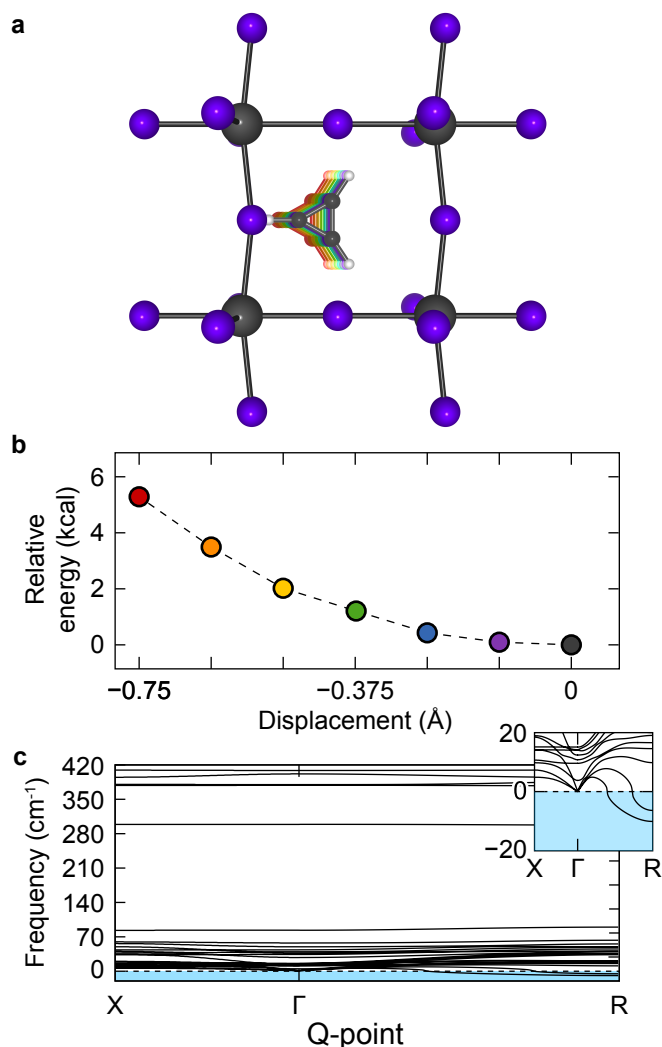


**Figure 3.2.2** (a) Seven displacements of the A-site cation. The trajectory was obtained from an *ab initio* molecular dynamic simulation triplicate. (b) Corresponding energies of displacement suggest that C<sub>3</sub>H<sub>3</sub><sup>+</sup> ions are at least translation mobile at room temperature. (c) Examination of the phonon band structure shows no negative modes at  $\Gamma$ , and the usual negative modes - emphasized in the inset of panel c - associated with PbI<sub>3</sub><sup>-</sup> cage deformation when sampling in the R-vector, similar to that observed in (CH<sub>3</sub>NH<sub>3</sub>)PbI<sub>3</sub>.

hydrogen bonding will almost certainly affect the dynamics of any protic A-site cation, whose acidic proton is attracted to the bridging iodides. It should be noted, however, that intermolecular H-bonds could be beneficial in the formation of (CH<sub>3</sub>NH<sub>3</sub>)PbI<sub>3</sub>, but would also give rise to strong acid-base interactions with water. While C<sub>3</sub>H<sub>3</sub><sup>+</sup> would not be assumed to be a strong hydrogen bond donor, we nevertheless explored this possibility. We note that the geometrically optimized structure produced from our DFT calculations yields two distinct C-C bond lengths in the C<sub>3</sub>H<sub>3</sub><sup>+</sup> ring, (1.365 and two 1.734 Å). The bond length anisotropy is due to polarization installed by the PbI<sub>3</sub><sup>-</sup> cage deformation and the static nature of the DFT calculation. Using *ab initio* molecular dynamics simulations we are able to sample the A-site cation mobility (and therefore the A-site - cage interaction energy). We observe that C<sub>3</sub>H<sub>3</sub><sup>+</sup> can translate along the plane in which it points, one such trajectory is presented in Figure 3.2.2a. This motion occurs along a shallow potential energy surface (Figure 3.2.2b) suggesting that the A-site cation is mobile. As expected, we did not observe orientation of the A-site C-H proton towards a bridging I<sup>-</sup>, as the cyclopropenium is a poor hydrogen bond donor.

hydrogen bonding will almost certainly affect the dynamics of any protic A-site cation, whose acidic proton is attracted to the bridging iodides. It should be noted, however, that intermolecular H-bonds could be beneficial in the formation of (CH<sub>3</sub>NH<sub>3</sub>)PbI<sub>3</sub>, but would also give rise to strong acid-base interactions with water. While C<sub>3</sub>H<sub>3</sub><sup>+</sup> would not be assumed to be a strong hydrogen bond donor, we nevertheless explored this possibility.

We note that the geometrically optimized structure produced from our DFT calculations yields two distinct C-C bond lengths in the C<sub>3</sub>H<sub>3</sub><sup>+</sup> ring, (1.365 and two 1.734 Å). The bond length anisotropy is due to polarization installed by the PbI<sub>3</sub><sup>-</sup> cage deformation and the static nature of the DFT calculation. Using *ab initio* molecular dynamics simulations we are able to sample the A-site

We compute the phonon band structure to assess the structural stability of our orthorhombic structure (Figure 3.2.2c). We note that there are no negative modes at the  $\Gamma$ -point and, like  $(\text{CH}_3\text{NH}_3)\text{PbI}_3$ , we see negative acoustic modes when sampling  $\Gamma$ -to-R, associated with  $\text{PbI}_3^-$  cage deformation/structural transitions. Hence, we suspect that  $(\text{C}_3\text{H}_3)\text{PbI}_3$  is, at minimum, metastable and likely exists in a similar chemical space to its other hybrid cousins.

Indeed, the orthorhombic phase is only one of several possible structural phases that  $(\text{C}_3\text{H}_3)\text{PbI}_3$  may crystallize in. Short of an exhaustive structure search, we elected to include a second plausible hypothetical phase. Beginning with the  $\alpha$ -phase<sup>197</sup> observed for  $(\text{CH}(\text{NH}_2)_2)\text{PbI}_3^-$  cation substitutions were made and the structure was fully optimized; the resultant structure was triclinic (see Supporting Information for the optimized structure of both phases). The significant increase in unit cell size prevents a full analysis of the phonon band structure but we were able to assess dynamic stability through the omission of negative phonon modes at the  $\Gamma$ -point only. The electronic band gap was computed to be comparable to the orthorhombic phase, and the  $\alpha$ -phase predicted to lie on a relatively shallow potential energy surface, and is predicted to be more stable by 5 kcal/mol. The  $\alpha$ -phase is further dissimilar to the orthorhombic phase as the  $\text{C}_3\text{H}_3^+$  ions are aligned in a diagonal fashion, rather than coplanar to a lattice plane (this is best visualized by examination of the optimized structures, presented in the Supporting Information).

### III.3 Conclusions

In summary, the use of  $\text{C}_3\text{H}_3^+$  in  $\text{PbI}_3^-$  halide perovskite-type architectures provides interesting avenues and potential improvements in three key areas that trouble other hybrid alternatives. 1) The water instability of protic A-site cations may be remediated by the use of an aprotic cation such as the aromatic cation described in this paper. 2)  $\text{C}_3\text{H}_3^+$  possesses no permanent dipole, thus obviating charging effects and other anomalous behavior observed in the literature. 3) The similar band gap compared to existing hybrid technologies should lead to comparable performance of the chromophore. Finally, we must comment on the reactivity and stability of  $\text{C}_3\text{H}_3^+$ . Indeed, there are new challenges associated with the cyclopropenium cation and our current synthetic approach will likely have to be altered to realize this material. Furthermore, the more easily handled covalently halogenated cyclopropeniums are not feasible A-site cations in the 3D connected perovskites, due to the size requirements imposed by the  $\text{PbI}_3^-$  cage, but may offer interesting targets for 2D and layered

architectures.

### III.4 Computational Methods

Beginning with the experimentally determined crystal structure of the orthorhombic methylammonium lead iodide the A-site cation was substituted for  $C_3H_3$ . The material remained charge neutral as the cyclopropenium carries a single positive charge in this framework. The structure was then geometrically and electronically optimized with the DFT construct as implemented in VASP. A 500 eV planewave cutoff, PBEsol, and a 6 x 6 x 6 k-grid was used to ensure electronic convergence to within 0.001 eV per atom, and the resultant structure was found to be orthorhombic. A similar procedure was employed for the modification of  $\alpha$ -(CH(NH<sub>2</sub>)<sub>2</sub>)PbI<sub>3</sub>. A 4 x 4 x 2 k-grid was used and full optimization was performed. The resultant structure was triclinic. Tolerance factors were computed using  $r_{Pb} = 1.03$ ,  $r_I = 2.20$ , and  $r_{C_3H_3} = 2.16 \text{ \AA}$ , yielding a tolerance factor of 0.96.

Typically both Pb and I require spin-orbit coupling for accurate electron energies. However, the systematic underestimation of electronic band gap produced by PBEsol has been shown to recover the correct electronic band gap for these materials.<sup>198</sup> Here we use PBEsol as a first approximation, and compute the electronic band gap to be 1.3 eV. To recover a better electronic description of (PbI<sub>3</sub><sup>-</sup>) materials we employed the HSE06sol functional with an increased mixing of exact HF exchange (43%) and spin-orbit coupling. A similar procedure has been previously fruitful in predicting electronic properties of this class of materials.<sup>62,199</sup> In the text we refer to this method as HSE06sol+SOC and yielded  $E_g = 1.5 \text{ eV}$ . The electronic band structure is the computed using the geometric output from the PBEsol optimization with the HSE06sol+SOC used to sampling along the k-vectors (Figure 3.2.1). With exception to (NH<sub>4</sub>)PbI<sub>3</sub>, all hybrid halide perovskites are *P1*. Hence, we approximate the high symmetry point vectors and nomenclature using those assigned formally to the CsPbI<sub>3</sub> material, space group *Pm-3m*.

Effective masses were computed using the Effective Mass Calculator as presented by Fonari and Sutton,<sup>200</sup> accessed 09/09/2017. K-point sampling was made using a step size of 0.01 Bohr<sup>-1</sup>. The phonon band structure was computed using PhonoPy<sup>201</sup> by construction of a 2 x 2 x 2 supercell. Finite displacements were then used to compute the forces, using a tightened convergence criterion (0.0005 eV per atom).

*Ab initio* molecular dynamics was employed to investigate the dynamic stability of the  $C_3H_3^+$  cation. A relaxed cutoff of 400 eV and  $\Gamma$ -only k-grid sampling was used.

Simulations were run in triplicate to ensure no anomalous results, with a timestep of 0.5 fs heating at 0.1 K per geometric step from 0 – 500 K.

CHAPTER IV  
ELECTRONIC IMPLICATIONS OF ORGANIC NITROGEN LONE PAIRS IN LEAD IODIDE  
PEROVSKITES

*The contents of this chapter have been or are intended to be published in whole or in part.  
The text presented here has been modified from the publication below:*

T. W. Kasel and C. H. Hendon, *J. Mater. Chem. C*, 2018, **6**, 4765

#### **IV.1 Bridge & Introduction**

As seen from the previous work, chemical substitutions can be made to yield dissimilar physical properties to the parent material, while leaving the electronic properties relatively unaugmented. There are, however, other ways to achieve similar results without the need to change the base structure. Chemical additions at grain boundaries and interstitial locations can be used to tune both the physical and electrical properties of the host material. These additions could offer an alternative route to boosting the moisture resistance (decomposition shown in Figure 4.1.1a) of organic-inorganic hybrid perovskites without making chemical substitutions to the base composition of the parent material.

Surface passivation – both crystallographic<sup>106</sup> and at grain boundaries<sup>108,202</sup> – with hydrophobic organic molecules have shown some early success at boosting moisture resistance<sup>119</sup> (a (100) passivation is shown schematically in Figure 4.1.1b). The same passivation can also be extended to device surfaces and boundaries with other materials/air, encapsulating the perovskite material. Surface and grain boundary passivation has been achieved using both inorganic<sup>203</sup> and organic motifs, called passivating (or capping) agents.<sup>106</sup> Examples of inorganic motifs using elements native to PbI<sub>3</sub> based perovskites include lead oxysalts<sup>204</sup> and lead iodide<sup>205</sup> (lead iodide surface passivation is discussed in our later work).<sup>\*</sup> Organic motifs are typically small organic molecules<sup>118,119</sup> and polymers.<sup>108</sup> These organic motifs are commonly

---

<sup>\*</sup>Publication in review.

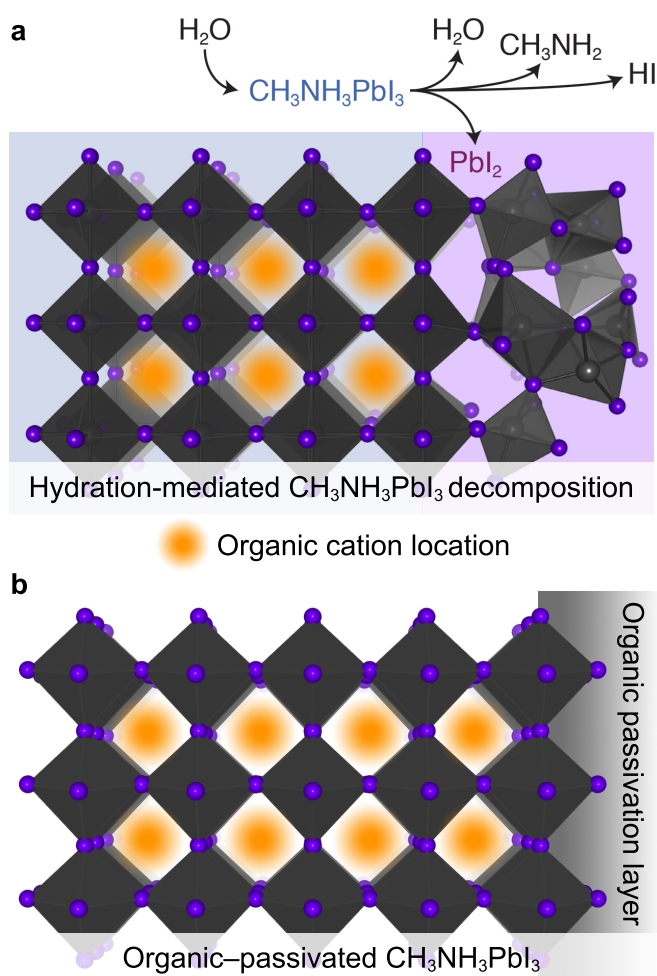


**Figure 4.1.1** a) The organic motif in protic organohalide perovskites (orange) reacts with water to form methylamine,  $\text{CH}_3\text{NH}_2$  evaporates at low temperatures, forming  $\text{PbI}_2$  and residual  $\text{HI}$ . b) The addition of a hydrophobic passivation agent at either external device faces or at grain boundaries is thought to improve moisture stability. They also act as a physical barrier to imminent water. Lead and iodine are shown in grey and orange respectively.

integrated into 2D perovskite architectures. One can envisage 2D perovskites by simply making a slice through a plane of iodides in a 3D lattice and pulling the respective slices apart. The real power of 2D perovskites is their ability to incorporate organic molecules and polymers that are too large to fit inside the caged A-site.<sup>206</sup>

One only needs to increase the distance between two blocks of 2D perovskite to incorporate larger organic motifs, offering tunability in organic molecular makeup. These organic motifs are often nitrogen containing<sup>118</sup> or nitrogen terminated,<sup>119,206</sup> giving them a chemical composition reminiscent of popular A-site organic cations. This is an exceptionally important implication, as under the right conditions, the A-site cations

should behave in a manner similar to these organic motifs, for better or worse.

Passivating agents incorporated at grain boundaries have been shown to increase device stability, prolonging device lifetimes<sup>207</sup> presumably slowing water penetration into the material. While passivating agents are typically composed of polymers containing tertiary amines (formed through ammonia condensation polymerization), as well as other non-polar polymers, the shortcoming of this approach is that the passivating agents potentially decrease device efficiency as the organic polymers are not typically electrically conductive.

In this vein, similarly motivated at increasing moisture resistance, we focused on understanding the electronic effects of these generally nonconductive organic polymers when implemented at perovskite surfaces and grain boundaries. The goal is to generate a detailed understanding of how the inclusion of passivating agents augment the electronic properties of the host material. The difficulty is, that unlike making component substitutions in the parent material, it is less clear how the addition of a nonnative chemical component will augment the electronic structure as it is unknown exactly how the nonnative addition will electronically and chemically mix with the host. It is even further complicated by the fact that surfaces of polar solids are difficult to model, made yet more difficult with additional surface atoms. The trick then is to find regions and motifs of the organic passivating agents that mix with the frontier electronic states of the host in a predictable and thus controllable manner, or not at all. If problematic regions are identified, they can be chemically tuned to dampen or remove negative electronic effects. The ideal effects of the passivating agents are identical to that of cyclopropenium in the previous work: to boost the moisture stability of the parent material to avoid decomposition without perturbing the electronic properties.

## IV.2 Results and Discussion

Our initial motivation was to examine the electronic implications of direct A-site substitution for a polymeric organic cation, which we conjecture would serve to mitigate water instability. Polymeric cations could potentially overcome entropic decomposition of  $\text{CH}_3\text{NH}_3\text{PbI}_3$  through a hydration-mediated deprotonation and subsequent release of  $\text{CH}_3\text{NH}_2$ . We elected to use polymers containing alkaline heteroatoms which could be protonated to form a charge neutral solid, as they were most reminiscent of methylammonium itself (*e.g.* aliphatically linked tertiary amines) one example shown in Figure 4.2.2f. After careful construction and optimization of several representative aliphatic cationic-polymer- $\text{PbI}_3$  models the resultant materials were determined to be unstable. The aliphatic  $-\text{CH}_2-\text{CH}_2-$  is too large to fit through the face of the perovskite resulting in significant Peirels distortion of the  $\text{PbI}_6$  octahedron. Although this outcome was unsurprising as syntheses involving large organic cations typically yield a 2D perovskite structure type.

During that initial investigation we noted one subtle utility of the 2D perovskite structure-type: they are reasonable models for the most extreme 3D perovskites grain boundary (a monolayer of anionic lead iodide). This similarity arises because the 2D

$\text{PbI}_4^{2-}$  and the (100) surface of the 3D  $\text{PbI}_3^-$  have analogous dangling iodides, Figure 4.2.1a, thus allowing us to model a surface without having to cleave a dipole neutral surface of the parent 3D semiconductor<sup>208,209</sup>. The validity of this surface approximation is predicated on the fact that dangling monolayer 2D iodides are less stable (*i.e.* higher energy) than their 3D counterparts due to the increase charge density of the  $\text{PbI}_4^{2-}$  sheet. Of course, other 2D  $\text{PbI}_n$  materials have been reported<sup>210</sup>, and could also be used in a similar fashion to analyze the electronic influences of the organic passivating agents on the electronic properties at grain boundaries of 3D materials.

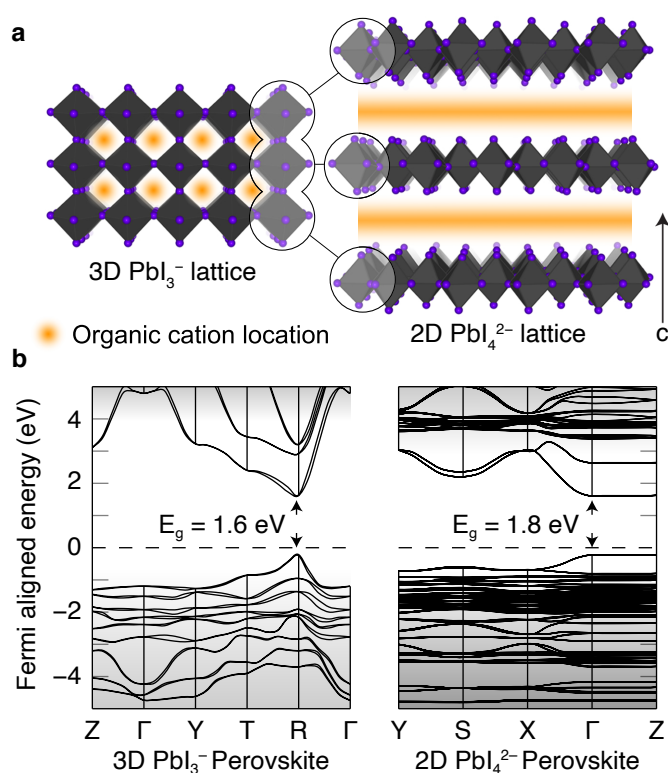


**Figure 4.2.1** a) The 3D perovskite  $\text{PbI}_3^-$  cage features similar inorganic connectivity to the 2D  $\text{PbI}_4^{2-}$  counterpart. The 2D dangling iodides are analogous to the (100), (010), and (001) surfaces of the 3D material. b) The electronic band structure of the 3D material features large band curvature in the conduction band, associated with delocalized Pb  $p$ -states. The valence band has less dispersion, and is comprised of a combination of Pb  $s$ - and I  $p$ -states. The reduction in Pb-I dimensionality in the 2D perovskite results in reduced curvature in both band extrema. Special points map to  $Pm-3m$  and  $Pbca$  space groups for the 3D and 2D structures, respectively.

The confinement of the 2D Pb-I connectivity manifests as a reduction in electronic band curvature and minor increase in band gap, as evidence by comparison of electronic band structures in Figure 4.2.1b. These effects are inconsequential for the subsequent examination of the impact of organic functional groups on the frontier bands, as the 2D  $\text{PbI}_4^{2-}$  ‘surface’ should be an energetically conservative model of the 3D system ‘surface’ allowing for us to compare perturbations to the valence band maximum (VBM) and conduction band minimum (CBM) of the 2D material.

Using computational methods, this study details the utility of the 2D perovskite architecture in assessing the electronic implications of both

i) the organic cation in the bulk 2D system, as well as ii) passivation agents at grain boundaries in the larger family of 3D  $\text{PbI}_3^-$ -based materials. Using the 2D model we show that organic layers containing nitrogen lone pairs are expected to act as a chromophore (installing a new flat valence band) composed of N p-states, highlighting the potential photochemical non-innocence of common organic passivation agents.

Starting with a representative 2D perovskite, phenylmethylammonium lead iodide  $(\text{PMA})_2\text{PbI}_4$ <sup>206</sup>, the electronic band structure, Figure 4.2.2a, was generated using the Computational Method. The Z- $\Gamma$  vector is decidedly flat, corresponding to sampling in the crystallographic *c* direction (the direction with no covalent Pb-I connectivity, Figure 4.2.1a).  $(\text{PMA})_2\text{PbI}_4$  features a direct band gap of 1.8 eV at the  $\Gamma$  point, closely matching the experimental report<sup>206</sup>. Optical absorption spectra are presented in the Electronic Supplementary Information. Large band curvature is observed in the direction of Pb-I connectivity, where the VBM and CBM are composed of primarily iodine and lead orbitals, respectively.

Perturbations to  $(\text{PMA})_2\text{PbI}_4$  were made by substituting PMA for aliphatic cationic ammonium polymers, Figure 4.2.2. Upon geometric equilibration (details in Computational Methods) the electronic band structure of the system with only quaternary nitrogen (Figure 4.2.2b) show negligible perturbation, with both the curvature and composition of the bands remaining unchanged. The band structure does show reduced degeneracy owing to the asymmetric nature of the aliphatic carbon, reducing the cell to *P1*.

The experimentally relevant inclusion of tertiary amines in the backbone of the organic cation again yields a similar band gap and curvature in the conduction bands, Figure 4.2.2c-f. While the VBM remains unperturbed, the valence band shows the emergence of a highly localized nitrogen-based band which can be attributed to nitrogen lone pairs, Figure 4.2.2c-f. The flat band is unaffected by inter nitrogen chain length (as evidenced by Figure 4.2.2c and d). Increasing the concentration of lone pairs shows an increase in nitrogen density of states, Figure 4.2.2e, most extremely demonstrated by the inclusion of a polymer (Figure 4.2.2f). The nitrogen effect is further evidenced by the increase in hole effective mass ( $m_h^* = 0.44 m_o$  and  $m_h^* = 2.73 m_o$  for  $(\text{PMA})_2\text{PbI}_4$  and  $(\text{polymer})\text{PbI}_4$ , respectively). All hole effective masses are presented in Figure 4.2.2. The polymer-containing material is most relevant as it belongs to the same family of materials used for grain boundary passivation of the 3D counterparts<sup>108</sup>. In this case, our polymer features one amine lone pair per ammonium

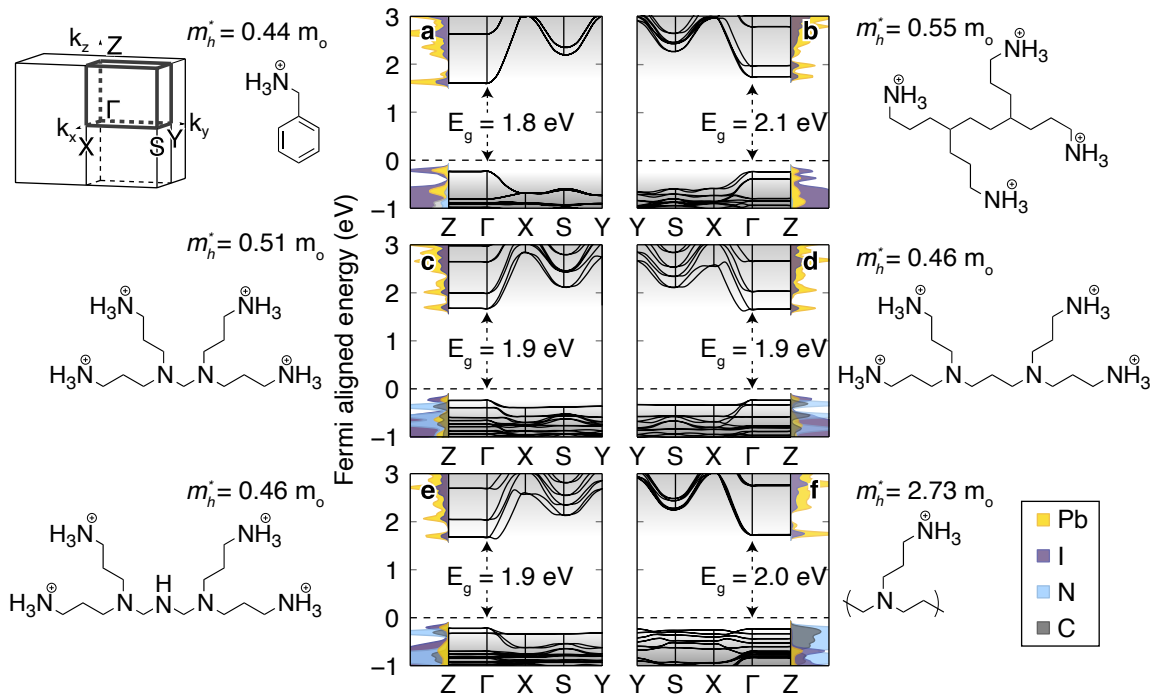


**Figure 4.2.2** Electronic band structures and density of states (DOS) of 2D perovskites with their corresponding organic cations. The  $\mathbf{k}$ -vectors map to space group  $Pbca$ , and the first Brillouin zone is shown. All electronic structures were computed using PBEsol+SOC. DOS is reported for  $\Gamma$  only. Organic molecules containing nitrogen lone pairs show nitrogen DOS near the VBM, which grows with increasing concentration of tertiary nitrogen.

tail and the band structure shows a significant contribution to the valence DOS from the amine group, suggesting that the lone pair should be a chromophore.

### IV.3 Conclusion

The emergence of nitrogen lone pairs to the valence band is concerning because the hole mobility of the material is directly determined by the valence band curvature. Remembering that the 2D VBM is likely higher in energy than the 3D surface, this is of particular concern because this could result in nitrogen lone pairs sitting midgap at a grain boundary of the 3D architecture.

In summary we concisely demonstrated that nitrogen lone pairs may be chromophores in  $PbI_n$ -based materials. Furthermore we also show that the 2D architectures are reasonable models for surfaces of 3D perovskites, allowing us to probe the electronic properties of relevant surfaces and grain boundaries. Beyond the results presented herein, we hope to have demonstrated the utility of the 2D architectures for further computational studies on the effects of organic substituents used in both 2D and 3D  $PbI_n$ -based materials.

#### IV.4 Computational Methods

Beginning with the experimentally determined structure of the 2D perovskite phenylmethylammonium lead iodide<sup>206</sup>, the organic cation was substituted for alternative aliphatic cations with protonation states adjusted for stoichiometric charge neutrality. The resultant materials were then geometrically equilibrated using the DFT functional PBEsol<sup>145</sup>, as implemented in VASP<sup>131</sup>. A 500 eV planewave cutoff and a 3x3x1 **k**-grid was determined to provide satisfactory convergences to within 0.005 eV per atom.

Spin-orbit coupling (SOC) is required to recover the accurate electronic structure of materials containing lead and iodine. Although HSE06 + 43% HF exchange + SOC has been shown to produce the correct electronic band gap and curvature, we cannot apply this to the 2D system due to computational expense. Instead, we note that PBEsol without SOC is found to recover the correct band gap through a systematic underestimation of band gaps: PBEsol+SOC underestimates the electronic band gap. Hence, the electronic structure presented in this paper uses the band structures computed with PBEsol+SOC with the conduction band energies adjusted to reflect the PBEsol band gap. Given the Pb-I connectivity was largely unaltered by the organic substitutions, we computed the electronic band structure using high symmetry points that map to the parent space group of the literature phenylmethylammonium lead iodide material, *Pbca*. Effective masses were calculated from VBM curvature recovered from a high resolution scan around  $\Gamma$ . Absorption spectra were computed from single point electronic calculations.

The electronic band structure of the 3D material was produced using the orthorhombic structure optimized using PBEsol, a 6x6x6 **k**-grid and 500 eV cutoff. The electronic band structure was produced using the same procedure as above.

## CHAPTER V

### A TYPE I HETEROINTERFACE BETWEEN AMORPHOUS $\text{PbI}_2$ OVERLAYERS ON CRYSTALLINE $\text{CsPbI}_3$ : OPPORTUNITIES FOR NANOCRYSTALS?

*The contents of this chapter have been or are intended to be published in whole or in part.  
The text presented here has been modified from the publication below:*

T. W. Kasel and C. H. Hendon, *Chem. Comm.*, 2020, \*In Preparation

#### **V.1 Bridge & Introduction**

As seen in the previous work, the contents of passivating agents can have adverse effects on the electrical properties of perovskite materials. Unfortunately, the inclusion of passivating agents has not been 100% effective at stopping moisture penetration, and has only been able to slow the degradation of the lattice. Furthermore, the effectiveness of passivating agents at preventing the other forms of degradation has not been thoroughly studied. In this regard, it is unknown whether passivating agents would be effective at preventing heat<sup>94,95,98</sup> or photoredox (in air)<sup>92,93</sup> degradation of the lattice. In all cases, protonation of the bridging iodides promotes the formation of  $\text{PbI}_2$  (the thermodynamic product), a process readily observed by a color change from the black  $\text{PbI}_3^-$  lattice to the characteristic yellow of  $\text{PbI}_2$ .<sup>96,211</sup> The presence of  $\text{PbI}_2$  in the perovskite lattice presents an obvious problem for photovoltaic applications due to its insulating nature. In this regard, the growth of  $\text{PbI}_2$  at surfaces and grain boundaries should result in a clear decrease in performance, especially when the perovskite grains become fully encompassed in a  $\text{PbI}_2$  shell. We were thus initially motivated in understanding the electronic effects of surface  $\text{PbI}_2$ .

From a bulk electronic structure perspective, (Figure 5.1.1), our calculations suggest that the formation of  $\text{PbI}_2$  on the surface of a lead iodide perovskite is hypothesized to have two primary effects on bulk material properties: i) the installation of shallow mid-gap trap states in the valence band, and ii) the widening of the band gap diminishing long range charge mobility. Hence, the emergence of  $\text{PbI}_2$  is

largely believed to be detrimental at both grain boundaries and at material surface contacts in photovoltaic devices. There is, however, some evidence that the presence of  $\text{PbI}_2$  may be beneficial, as Kim et al. has demonstrated that the existence of excess  $\text{PbI}_2$  boosts device performance.<sup>213</sup> While Kim's results are in agreement with other reports investigating the same phenomena, others have suggested that the presence of excess  $\text{PbI}_2$  acts more like a double-edged sword.<sup>214–216</sup> While Jacobsson et al., Liu et al., and Gujar et al. acknowledge that small amounts of excess  $\text{PbI}_2$  increases device efficiency, they demonstrate that excess  $\text{PbI}_2$  simultaneously decreases device stability. As such, there is currently a debate as to whether excess  $\text{PbI}_2$  should be explicitly avoided, or whether the formation of trace amounts of excess  $\text{PbI}_2$  should be welcomed. Our initial results seem to agree with the former, however, our simple band alignment image is insufficient to validate the former concern as the electronic properties of the  $\text{PbI}_2/\text{APbI}_3$  heterostructure will have dissimilar electronic properties to the bulk alignments, primarily due to band bending and redistribution of electrons. The alignment, however, provides an indication that the wider band gap will likely result in an Ohmic interfacial layer with the underlying  $\text{PbI}_3^-$  layers, lowering long range charge carrier mobility.

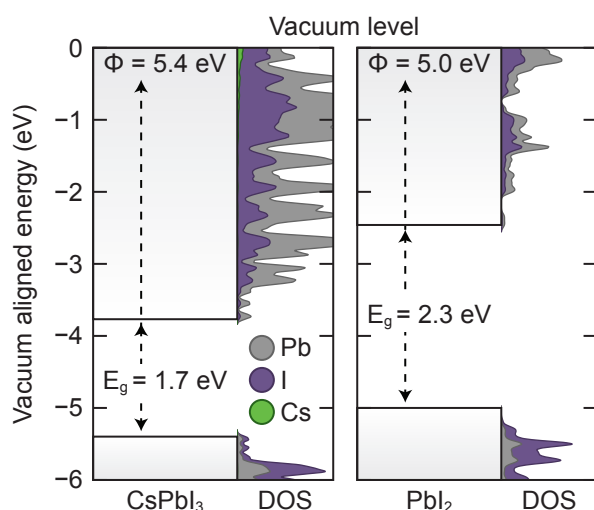


**Figure 5.1.1** Band edge diagram for  $\text{CsPbI}_3$  and  $\text{PbI}_2$ . The VBM of  $\text{PbI}_2$  lies within the gap of  $\text{CsPbI}_3$  suggesting that its existence results in mid gap states. The work function for  $\text{CsPbI}_3$  was obtained from literature.<sup>212</sup>

In addition to pondering the effect on photovoltaic properties, and motivated by our initial finding, we began to think about opportunities for using  $\text{PbI}_2$  overlayers as a novel route to forming supported nanocrystals as a functional result of lattice degradation. While this overlaying approach has been recently demonstrated for lead oxide overlayers (albeit not for nanocrystal formation explicitly),<sup>204</sup> the appeal of

using  $\text{PbI}_2$  formed by simple exposure to air offers a unique avenue to create novel crystal morphologies. Furthermore, our band alignment prediction suggests that, depending on the extent of energetic reordering arising from the interface,  $\text{PbI}_2$  overlayers could act much the same as the  $\text{PbO}_x$  overlayer, or analogous to  $\text{PbS}$

coatings on PbSe nanocrystals.<sup>217-219</sup> This would afford numerous new opportunities for formation of PbI<sub>2</sub>/APbI<sub>3</sub> hybrids. By inducing natural lattice degradation processes, a core@shell architecture could be readily generated. In this regard, the intensely studied degradation of perovskite lattices could provide a utility, rather than a persistent problem. Of course, these over layers are only useful if the surface states do not contribute to the valence and conduction band edges. In photovoltaics, such surface state contribution could act as charge carrier traps, likely lowering photovoltaic performance. For core@shell architectures, these band edge states would likely interfere with luminescent properties. It is therefore paramount that the location of PbI<sub>2</sub> states relative to a pristine PbI<sub>3</sub><sup>-</sup> lattice be elucidated. To make this assessment, we turned to more complicated models: amorphous lead iodide ( $\alpha$ -PbI<sub>2</sub>) overlayers on crystalline CsPbI<sub>3</sub> (*i.e.*  $\alpha$ -PbI<sub>2</sub>@CsPbI<sub>3</sub>).

## V.2 Results and Discussion

Using the Computational Methods, we constructed several variations of  $\alpha$ -PbI<sub>2</sub>@CsPbI<sub>3</sub> from a combined *ab initio* molecular dynamics and conventional DFT approach to recover realistic surface descriptions for these heterostructures, Figure 5.2.1a. Initially, we surmised that the resulting disorder of amorphous PbI<sub>2</sub> would exhibit an increase in valence band energy compared to crystalline 2D PbI<sub>2</sub> which is more stable than its amorphous derivative. Such predictions would lead to an exacerbation of the problems outlined from Figure 5.1.1. Furthermore, the pseudo-disorder of the periodically repeating amorphous PbI<sub>2</sub> structures contained within our models would minimize any artificial energetic contributions arising from heteroepitaxy. This results in an underestimation of the effects of amorphous PbI<sub>2</sub> on the electronic properties of a PbI<sub>3</sub><sup>-</sup> lattice. Thus, band alignment of amorphous PbI<sub>2</sub> containing models using absolute references such as those in Figure 5.1.1 would provide a "worst case scenario" prediction of the band alignments. As such, we elected to instead align to the PbI<sub>3</sub><sup>-</sup> lattice as i) by definition electronic states can be compared across models with the assumption that PbI<sub>3</sub><sup>-</sup> deep core-states are identical across all models, and ii) the extent and importance of perturbations caused by amorphous PbI<sub>2</sub> is drawn directly through comparison with the PbI<sub>3</sub><sup>-</sup> lattice. As the deformation on each side of the core is not identical, there is an artificial macroscopic dipole across the material. As comparisons are drawn from the band edge, however, such dipole should be inconsequential in conclusions drawn as they are formulated from a self referenced calculation. It should be noted that all our dissimilar structures had similar features: i) surface PbI<sub>2</sub> favored

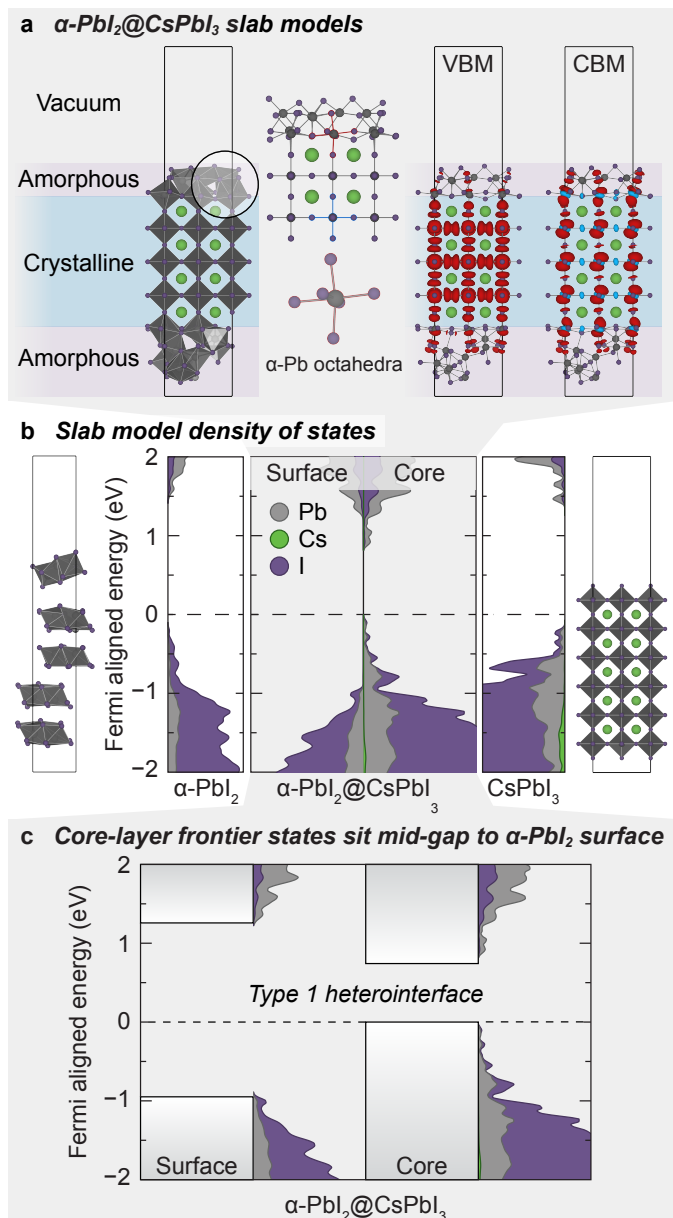


**Figure 5.2.1** a) Models used to recover the electronic effects of the decomposition of a pristine  $\text{PbI}_3^-$  lattice to  $\alpha\text{-PbI}_2$ . b)  $\alpha\text{-PbI}_2\text{@CsPbI}_3$  and its charge density calculated at the valance band maximum and conduction band minimum. Charge densities were plotted with an isosurface value of  $10^{-5} \text{ e}^-/\text{\AA}^3$ . c) Fermi aligned density of states were calculated using HSE06sol+SOC (PBEsol + 43% Hartree-Fock exchange + spin-orbit coupling). The  $\alpha\text{-PbI}_2$  region has an  $\sim 950 \text{ meV}$  and an  $\sim 1250 \text{ meV}$  energy barrier associated with hole transport and electron transport from the core to the surface, respectively.

the formation of octahedral Pb, ii) surface unsaturated iodides preferentially formed as many bonds as possible with surface Pb, and iii) the interface between the crystalline regions and the amorphous regions are incoherent.

Running our models in quadruplicate (to account for any anomalies and rare events possibly generated in a single *ab initio* molecular dynamics run), we find that contrary to Figure 5.1.1, no mid-gap states were introduced by the  $\alpha\text{-PbI}_2$  overlayer. By examination of both the orbital projection of the valence and conduction bands (Figure 5.2.1a), the surface iodides do not contribute to the frontier bands.

Furthermore, a comparison of slab models of both amorphous  $\text{PbI}_2$  and  $\text{CsPbI}_3$ , Figure 5.2.1b, the surface overlayers appear to bracket both the valence and conduction bands of the intact perovskite (in essence, a type I heterojunction). In photovoltaic applications, this installs a difficult to surmount energy

barrier for charge carriers. As such, if a  $\text{PbI}_2$  region exist between the location of charge carrier generation and its corresponding transport layer, it is likely that

photovoltaic performance will be hindered. However, this alignment is similar to those found for PbS@PbSe, as well as the PbO<sub>x</sub>@perovskite architectures, suggesting that the overlayers could prolong exciton lifetimes: Thus, could  $\alpha$ -PbI<sub>2</sub> be a useful overlayer in forming meta-stable nanoparticles?

While we cannot be conclusive in our assessment, the density of states plots provide some reasons to be optimistic. The density of states plot of  $\alpha$ -PbI<sub>2</sub>@CsPbI<sub>3</sub> in Figure 5.2.1c reveals that the highest energy occupied  $\alpha$ -PbI<sub>2</sub> state occurs  $\sim 0.95$  eV below the Fermi level. Similarly, the first unoccupied  $\alpha$ -PbI<sub>2</sub> state appears  $\sim 1.25$  eV above the Fermi level. Our amorphous layer pseudo-gap aligns nicely with the observed yellow color seen in experiments. However, the lack of  $\alpha$ -PbI<sub>2</sub> states within the band gap, or defining the band edges, indicates that  $\alpha$ -PbI<sub>2</sub> does not result in the mid-gap states predicted in Figure 5.1.1. Hence, we suggest that only when the ratio between the interfacial surface area and the bulk volume increases (*i.e.* very large surface area and low bulk volume) will these frontier  $\alpha$ -PbI<sub>2</sub> states have an observable effect on pristine bulk frontier band properties. Further, the interfacial charge density does not appear to alter the chemistry of the sub-surface CsPbI<sub>3</sub>, implying that the thickness of the amorphous region has little to no influence on the frontier electrical properties of the bulk. This suggests that the location of PbI<sub>2</sub> regions has a larger impact on photovoltaic performance than its size. As previously mentioned, photovoltaic performance is likely to be inhibited only if PbI<sub>2</sub> regions occur between the location of charge carrier generation and corresponding transport materials.

From the arguments above, we interpret these data to suggest that the addition of amorphous PbI<sub>2</sub> on the surface of CsPbI<sub>3</sub> does not result in mid gap states predicted from simpler bulk band edge alignments of their respective bulk crystalline models. Our DFT calculations indicate that  $\alpha$ -PbI<sub>2</sub> overlayers on crystalline CsPbI<sub>3</sub> generates a Type 1 semiconductor heterointerface, which ultimately does not affect the electronic properties afforded by the frontier states in CsPbI<sub>3</sub>. In this regard, techniques to induce lattice degradation could be utilized post-synthetically as a novel and simple path for generating perovskite core@shell architectures. Additionally, since the charge density of the models suggest that the thickness of the  $\alpha$ -PbI<sub>2</sub> shell has little impact on the electronics of the core, the extent of surface passivation as well as the quantum confinement experienced by the core, could readily be tuned by the extent of degradation induced post-synthetically. While these results are detrimental from a photovoltaic sense, we suspect that there are several opportunities for encapsulated

perovskite nanoparticles formed from controlled decomposition of  $\text{PbI}_3^-$  lattices.

### Computational Methods

Geometric optimizations were performed on  $\alpha\text{-PbI}_2@ \text{CsPbI}_3$ ,  $\text{PbI}_2$ , and  $\text{CsPbI}_3$  using a 500 eV planewave cutoff, a projector-augmented-wave (PAW) basis,<sup>151</sup> and a  $2 \times 2 \times 1$ , a  $4 \times 4 \times 1$ , and a  $2 \times 2 \times 1$  k-grid respectively. Density of states and charge densities were recovered using HSE06sol+SOC (PBEsol + 43% Hartree-Fock exchange + spin-orbit coupling).<sup>62,199,220,221</sup> All calculations were performed using the Vienna ab initio Simulation Package (VASP).<sup>131,132</sup> Slabs were constructed from the geometrically equilibrated bulk unit cell of  $\text{CsPbI}_3$ . To do so, the cell was expanded to a  $2 \times 2 \times 8$  supercell and 17.5 Å of vacuum was added. To create the  $\alpha\text{-PbI}_2@ \text{CsPbI}_3$  system, half of the  $\text{PbI}_3^-$  lattice was stoichiometrically exchanged for  $\text{PbI}_2$  by removal of equal amounts of Cs and I. The cell was thus comprised of half  $\text{CsPbI}_3$  and half  $\text{PbI}_2$  in a  $2 \times 2 \times 4 - 2 (\text{PbI}_2 - \text{CsPbI}_3 - \text{PbI}_2)$  configuration. For all calculations using this model, the atomic coordinates of core  $\text{CsPbI}_3$  were held constant (frozen) to provide a constant accurate description of a core  $\text{CsPbI}_3$  lattice. The  $\text{CsPbI}_3$  slab was created through a  $2 \times 2 \times 6$  supercell expansion, and a vacuum of approximately 30 Å was added to match the  $c$  lattice vector of  $\alpha\text{-PbI}_2@ \text{CsPbI}_3$ . To model a slab of  $\alpha\text{-PbI}_2$ , the optimized bulk of  $\text{PbI}_2$  was expanded in a  $1 \times 1 \times 5$  supercell expansion and 20 Å of vacuum was added.

*Ab initio* molecular dynamics simulations were then performed on  $\alpha\text{-PbI}_2@ \text{CsPbI}_3$  and  $\text{PbI}_2$  using a canonical ensemble (NVT) based upon the Nosé-Hoover thermostat.<sup>222-224</sup>  $\alpha\text{-PbI}_2@ \text{CsPbI}_3$  was heated to 600 K at 1 K per fs and then rapidly cooled and held at 300 K for 10 ps, to trap a high energy  $\alpha\text{-PbI}_2$  surface.  $\text{PbI}_2$  was heated to 500 K in 1 K per fs to simulate melting. In order to obtain statistical variability, all simulations of the  $\alpha\text{-PbI}_2@ \text{CsPbI}_3$  model were run in quadruplicate. Interfacial lead and iodide were treated as part of the core as they mostly retained their octahedral geometry and only exhibited slight distortion, shown in Figure 5.2.1a.

CHAPTER VI  
METAL-FREE PEROVSKITES FOR NON-LINEAR OPTICAL MATERIALS

*The contents of this chapter have been or are intended to be published in whole or in part.  
The text presented here has been modified from the publication below:*

Kasel, T. W., Deng, Z., Mroz, A. M., Hendon, C. H., Butler, K. T., and Canepa, P.,  
*Chem. Sci.*, 2019, **10**, 8187

### **VI.1 Bridge & Introduction**

Over the course of this PhD, a new class of interesting perovskites has emerged. These perovskites do not contain the typical divalent metal in the B-site; They do not contain a metal at all, and have thus been named metal-free perovskites.<sup>225</sup> In Ye et al. original work, the B-site was inhabited by  $\text{NH}_4$ , leading to a larger than traditional cation in the A-site. In order to preserve charge neutrality, the A-site is occupied by a dication. Metal-free perovskites, as will be presented later, contain band gaps significantly larger than traditional perovskite materials ( $> 5.5\text{eV}$ ), making them unsuitable for photovoltaic applications. However, the occupation of a molecular species at the B-site, alongside a larger, more charged A-site, gives rise to exceptionally unique optical properties not normally exhibited by the perovskite family of materials. Additionally, an organic B-site allots a wider range of molecular diversity in both the A- and B-site cations, increasing the number of unique structures (and thus interesting properties for an array of applications) available to the research community.

New unique optical properties are often the result of a dramatic change in the crystal symmetry. For example, the reduction of crystal symmetry that comes with augmenting the  $\text{BX}_3$  octahedron, when performed correctly, transforms the space group of the material from a centrosymmetric group to a noncentrosymmetric group. This is achieved through the loss of inversion symmetry, to be specific centrosymmetric groups have inversion symmetry while noncentrosymmetric groups do not. The loss of inversion symmetry, alongside the phase matching criteria, allows metal-free

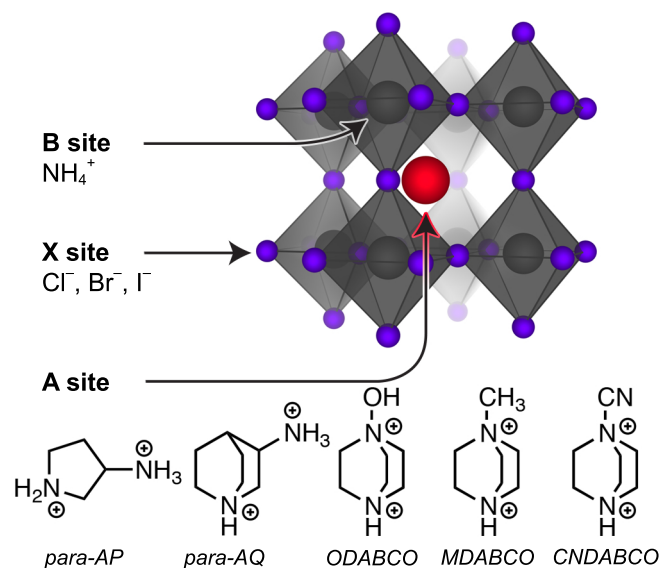


**Figure 6.1.1** Polyhedra representation of a metal-free  $ABX_3$ -type perovskite, where  $A$  can be one of the four organic cations (also shown by the red ball),  $B$  is  $\text{NH}_4^+$  (grey ball) and  $X$  the halide ion, i.e.  $\text{Cl}^-$ ,  $\text{Br}^-$  and  $\text{I}^-$  (purple balls). The nature of the  $A$  cation is also shown.

perovskites to exhibit a second order NLO response.

The all-inorganic perovskite  $\text{CsPbI}_3$  falls into the centrosymmetric space group #221 and thus cannot readily exhibit second order NLO properties. It may seem like an obvious conclusion that the organic-inorganic hybrid perovskites must

be in noncentrosymmetric space groups due to the resulting disorder of their A-site organic cations, however, the rotation freedom that the A-site cations exhibit at moderate temperatures<sup>104</sup> allows them to be approximated as spheres. Their symmetry, therefore, can thus be treated in a fashion similar to  $\text{CsPbI}_3$ , placing them in space group #221. In this regard, augmenting the chemical makeup of the  $\text{BX}_3$  octahedron appears to be the most reliable way to achieve such results. Augmenting perovskites in such a manner to generate a NLO response offers a way to diversify both the application of perovskite based devices while simultaneously expanding the NLO markets/field.

Recently, NLO and SHG have been at the heart of several technological revolutions. With the advent of the internet, conveying information and data by means of fibre-optics and lasers have transformed telecommunications. The development of fiberoptic devices with increased performance has fueled a surge of interest in the development of materials with ever-increasing data-transfer capabilities.<sup>226-235</sup> Materials, such as  $\text{LiNbO}_3$  and  $\text{LiTaO}_3$  with NLO and SHG are at the core of high-speed electro-optic modulator devices, significantly boosting the transmission capacities of the telecommunication infrastructure ( $\sim 10 \text{ Gbit s}^{-1}$ ).<sup>226,236</sup> In parallel, NLO materials for deep-UV lasers are being used in semiconductor manufacturing, photolithography, laser systems, and advanced instrument development.

The demand for apparatus with increased performance requires the development

of novel inexpensive NLO materials and every year the electronic and telecommunication industries demands the production of  $\sim 40,000$  tons of  $\text{LiNbO}_3$ . The soaring costs of lithium and niobium,<sup>237,238</sup> and thus  $\text{LiNbO}_3$ , requires the development of the new generation of NLO materials relying on more earth-abundant elements.<sup>239-241</sup> This is further aggravated by the fact that  $\text{LiNbO}_3$  melts incongruently and the manufacturing of congruently lithium niobate single crystals requires cooling of Li-poor nonstoichiometric melts of  $\text{LiNbO}_3$ ,<sup>242</sup> adding additional production costs.

Meanwhile, for deep-UV applications Tran *et al.*<sup>234</sup> have shown that only a handful of materials, i.e.,  $\text{KBe}_2\text{BO}_3\text{F}_2$ ,  $\text{RbBe}_2\text{BO}_3\text{F}_2$  and  $\text{CsBe}_2\text{BO}_3\text{F}_2$ , sharing similar structural features currently fulfill the desired requirements. However, these materials contain toxic Be, whose usage is prohibited in many countries. Therefore, materials with better NLO characteristics are required to supplant deep-UV lasers.<sup>235</sup> As identified by Halasyamani and Rondinelli,<sup>235</sup> NLO materials for application in deep-UV lasers must fulfil a minimal number of requirements: *i*) the atoms in the material should present a noncentrosymmetric arrangement, *ii*) the material absorbs light in the deep-UV spectrum (i.e., absorption wavelengths  $\geq 175$  nm), and *iii*) the material should respect the phase-matching criteria discussed later.

One promising route towards sustainable NLO materials lies in organic materials, which have shown promising SHG properties.<sup>228,243-253</sup> However, to date organic NLO suffer from thermal instability and difficult fabrication. In contrast to typical organic-based NLO, metal-free perovskites have been shown to be structurally stable beyond 200 °C.<sup>225</sup>

In this study we present an in-depth analysis of the NLO properties of a new class of materials with ferroelectric response termed metal-free perovskites developed by Ye and co-workers.<sup>225</sup> We use first-principles calculations, based on density functional theory (DFT) to chart the optical and NLO properties of a these novel metal-free perovskites. In contrast to typical inorganic perovskite  $A^{2+}B^{4+}O_3^{2-}$  where *A* and *B* are metal cations (e.g.,  $\text{CaTiO}_3$ ), in metal-free perovskites the *A* and *B* cations are replaced by organic units. The rich choice of organic units introduces the possibility of tailoring the functional properties of such metal-free perovskites, while being easy-to-synthesize, affordable and non-toxic. Note that NLO materials with inorganic perovskite structures exist (e.g.,  $\text{K}_3\text{B}_6\text{O}_{10}\text{Cl}$ ) which are more closely related to the metal-free perovskites than organic-based NLO materials.<sup>254</sup>

We investigate such metal-free perovskites as NLO materials for SHG applications,

and verify whether these perovskites are suitable as deep-UV NLO materials. Our findings reveal that metal-free perovskites, based on the organic moieties N-methyl-N-diazabicyclo[2.2.2]octonium (MDABCO<sup>2+</sup>) and N-hydroxy-N-diazabicyclo[2.2.2]octonium (ODABCO<sup>2+</sup>), possess SHG response, with magnitudes similar to some inorganic contenders, such as KBe<sub>2</sub>BO<sub>3</sub>F<sub>2</sub>, RbBe<sub>2</sub>BO<sub>3</sub>F<sub>2</sub> and CsBe<sub>2</sub>BO<sub>3</sub>F<sub>2</sub>. We demonstrate that organic groups presenting intrinsic dipole moments can contribute positively to the ferroelectric response of the material, and provide an increased NLO response.

On the basis of our predictions, we provide guidelines to improve the SHG response of the metal-free perovskites, by tailoring the structural features of the organic cations. Following this principle, we extend the computational search to new structures. For example, we show the case where the hydroxy-group in ODABCO<sup>2+</sup> (A-cation) is effectively replaced by a cyanide CN<sup>-</sup> group with increased polarity, which provides remarkable NLO response. While preliminary observations<sup>225</sup> showed experimentally SHG response in MDABCO-NH<sub>4</sub>I<sub>3</sub>, we also identify ODABCO-NH<sub>4</sub>I<sub>3</sub> and CNDABCO-NH<sub>4</sub>I<sub>3</sub> as superior SHG materials, and their properties should be carefully verified experimentally.

## VI.2 Results

### VI.2.1 Structure of ferroelectric metal-free perovskites

The first point when considering the suitability of a material for NLO applications is the crystal structure. All materials reported herein and shown in Figure 6.1.1 feature the typical perovskite ABX<sub>3</sub> structure (where *A* and *B* are cations and *X* are anions), with BX<sub>3</sub> corner-sharing octahedra and charge-balancing *A* cations in the cavities of the framework. The structures investigated have NH<sub>4</sub><sup>+</sup> as *B* sites and halide X<sup>-</sup> sites, as seen in Figure 6.1.1. A series of different *A* site divalent molecular cations are considered (i) N-methyl-N-diazabicyclo[2.2.2]octonium (MDABCO<sup>2+</sup>), (ii) N-hydroxy-N-diazabicyclo[2.2.2]octonium (ODABCO<sup>2+</sup>), (iii) R-3-ammonioquinuclidinium (R-3AQ<sup>2+</sup>), and (iv) S-3-ammoniopyrrolidinium (S-3AP<sup>2+</sup>). Starting from the ODABCO-NH<sub>4</sub>X structures, we also replaced the hydroxy group with a more polar cyanide CN<sup>-</sup> group forming a new metal-free perovskite termed CNDABCO-NH<sub>4</sub>X<sub>3</sub>.

In studying the halide chemical space of these metal-free perovskites, we proposed three new structures, including MDABCO-NH<sub>4</sub>Cl<sub>3</sub>, ODABCO-NH<sub>4</sub>I<sub>3</sub> and S-3AP-NH<sub>4</sub>I<sub>3</sub>

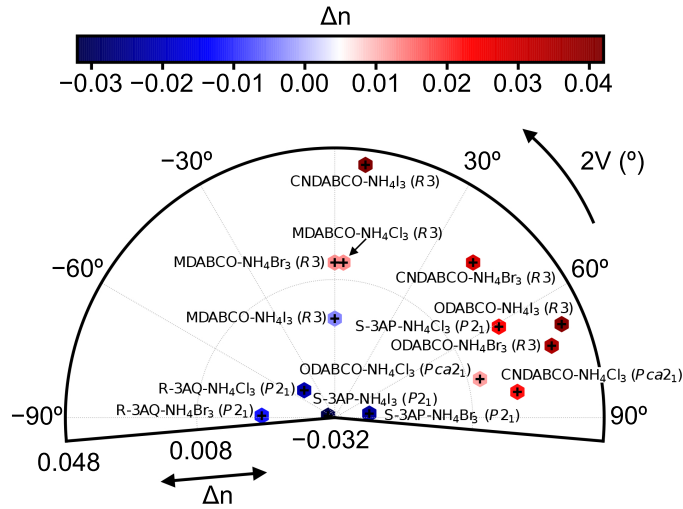


**Figure 6.2.1** Computed birefringence  $\Delta n$  and  $2V$  angle of metal-free perovskites at their experimental volume and lattice constants.  $\Delta n$  is plotted on the radial axis and using the colour-bar, with red indicating positive  $\Delta n$ . Values of  $n$  are given in Table S3 of the SI. The  $2V$  angles provide information about the nature of the birefringence in biaxial crystals.

space groups,  $R3$ ,  $Pca2_1$  and  $P2_1$ , all of which are non-centrosymmetric. For those metal-free perovskites that have been synthesized and characterized previously the non-centrosymmetric space groups persisting up to 448 K.<sup>225</sup>

In addition, metal-free perovskites, and inorganic materials, such as  $\text{LiNbO}_3$  possess an intrinsic polarization, which is typical of ferroelectric materials.  $\text{LiNbO}_3$  charts among the most popular of NLO materials with a polarization of  $\sim 70\text{-}75 \mu\text{C}/\text{cm}^2$ .<sup>255</sup> The presence of dipolar molecules and the off-centering of the  $B$ -site cation in the metal-free perovskites indicates the existence of an intrinsic polarization, which for  $\text{MDABCO-NH}_4\text{I}_3$  has been measured to be  $\sim 19 \mu\text{C}/\text{cm}^2$ .<sup>225</sup>

## VI.2.2 Birefringence activity of Metal-free Perovskites

Having established the crystallographic criteria for NLO materials, we now consider the optical properties that must be satisfied for SHG. The birefringence is the maximum difference refractive indices ( $n$ ) which depends on the propagation directions of light in the crystal at a fixed frequency ( $\omega$ ) (as in Eq. VI.2.1).

$$\Delta n = n_{\max}(\omega) - n_{\min}(\omega) \quad (\text{VI.2.1})$$

that were not identified by Ye *et al.*<sup>225</sup> In the case of  $\text{ODABCO-NH}_4\text{I}_3$  and  $\text{CNDABCO-NH}_4\text{X}_3$  we assumed a  $R3$  space group. However, we also computed the Iodine-based polymorph with  $Pca2_1$  space group (as in  $\text{ODABCO-NH}_4\text{Cl}_3$ ), which converted to the  $R3$  polymorph.

To be NLO active a material must be non-centrosymmetric. As shown in Table S1 and Table S2 of the Supporting Information (SI), the materials considered here fall into three

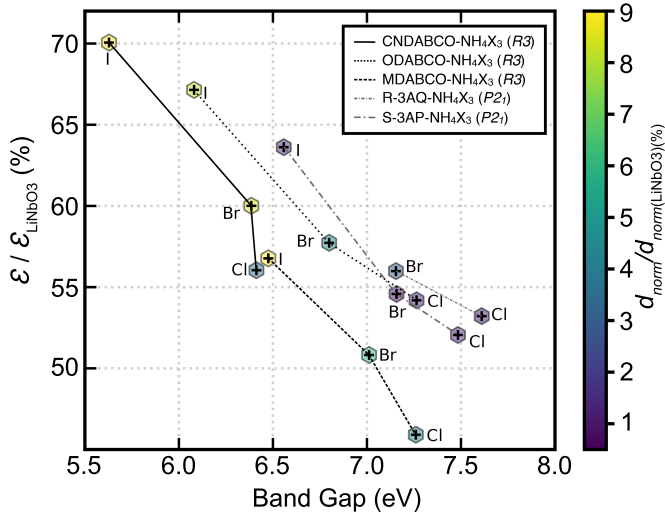


**Figure 6.2.2** Computed static  $d_{\text{norm}}$  (colour-bar) as function of the band gap (x-axis, eV) and average dielectric constant (y-axis) of the metal-free perovskites at the experimental volume. The  $\epsilon$  values (in the static limit) computed for the metal-free perovskites are normalised against the  $\text{LiNbO}_3$  ( $\sim 4.39$ ). Similarly, the values of  $d_{\text{norm}}$  are rescaled to that of  $\text{LiNbO}_3$  ( $\sim 17.91$  pm/V). The space group of each structure is also reported.

SHG occurs efficiently whenever the refractive index  $n$  of the  $2^{\text{nd}}$  harmonic is equal (or close) to that of the generating wave at half-frequency, i.e.,  $n(2\omega) = n(\omega)$ —this condition is termed phase-matching. Phase-matching requires a suitable range of frequencies with refractive indexes,  $n_{\text{max}}(\omega) - n_{\text{min}}(2\omega) > 0$ , with  $n_{\text{min}}$  and  $n_{\text{max}}$  the lowest and the largest refractive index in the spread.<sup>256</sup>

If  $\Delta n$  of a material is too small the phase-matching condition for SHG will not

occur. If  $\Delta n$  is too large the material will exhibit spatial beam walk-off, where the intensity distribution of the wave drifts away from the direction of propagation resulting in reduced SHG intensity. In general a moderate birefringence ( $\Delta n \approx 0.07$ ) is desired.

In uniaxial systems, such as  $\text{LiNbO}_3$  and the  $\text{MDABCO-NH}_4\text{X}_3$  systems the direction of ordinary and extraordinary rays occurs along the optical axis, which lays along the highest symmetry axis.

In contrast, biaxial systems have multiple optic axes, whose directions of propagation depend on the diffraction index and measured by the 2V acute angle (see below).<sup>256</sup> Therefore, the 2V angle provides information about the nature of the birefringence in biaxial crystals. In general, orthorhombic, monoclinic and triclinic systems are biaxial crystals.

Figure 6.2.1 plots  $\Delta n$  (obtained from the dielectric constants in the static regime) and the 2V acute angle. From Figure 6.2.1, we observe that all the systems considered here have  $\Delta n$  ranging between values of  $-0.03$  and  $+0.05$ , with CNDABCO, ODABCO, S-3AP and R-3AQ-based perovskites charting among the highest in magnitude. The R3 materials, which are uniaxial NLO systems, all exhibit positive birefringence. In

contrast, the  $Pca2_1$  and  $P2_1$  systems, which are biaxial NLO materials, display both positive and negative birefringence. A closer look at Figure 6.2.1 shows that with the exception of MDABCO-based perovskites and S-3AP-NH<sub>4</sub>I<sub>3</sub> (whose  $2V \sim 0$ ), the remaining materials all show a rather complex biaxial response.

### VI.2.3 NLO response in Metal-free Perovskites

We now discuss the NLO response of the metal-free perovskites. Among the prerequisites for SHG the materials under investigation should display a non-negligible value of the second order dielectric tensor,  $\chi^{(2)}$ .

$\chi_{ijk}^{(2)} = 2d_{ijk}$  is a third-rank tensor as defined in Eq. VI.5.4, and therefore can be difficult to analyse intuitively. The  $i$ ,  $j$  and  $k$  components of the  $d$  tensor identify the directions of the applied electric fields (i.e.,  $j$  and  $k$ ) of the incident radiation and the polarization of the generated second harmonic (i.e.,  $i$ ), respectively, (see Eq. VI.5.4). In SHG experiments, the directions of the electric fields of incident radiations have frequencies  $\omega_1$  and  $\omega_2$  (with  $\omega_1 = \omega_2$  in SHG) and the second harmonic wave with frequency  $\omega_3 = \omega_1 + \omega_2$ . A complete discussion of the  $\chi^{(2)}$  and  $d$  tensors and their dependence can be found in Ref. 165.

A useful proxy for presenting the  $ijk$  component of the static  $\chi^{(2)}$  tensor is the norm of the  $d_{ijk}$  components of Table 6.2.1 and Eq. VI.2.2:

$$||d_{\text{norm}}|| = \sqrt{\sum_{ijk} d_{ijk}^2} \quad (\text{VI.2.2})$$

$d_{\text{norm}}$  has been utilised previously<sup>241,257</sup> and is more effective of a simple geometric mean of the  $d_{ijk}$  components, which can assume values approaching numerical zeros given the oscillations in sign of the  $d_{ijk}$  values (see Table 6.2.1). We note that the values  $d_{\text{norm}}$  are by definition larger in magnitude of any component  $d_{ijk}$ , but here  $d_{\text{norm}}$  serves us simply to compare each materials investigated on the same footing.

Figure 6.2.2 presents the static dielectric constant  $\epsilon$  (y-axis) as a function of the band gap (x-axis) for the materials studied, the data points are colored according to the magnitude of  $d_{\text{norm}}$ , which are obtained at the experimental volumes at room temperature. The values of band gap,  $\epsilon$ ,  $\chi^{(1)}$ ,  $\chi_{ijk}^{(2)}$  and  $d_{\text{norm}}$  of these materials are

**Table 6.2.1** Computed static  $d_{ijk}$  components of the  $\chi^{(2)}$  tensor and their norm  $d_{\text{norm}}$  (in pm/V) of the metal-free perovskites at the experimental volumes. Spg. is the space group.

$X^-$	Spg.	$d_{xxx}$	$d_{xyx}$	$d_{xxz}$	$d_{xyy}$	$d_{xyz}$	$d_{xzz}$	$d_{yyy}$	$d_{yyz}$	$d_{yzz}$	$d_{zzz}$	$\ d_{\text{norm}}\ $
MDABCO–NH <sub>4</sub> X <sub>3</sub>												
Cl	<i>R3</i>	0.140	−0.410	0.048	−0.140	0.000	0.000	0.410	0.048	0.000	−0.490	0.79
Br	<i>R3</i>	0.230	−0.620	−0.058	−0.230	0.000	0.000	0.620	−0.058	0.000	−0.580	1.10
I	<i>R3</i>	−0.170	1.200	0.430	0.170	0.000	0.000	−1.200	0.430	0.000	0.021	1.80
ODABCO–NH <sub>4</sub> X <sub>3</sub>												
Cl	<i>Pca2</i> <sub>1</sub>	0.000	0.000	0.230	0.000	0.000	0.000	0.000	−0.076	0.000	−0.076	0.25
Br	<i>R3</i>	0.019	0.510	−0.320	0.150	−0.290	−0.069	0.099	−0.100	−0.280	−0.230	0.79
I	<i>R3</i>	0.270	0.620	−0.670	−0.190	−0.400	0.100	−0.840	−0.490	−0.280	0.007	1.50
CNDABCO–NH <sub>4</sub> X <sub>3</sub>												
Cl	<i>Pca2</i> <sub>1</sub>	0.000	0.000	0.650	0.000	0.000	0.000	0.000	−0.160	0.000	0.075	0.68
Br	<i>R3</i>	−0.450	0.850	0.260	0.230	0.120	0.092	−0.880	0.350	0.071	−0.590	1.50
I	<i>R3</i>	−0.450	1.310	0.760	0.450	−0.001	0.0006	−1.310	0.760	0.004	−0.014	2.20
R–3AQ–NH <sub>4</sub> X <sub>3</sub>												
Cl	<i>P2</i> <sub>1</sub>	0.000	0.091	0.000	0.000	0.068	0.000	0.012	0.000	−0.160	0.000	0.19
Br	<i>P2</i> <sub>1</sub>	0.000	−0.075	0.000	0.000	0.004	0.000	−0.320	0.000	0.400	0.000	0.52
S–3AP–NH <sub>4</sub> X <sub>3</sub>												
Cl	<i>P2</i> <sub>1</sub>	0.000	−0.025	0.000	0.000	−0.041	0.000	−0.160	0.000	−0.150	0.000	0.22
Br	<i>P2</i> <sub>1</sub>	0.000	−0.029	0.000	0.000	−0.055	0.000	−0.120	0.000	−0.048	0.000	0.14
I	<i>P2</i> <sub>1</sub>	0.000	−0.210	0.000	0.000	−0.075	0.000	−0.140	0.000	0.029	0.000	0.26
LiNbO <sub>3</sub>												
—	<i>R3c</i>	0.170	0.000	5.000	0.170	0.000	0.000	0.000	5.000	0.000	16.450	17.91

found in Table S4 and Table S5.

In general, volumes obtained after relaxation in hybrid systems containing a number of Van der Waals interactions, such as these metal-free perovskites, tend to be highly distorted. Therefore, the main text concentrates on results obtained on structures where all the atomic coordinates are relaxed at the experimental volumes and lattice constants, whereas results on fully relaxed structures are available in the SI. For clarity and ease of comparison, the dielectric constant and the  $d_{\text{norm}}$  are scaled by that of  $\text{LiNbO}_3$ , calculated at the same level of theory (Table S4 and Table S5).

The y-axis of Figure 6.2.2 presents the average dielectric constant (in the static limit) of the metal-free perovskites rescaled to that of  $\text{LiNbO}_3 \sim 4.39$ , which compare well with experimental data ( $\sim 4.87$ ).<sup>255</sup> The computed  $d_{\text{zzz}}$  values of 16.45 pm/V (at the experimental volume of  $\text{LiNbO}_3$ ) slightly underestimated the experimental value of ( $\sim 22.0$  pm/V at  $\lambda \sim 407.2$  nm) by Magel *et al.*<sup>258</sup> DFT has been known to systematically underestimate values of  $d$  in NLO materials.<sup>259</sup> The complete dielectric and  $d$  tensors of each metal-free perovskites are reported in the SI.

The computed band gaps of Figure 6.2.2 are characteristic of high-gap insulators ranging between  $\sim 5.5$  and 8 eV. The metal-free perovskites absorb light between 155 and 220 nm, i.e. the deep-UV portion of the electromagnetic spectrum, meaning that these materials fulfil another of the criteria for deep-UV SHG applications. All computed  $d_{\text{norm}}$  values in metal-free perovskites with the same organic A-site cation follow the order  $\text{I} > \text{Br} > \text{Cl}$ . The order of increasing  $d_{\text{norm}}$  moving down the halide group follows the trend in band gaps. We find that the computed  $d_{\text{norm}}$  of all the metal-free perovskites is a fraction (ranging between 1% and 10%) of the the  $d_{\text{norm}}$  of  $\text{LiNbO}_3$  (Figure 6.2.2), which is used as a reference.

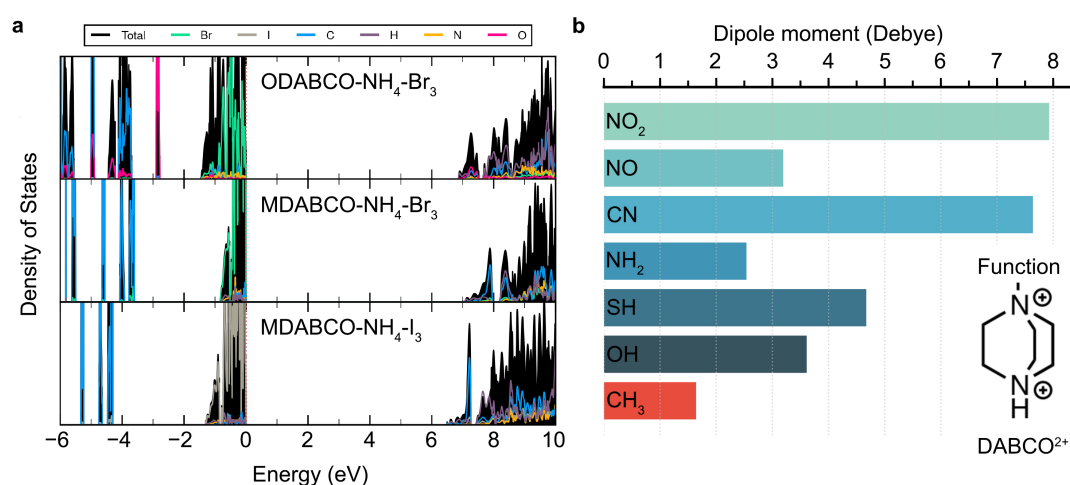
From these data, we identify two iodine-based structures, MDABCO- $\text{NH}_4\text{I}_3$  and ODABCO- $\text{NH}_4\text{I}_3$  as the best NLO materials across the metal-free perovskites investigated. When the  $\text{OH}^-$  group in ODABCO- $\text{NH}_4\text{X}_3$  is replaced by a polar  $\text{CN}^-$  group (see Figure 6.2.2), forming CNDABCO- $\text{NH}_4\text{X}_3$ , we find improved NLO properties. In CNDABCO- $\text{NH}_4\text{X}_3$ , the computed  $d_{\text{norm}}$  of  $\sim 2.23$  pm/V outperforms all other metal-free perovskites, suggesting that CN-substituted A cations offer a promising strategy to improve the optoelectronic properties of these materials.

Figure 6.2.2 shows that both R-3AQ- $\text{NH}_4\text{X}_3$  and S-3AP- $\text{NH}_4\text{X}_3$  possess small values of  $d_{\text{norm}}$ , covering a narrow range between  $\sim 0.14$  and  $\sim 0.52$  pm/V, with the highest value set by R-3AQ- $\text{NH}_4\text{Br}_3$  and the lowest by S-3AP- $\text{NH}_4\text{Br}_3$ . Hence, both

R-3AQ-NH<sub>4</sub>X<sub>3</sub> and S-3AP-NH<sub>4</sub>X<sub>3</sub> are expected to show low SHG behavior and therefore, will not be considered further in this analysis.

### VI.3 Discussion

We have identified that MDABCO-NH<sub>4</sub>I<sub>3</sub>, ODABCO-NH<sub>4</sub>I<sub>3</sub> and CNDABCO-NH<sub>4</sub>I<sub>3</sub> show the largest NLO response. Our results show the largest components of the  $d$  tensor in MDABCO-NH<sub>4</sub>I<sub>3</sub> are  $d_{xxz} = d_{yyz} \sim 0.43$  pm/V and  $d_{xxy} \sim 1.20$  pm/V, respectively,  $d_{yyy} \sim 0.84$  pm/V in ODABCO-NH<sub>4</sub>I<sub>3</sub> and  $d_{yyy} \sim 1.31$  pm/V in CNDABCO-NH<sub>4</sub>I<sub>3</sub>, which represent three promising NLO materials with good SHG. Therefore, the discussion will only focus on the subset of metal-free perovskites showing significant SHG activity, including CNDABCO-NH<sub>4</sub>I<sub>3</sub>, ODABCO-NH<sub>4</sub>X<sub>3</sub> and MDABCO-NH<sub>4</sub>X<sub>3</sub>.



**Figure 6.3.1** a Total and projected density of states of ODABCO-NH<sub>4</sub>Br<sub>3</sub>, MDABCO-NH<sub>4</sub>Br<sub>3</sub> and MDABCO-NH<sub>4</sub>I<sub>3</sub> obtained with PBEsol0-D3. The red line (dash) is the Fermi energy, which is set at the top of the valence band of each material. b Variance of dipole moment for DABCO cations substituted with a number of organic groups (functions).

The values for SHG are similar and in most cases even larger than the prescribed minimal conditions for deep-UV applications, i.e.  $d_{xyz} \sim 0.39$  pm/V (with  $\lambda \sim 1.064$   $\mu\text{m}$ ) KH<sub>2</sub>PO<sub>4</sub>.<sup>234,260</sup> The calculated band gaps indicate that while the materials absorb in the  $2\omega$  range required for SHG, they do not absorb in the region  $\omega$ , a critical consideration, as absorption at  $\omega$  would lead to material damage in operation. It is important to note that in a operation scenario the light absorbed will enhance the susceptibility but will also reduce the emission, thus the calculate values of  $d_{xyz}$  serve to demonstrate the very promising properties of these materials for NLO and SHG applications, but should be considered as guides, rather than definitive numbers of real device operation. Most importantly, the composition-structure-property relationships driving NLO response in these test systems can provide rules for designing even more SHG active materials.

As seen in Figure 6.2.2, the primary factor influencing the size of  $d_{\text{norm}}$  is the magnitude of the band gap. This is a well established trend in semiconductor materials in general and is related to lower carrier concentrations in wider gap materials at finite temperatures. A correlation between band-gap and the halide species exists, we find a similar correlation in the values of the static dielectric constants vs. the anion species, following the trend  $\epsilon(\text{I}^-) > \epsilon(\text{Br}^-) > \epsilon(\text{Cl}^-)$ . This observation is consistent with the density of states of Figure 6.3.1 of ODABCO-NH<sub>4</sub>Br<sub>3</sub> (top), MDABCO-NH<sub>4</sub>Br<sub>3</sub> (middle) and MDABCO-NH<sub>4</sub>I<sub>3</sub> (bottom), respectively, which shows the valence band dominated by halide species and the conduction band populated by the A organic cation, i.e., ODABCO<sup>2+</sup> or MDABCO<sup>2+</sup>. As the frontier valence orbitals are primarily halide in character (Figure 6.3.1), it is not surprising that the largest change in band gap is controlled by halide exchange. These findings are also supported by the DOS presented in Ref. 261 and are consistent with observations in hybrid halide perovskites.<sup>262</sup>

There is a secondary contribution to the  $d_{\text{norm}}$  arising from the nature of the organic cation at the A-site. As seen in Figure 6.2.2,  $d_{\text{norm}}$  follows the order  $d_{\text{norm}}(\text{CNDABCO}^{2+}) \gg d_{\text{norm}}(\text{MDABCO}^{2+}) > d_{\text{norm}}(\text{ODABCO}^{2+})$ . However, this trend becomes  $d_{\text{norm}}(\text{CNDABCO}^{2+}) \gg d_{\text{norm}}(\text{ODABCO}^{2+}) > d_{\text{norm}}(\text{MDABCO}^{2+})$  when the structures are fully relaxed (see Table S5). This is despite the fact that both CNDABCO<sup>2+</sup> and ODABCO<sup>2+</sup> systems have larger dielectric constants and smaller band gaps than the MDABCO<sup>2+</sup> counterparts. As an example, while the ODABCO<sup>2+</sup> cation is structurally very similar to the group MDABCO<sup>2+</sup> (see Figure 6.1.1), the apical methyl group in MDABCO<sup>2+</sup> is substituted by a polar OH<sup>-</sup> in ODABCO<sup>2+</sup>. The presence of polar moieties in the organic cations, such as the CN<sup>-</sup> and OH<sup>-</sup> groups in CNDABCO<sup>2+</sup> and ODABCO<sup>2+</sup>, can result in a greater intrinsic electric dipole moments, whose polarisation induces an increase of the dielectric constant. The intrinsic electric dipole moment introduced by the CN<sup>-</sup> or the OH<sup>-</sup> groups increase the overall dipole of CNDABCO<sup>2+</sup> from  $\sim 3.61$  Debye to  $\sim 7.64$  Debye, compared to MDABCO<sup>2+</sup>  $\sim 1.64$  Debye, which is reflected by the values of dielectric constants of Figure 6.2.2.

Thus, the highly modular nature of the A site cation, in particular the DABCO group, afforded by a metal-free scaffold can be exploited to fine-tune the NLO response of these perovskites. For example, the substitution of the CH<sub>3</sub> group on MDABCO with highly polar organic groups, such as -SH (thiol), -NH<sub>2</sub> (amine), -NO (nitroso) and -NO<sub>2</sub> (nitro), whose computed electrical dipole moment are shown in Figure 6.3.1b, represents a viable strategy to increase the NLO response of these metal-free

perovskites. Indeed, in Figure 6.2.1 we have demonstrated that replacing the CH<sub>3</sub> (or OH) with the CN moiety, increases substantially the values of  $d_{\text{norm}}$ , thus providing a clear design rule to design novel metal-free perovskites.

The properties and tunability demonstrated in metal-free perovskites are comparable to organic-based NLO materials. Organic NLOs can supersede the performance in terms of descriptors,  $\chi^{(2)}$  (see Eq. VI.5.4), even by 1-2 orders of magnitude of the inorganic NLO materials discussed so far.<sup>228,243-253</sup> Some of these materials are even commercial.<sup>228,263,264</sup> For example, the 4-N,N-dimethylamino-4'-N'-methyl-stilbazolium tosylate (DAST) forms organic crystals with a superior non-linear susceptibility  $d \sim 580$  pm/V (with  $d = 0.5\chi^{(2)}$ ).<sup>246,250</sup> However, organic-based NLOs display at least three major limitations curbing their use in optical devices:<sup>248,252</sup> *i*) difficult to obtain sufficiently large-size crystals, *ii*) limited thermal stability above 200 °C and *iii*) low mechanical strength. For example, while a good NLO organic material, such as the 3-methyl-4-methoxy-4'-nitrostil-bene has a 1<sup>st</sup> hyperpolarizability  $\beta$  (see Eq. VI.5.4) approximately 300 times larger than the inorganic KH<sub>2</sub>PO<sub>4</sub>, it melts at 109 °C.<sup>248</sup> Metal-free perovskites also offer the potential to overcome these challenges.

All of the above trends are also dependent on crystal structure and therefore a further understanding of how composition and structure are related is required to achieve truly targeted synthesis. In systems like these metal-free perovskites an interplay of weak forces, such as dispersion, hydrogen bonding and entropy will be important for driving structure and phase transitions, as exemplified in the hybrid halide perovskites.<sup>265,266</sup>

#### VI.4 Conclusions

Using first-principles calculations, we have demonstrated the existence of NLO activity in a number of novel metal-free perovskites. In the past, density functional theory has been shown to systematically underestimate the values of  $\chi_{ijk}^{(2)}$ . While we believe the superior quality of hybrid DFT/PBESol0-based simulations may still underestimate  $\chi^{(2)}$ , our data show that MDABCO-NH<sub>4</sub>I<sub>3</sub> and ODABCO-NH<sub>4</sub>I<sub>3</sub> both fulfil the criteria to be useful as deep-UV second-harmonic generation materials. We identify the role of the dipole moment imparted by the organic group on the A cation as an important parameter to tune the NLO properties of these materials. We apply this knowledge by introducing the cyanide CN<sup>-</sup> group on the DABCO-NH<sub>4</sub>X<sub>3</sub> structure, improving significantly the NLO properties of metal-free perovskites. Furthermore our systematic

calculations allows us to extract useful trends to chart the second-harmonic generation properties of this novel class of materials. We have shown that the material band gap, and hence the  $d_{\text{norm}}$  can be tuned by altering the halide anion. We also show the selection of the  $A$ -site cation provides an extra degree of tuning the  $\chi^{(2)}$ . By combining engineering of both the  $A$ - and  $X$ -sites we believe that these findings provide a blueprint for how to achieve high non-linear optics and second-harmonic generation activity in the desired part of the electromagnetic spectrum. We hope that these findings will help to accelerate the application of metal-free perovskites as non-toxic, earth-abundant materials for the next generation of optical communication applications.

## VI.5 Linear and non-linear optic effects

Materials respond differently to incident electromagnetic waves, whose induced electric polarization  $P$  follows:<sup>165</sup>

$$\begin{aligned} P &= \epsilon_0 \left[ \chi^{(1)} E + \chi^{(2)} E^2 + \dots + \chi^{(n)} E^n \right] \\ &= P^{(1)} + P^{(2)} + \dots + P^{(n)} \end{aligned} \quad (\text{VI.5.1})$$

where  $E$  is the electromagnetic field,  $\epsilon_0$  is the vacuum permittivity, and  $\chi^{(1)}$ ,  $\chi^{(2)}$  and  $\chi^{(n)}$  are the 1<sup>st</sup>, 2<sup>nd</sup> and  $n^{\text{th}}$  order electric susceptibilities. The dependence of the polarization on the 2<sup>nd</sup> order term ( $P^{(2)}$ ) and successive electric susceptibilities suggests that the response of a permanent dipole in non-linear optical materials assumes an anharmonic behavior once the electric dipole is perturbed by an incident electromagnetic radiation.<sup>165</sup>

Here, we assess the linear and NLO properties up to  $\chi^{(2)}$  in the static regime, and accurately derived from first-principles calculations using the coupled perturbed Kohn-Sham theory (CPKS).<sup>167,168</sup> We compute the  $n^{\text{th}}$ -order derivatives of the total energy  $E_{\text{Tot}}$  with respect to derivatives of the electric field components in  $\vec{\epsilon}_{ijk}$  ( $i, j$  and  $k$  are the direction of the electric field), which are cast in the form of order- $n + 1$  tensors. Such derivatives link to important optical descriptors, such as the electric dipole moment  $\mu_i$  and the polarisability,  $\alpha_{ij}$ ,

$$\mu_i = -\frac{\partial E_{\text{Tot.}}}{\partial \vec{\epsilon}_i}. \quad (\text{VI.5.2})$$

$$\alpha_{ij} = -\frac{\partial^2 E_{\text{Tot.}}}{\partial \vec{\epsilon}_i \partial \vec{\epsilon}_j}. \quad (\text{VI.5.3})$$

From  $\alpha_{ij}$ , the components of the dielectric tensor  $\epsilon$  are derived as  $\frac{\alpha_{ij}}{\epsilon_0 V}$  with  $\epsilon_0$  the vacuum permittivity and  $V$  the unit-cell volume. We note that  $\epsilon = n^2 = 1 + \chi^{(1)}$ , with  $n$  the refractive index. Thus,  $n$  and  $\Delta n$  (of Eq. VI.2.1) are computed directly from the dielectric tensor.

The third-order rank tensor  $\chi_{ijk}^{(2)}$  relates to 1<sup>st</sup> hyperpolarizability  $\beta_{ijk}$ .

$$\beta_{ijk} = -\frac{\partial^3 E_{\text{Tot.}}}{\partial \vec{\epsilon}_i \partial \vec{\epsilon}_j \partial \vec{\epsilon}_k}, \text{ with } \chi_{ijk}^{(2)} = \frac{2\pi \beta_{ijk}}{V}. \quad (\text{VI.5.4})$$

where  $j$  and  $k$  are the directions of the incident waves and  $i$  the direction of the SHG wave. From Eq. VI.5.1,  $\chi_{ijk}^{(2)}$  links directly to the electric field that in materials is subjected to the spatially uniform electric fields of the incident radiations, and reads as:

$$P_i^{(2)}(\omega_1 + \omega_2) = \epsilon_0 \sum_{j,k} \chi_{ijk}^{(2)} \vec{\epsilon}_j(\omega_1) \vec{\epsilon}_k(\omega_2) \quad (\text{VI.5.5})$$

where  $\chi_{ijk}^{(2)}$  is a component of the  $\chi^{(2)}$  tensor proportional to the polarization generated along the  $i$ -axis (e.g.,  $x$ ), from the  $j$  and  $k$  (e.g.,  $y$  and  $z$ ) components of the electric fields of the incident radiations oscillating at frequencies  $\omega_1$  and  $\omega_2$ , respectively. In SHG materials  $\omega_1 = \omega_2$ .

Typically,  $\chi_{ijk}^{(2)}$  is reported as  $d_{ijk} = 0.5 \chi_{ijk}^{(2)}$ . Note that for hybrid functional calculations—the choice in this study—CRYSTAL17 computes only  $\beta_{ijk}$ ,  $\chi_{ijk}^{(2)}$  and  $d_{ijk}$  values in the static limit.

## VI.6 First-principles calculations

DFT is used to investigate the structural and optical properties of the metal-free perovskites. Structure relaxations of the experimental coordinates of the metal-free perovskites was performed using the PBEsol<sup>145</sup> functional as in VASP.<sup>129,131,132</sup> The Grimme D3<sup>267</sup> correction was added to capture dispersive forces. The wave functions of the valence electrons were expanded with plane-waves with a cutoff of 520 eV, and core electrons were treated with the projector augmented wave theory.<sup>268</sup> The Brillouin-zone was integrated on a mesh with reciprocal density of 64  $k$ -points per  $\text{\AA}^{-1}$ . The total energy was converged within  $10^{-5}$  eV and forces to  $10^{-2}$  eV  $\text{\AA}^{-1}$ .

An accurate treatment of the electronic structure and in particular the assessment of the optical band gaps is crucial for the description of NLO properties.<sup>233,235,269</sup> Starting from the PBEsol-D3 structures with VASP, we re-optimized the coordinates (or volume and coordinates) with the hybrid functional PBE0Sol-D3,<sup>145,270</sup> including 25%

of exact exchange as available in CRYSTAL17.<sup>169,170</sup> We exploited the all-electron linear combination of atomic orbitals of CRYSTAL17 expanded by consistent Triple- $\zeta$  plus polarization basis-sets, see Refs. 271 and 272. Given the electronic configuration of I ( $[\text{Kr}]4d^{10}5s^25p^5$ ) a fully-relativistic pseudo-potential is used.<sup>273</sup> The total energy was converged within  $\sim 3 \times 10^{-9}$  eV and integrated over a well converged and symmetrized  $4 \times 4 \times 4$   $k$ -point mesh (i.e., the shrinking factor is set to 4). The truncation of the (infinite) Coulomb and exchange series was set by the tolerances:  $10^{-7}$ ,  $10^{-7}$ ,  $10^{-7}$ ,  $10^{-7}$  and  $10^{-30}$ . Table S1 and S2 of SI show the PBE0Sol+D3 geometries. We computed the non-linear-optical properties with these settings. The iterative solution of the CPKS equations is reached for values below  $10^{-4}$ . Table S6 shows a comparison of the performance of a number of DFT functionals.

The dipole moments of the DABCO units substituted by the organic groups were computed with Gaussian16<sup>133</sup> using the PBE0+D3<sup>270</sup> functional and the same basis-set used in the periodic calculations with CRYSTAL17.

## CHAPTER VII

### CONCLUSION

While it is clear that the superior photovoltaic performance of perovskites make them a strong contender for meeting future renewable energy demands, what remains unclear is the exact pathway that renders them suitable for the consumer market. The challenge thus remains to find a suitable pathway to increase the stability of the hybrid halide perovskite family without sacrificing efficiency.

This thesis has offered an aprotic alternative cation in Chapter III, suggesting one logical next step in addressing the moisture instability is to search for alternative aprotic cations, rather than to add additional components. As is observed with other commonly incorporated cations, utilization of an aprotic alternative leaves the electronic structure of the  $\text{PbI}_3^-$  lattice uninhibited as readily seen in the electronic band structure of  $(\text{C}_3\text{H}_3)\text{PbI}_3$  in Figure 3.2.1. It was found that when  $\text{CH}_3\text{NH}_3^+$  is exchanged for  $\text{C}_3\text{H}_3^+$ , the frontier orbital characteristics of the parent material,  $(\text{CH}_3\text{NH}_3)\text{PbI}_3$ , were maintained: a direct band gap of  $\sim 1.5$  eV as well as Pb-s/I-p valence and Pb-p conduction orbital structure. Furthermore, the phonon band structure of  $(\text{C}_3\text{H}_3)\text{PbI}_3$  (Figure 3.2.2) suggests that it is at least dynamically stable as there is a lack of imaginary phonon frequencies at the  $\Gamma$  point. It is for these reasons that any simple aprotic organic cation with correct charge and size should be an appropriate contestant for the A-site lattice position in a moisture insensitive hybrid halide perovskite.

Indeed, the electronic properties of the  $\text{PbI}_3^-$  lattice, due to its indifference towards the identity of the A-site cation, in addition to its resilience to defects, should not be effected unless the lattice is interrupted. This conclusion is directly supported by the results of Chapters IV and V, and indirectly by Chapter VI. The presence of select motifs in polymer-based passivating agents that exhibit chromophoric behavior at grain boundaries have clear charge carrier trapping effects. The injection of lone pair containing nitrogen into the carbon backbone of passivating agents gives rise to a nitrogen bound valence trap state in Figure 4.2.2. It is clear that this nitrogen trap state is the result of lone pair containing amines in the carbon backbone rather than

chain terminating ammoniums as the trap state is absent when only terminating ammoniums are present, Figure 4.2.2a and b. As such, terminating ammoniums do not give rise to the observed trap state. The size of the trap state DOS, and thus the severity of the trap state and the extent of its influence on frontier orbital properties, increases with the number of lone pair containing nitrogens. The most severe case examined occurs when the ratio becomes unity, Figure 4.2.2f. While the conduction bands of these materials are unaffected, the chromophoric trap state has an adverse effect on the effective mass of holes, increasing hole effective masses an order of magnitude higher than current champion devices. This would likely inhibit charge transport, decreasing device efficiency. As such, lone pair containing nitrogen motifs ought to be avoided in the construction of passivating agents.

The degradation of the  $\text{PbI}_3^-$  lattice to amorphous  $\text{PbI}_2$ , just like lone pair containing nitrogen in passivating agents, is detrimental for photovoltaic performance; However, not in a manner that is readily obvious. When comparing passivating agents to a degraded  $\text{PbI}_2$  lattice, the presence of  $\text{PbI}_2$  itself does not exhibit expected chromophoric behavior as there is a lack of  $\text{PbI}_2$  states within the band gap or the frontier orbitals. Rather,  $\text{PbI}_2$  injects a difficult to surmount, location dependent energy barrier depicted in Figure 5.2.1. This energy barrier creates a type 1 heterointerface between amorphous  $\text{PbI}_2$  and  $\text{CsPbI}_3$  and charge carriers require additional energy to cross the amorphous region. As a result of the energy barrier, the extent of interference amorphous  $\text{PbI}_2$  exerts on the transport properties of the pristine lattice is directly dependent on its location. If the pathway a charge carrier travels to reach its transport material coincides with a region of amorphous  $\text{PbI}_2$ , then the charge carrier must obtain additional energy to pass through the amorphous region. It is therefore unlikely the charge carrier will make it to the transport material, which will have detrimental effects on device conversion efficiency. Conversely, if regions of amorphous  $\text{PbI}_2$  exist but are not spatially coincident with charge carrier pathways, then conversion efficiency is likely unaffected. The conclusions drawn from both Chapter IV and V imply it is desirable to maintain a relatively uninterrupted  $\text{PbI}_3^-$  lattice to and from transport layers.

Upon augmentation of the B-site cation, extensive perturbations of the host electronic properties are observed. When exchanging  $\text{Pb}^{2+}$  in the  $\text{PbI}_3^-$  lattice for  $\text{NH}_4^+$ , the band gap opens to  $> 6$  eV (see Figure 6.3.1) and completely new and exotic electrical properties are observed. It is obvious that the  $\text{NH}_4\text{I}_3^{2-}$  lattice is unsuitable for

photovoltaic applications due to its insulating band gap, however, it holds promise as a nonlinear optical material. Furthermore, the nonlinear optical properties are readily tuned through both the identity of the X-site halide (through changing the band gap) as well as by controlling the strength of the A-site cation dipole. As a result, metal-free halide perovskites exhibit multilevel tuning of their nonlinear optical properties.

In summary, this thesis offers four conclusions pertinent to the photovoltaic application of hybrid halide perovskites: I) an aprotic alternative A-site cation has been suggested to fundamentally address moisture sensitivity, II) lone pair containing nitrogen motifs in passivating agents have been identified as chromophoric centers and thus negatively impact light-to-electricity conversion efficiency, III) the impact of amorphous regions of  $\text{PbI}_2$  on light-to-electricity conversion efficiency is controlled by its location, and IV) the presence of a heavy metals, such as  $\text{Pb}^{2+}$  and  $\text{Sn}^{2+}$ , as the B-site cation is required to maintain desirable photovoltaic properties. Additionally, this thesis gives two examples of utilizing novel perovskite architectures for applications beyond photovoltaics through V) careful exposure to degradation inducing environments that can be utilized to generate core@shell ( $\text{PbI}_2$ @ $\text{APbI}_3$ ) nanocrystals, useful for photoluminescent applications by exploiting the quantum confinement induced by the type 1 heterointerface between  $\text{PbI}_2$  and  $\text{APbI}_3$  lattices, and VI) exchanging the B-site cation for an organic alternative giving rise to a novel perovskite subfamily of structures that exhibit nonlinear optical properties. Conclusions I-IV suggest that not only is searching for alternative aprotic cations a logical next step, it is likely one of the safest ways to fundamentally address the moisture instability of hybrid halide perovskites while preserving desired electronic properties. Conclusions V and VI suggest that there are novel architectures for perovskites not yet discovered that could expand the list of practical perovskite device application.

## VII.1 Future Directions

It is clear from the work outlined in this thesis that there are new and exciting solutions to addressing the instabilities of hybrid halide perovskites. It has also been made clear that the chemical makeup of additive substances must be carefully designed. Lastly, the perovskite family has exotic and unexplored properties waiting to be discovered by tweaking their chemical composition. These conclusions, however, do not discount the impressive progress made by the perovskite photovoltaic community in the past decade. In fact, it is likely that future solutions utilized in enabling commercialization will be a mix of individual solutions, such as multi-protic cations alongside carefully

designed passivating agents in a 2D-3D architectural mix. Unfortunately, there is a lack of guiding designing principles when it comes to perovskite photovoltaic engineering aimed specifically at their instabilities. Of the few general guiding principles available, there are two possible outcomes when attempting to apply current A-site cation design principles to aprotic alternatives: either i) the same guiding principles apply or ii) they do not. For the former, careful verification is required for a handful of chemically diverse aprotic alternative cations to probe the generality of the principle. For the latter, a search should be launched for the aprotic alternatives that do not inhibit parent lattice properties, and upon finding a few, the efficacy of the solution as a whole should be reexamined. The results of Chapter III, however, are indicative that the general principle should hold, but verification is still recommended. Additionally, it should also be verified that, identical to the results of Chapter IV, certain motifs do not inhibit charge transport properties. For example, would an aprotic alternative cation such as trimethylamine ((CH<sub>3</sub>)<sub>3</sub>N) exhibit chromophoric behavior? Once the generality of the of current A-site cation design principles are confirmed in aprotic alternatives, and there is an absence of motif hindrance, the ability for aprotic alternatives to resist both heat and the oxidation of the lattice in the presence of O<sub>2</sub> should be investigated. The search for alternative aprotic cations that maximize light-to-electricity conversion efficiency should begin shortly after. Hopefully expanding the body of available A-site cations aids experimentalists in their quest to provide real world and tangible solutions to these current problems. The synthesis of an aprotic hybrid halide perovskite device should provide a good starting point for fundamentally addressing instabilities present.

While it is clear that the lone pair containing nitrogen motif in passivating agents leads to a chromophoric state in the frontier valence band, it is unclear whether this phenomena is exclusive to nitrogen, a general principle of pnictogens, or a general principle for any atom with lone pairs in the carbon backbone. Investigating other pnictogens, as well as other lone pair containing elements that can fit into the carbon backbone, such as O or S, should elucidate the generality of the chromophoric state. Even if passivating agents containing alternative elements (O, S, or other pnictogens) do not offer realistic solutions to addressing moisture sensitivity of hybrid halide perovskites, their influence on the electrical properties of the frontier bands could give rise to a better understanding of the general influence certain elements have on the electronic properties of hybrid halide perovskites by targeting which elements should be avoided and why. The prospect of generating general guidelines when it comes to

the chemical composition of additive solutions is in its own right exceptionally valuable. It makes the most sense to investigate individual elements and draw conclusions on their systems first to generate several independent sets of conclusions. From there, parallels between conclusions can be drawn, generating the generalized guidelines. Such guidelines could even help design moisture insensitive A-site cations, or at the very least, give hints on what compositions to avoid. As such, future computational investigation is warranted.

The results in this thesis suggest that the location of amorphous  $\text{PbI}_2$  should determine its impact on conversion efficiency. Experimentally, these findings should be verified by examining the energetic location of the frontier orbitals (relative to a pristine  $\text{PbI}_3^-$  lattice) of thin regions of amorphous and pristine  $\text{PbI}_2$  on  $\text{PbI}_3^-$  using techniques such as scanning tunneling spectroscopy/microscopy. The results should indicate whether  $\text{PbI}_2$  acts like a type 1 heterointerface suggested by Chapter V or whether  $\text{PbI}_2$  exhibits chromophoric behavior similar to lone pair containing nitrogens in Chapter IV. If  $\text{PbI}_2$  acts like a chromophore, then it becomes more important than ever to ensure absolutely no lattice degradation occurs. On the other-hand, if  $\text{PbI}_2$  acts like a type 1 heterointerface, while still detrimental for photovoltaic applications, there is potential to generate simple to synthesize quantum confined perovskite nanocrystals. Synthetic control could be utilized to encase perovskite nanoparticles in a layer of  $\text{PbI}_2$ , electronically confining charge carriers to the  $\text{APbI}_3$  core, extending carrier lifetimes. These architectures could be achieved by exposing the perovskite lattice to moisture, heat, and light/air, letting natural degradation occur in bench-top and benign synthetic conditions. Such core@shell nanoparticles could find practical applications in photoluminescence devices through simple synthetic routes.

The computational discovery of nonlinear optical properties shown by metal-free halide perovskites should prove encouraging that perovskites have a wide array of practical applications. It is now up to experimentalists to synthetically realize these structures and demonstrate their nonlinear optical properties in the real world. Furthermore, additional organic B-site cations should be examined to see if they too exhibit nonlinear optical effects or novel electronic properties of their own. The exhibition of nonlinear optical properties enabled by novel chemical composition and architecture of metal-free halide perovskites suggests that there are still yet more undiscovered novel architectures with interesting and new electronic and physical properties.

In summary, there is a need to explore additional aprotic alternative cations to find a general trend and guiding principle for fundamentally addressing the moisture sensitivity of hybrid halide perovskites. As the lone pair containing nitrogen motif has been determined to be detrimental to photovoltaic properties, further computational investigations on the generality of these findings are warranted. Experimental observations of the electronic influence  $\text{PbI}_2$  has on  $\text{APbI}_3$  lattices is necessary to fully elucidate the impact  $\text{PbI}_2$  has on photovoltaic perovskite devices. Lastly, the discovery of nonlinear optical properties enabled by metal-free halide perovskites indicates that there are yet more undiscovered interesting electronic properties in novel perovskite families and architectures that are waiting to be discovered.

## CHAPTER A

### APPENDIX

Included are tables of calculated tolerance factors for all various combinations of the  $ABX_3$  structure where A is a monocation, B is a dication, and X is a halide. A-site cations were chosen from known organic cations and elements that readily exhibit a +1 charge and have a Shannon radii<sup>173,174</sup> for the +1 state. B-site cations were chosen from elements that readily exhibit a +2 charge and have a Shannon Radii for the +2 state. The highlight color is indicative of the formed structure: distorted perovskite (yellow), cubic perovskite (green), and non-perovskite (red).

**Table A.1** Tolerance factors for ABF<sub>3</sub> perovskites. Tolerance factors were calculated using the Shannon radii.<sup>173,174</sup> Combinations that theoretically result in a distorted perovskite structure (tf < 0.8) are highlighted in yellow. Combinations that theoretically result in a cubic perovskite structure (0.8 < tf < 1.0) are highlighted in green. Combinations that theoretically do not result in a perovskite structure (tf > 1.0) are highlighted in red. A-site cation radii were chosen as the smallest coordinated single charge ion whereas the B-site cation radii were chosen as the 6-coordinate radii. Not all combinations have been synthetically realized.

		B-site cation												
		Be <sup>+2</sup>	Mg <sup>+2</sup>	Ca <sup>+2</sup>	Sr <sup>+2</sup>	Ba <sup>+2</sup>	Ti <sup>+2</sup>	V <sup>+2</sup>	Cr <sup>+2</sup>	Mn <sup>+2</sup>	Fe <sup>+2</sup>	Co <sup>+2</sup>	Ni <sup>+2</sup>	Pd <sup>+2</sup>
A-site cation	H <sup>+</sup>	0.68	0.60	0.52	0.49	0.45	0.55	0.57	0.56	0.56	0.57	0.58	0.59	0.55
	Li <sup>+</sup>	0.76	0.67	0.58	0.55	0.51	0.62	0.64	0.63	0.63	0.64	0.65	0.67	0.62
	Na <sup>+</sup>	0.92	0.81	0.70	0.66	0.61	0.75	0.78	0.76	0.76	0.77	0.79	0.80	0.75
	K <sup>+</sup>	1.07	0.94	0.82	0.77	0.71	0.87	0.90	0.89	0.88	0.90	0.92	0.94	0.87
	Rb <sup>+</sup>	1.13	0.99	0.86	0.81	0.75	0.92	0.96	0.94	0.93	0.95	0.97	0.99	0.92
	Cs <sup>+</sup>	1.19	1.04	0.91	0.85	0.79	0.97	1.01	0.99	0.98	1.00	1.02	1.04	0.97
	Fr <sup>+</sup>	1.24	1.09	0.95	0.89	0.83	1.01	1.05	1.03	1.02	1.04	1.07	1.08	1.01
	Pd <sup>+</sup>	0.76	0.67	0.58	0.55	0.51	0.62	0.64	0.63	0.63	0.64	0.65	0.67	0.62
	Cu <sup>+</sup>	0.71	0.62	0.54	0.51	0.47	0.58	0.60	0.59	0.59	0.59	0.61	0.62	0.58
	Ag <sup>+</sup>	0.79	0.70	0.61	0.57	0.53	0.65	0.67	0.66	0.65	0.66	0.68	0.69	0.65
	Au <sup>+</sup>	1.07	0.94	0.82	0.77	0.71	0.87	0.90	0.89	0.88	0.90	0.92	0.94	0.87
	Hg <sup>+</sup>	0.91	0.80	0.70	0.65	0.61	0.74	0.77	0.76	0.75	0.76	0.78	0.80	0.74
	Tl <sup>+</sup>	1.12	0.99	0.86	0.80	0.75	0.91	0.95	0.93	0.93	0.94	0.96	0.98	0.91
	NH <sub>4</sub>	1.11	0.97	0.85	0.79	0.74	0.90	0.93	0.92	0.91	0.93	0.95	0.97	0.90
	CH <sub>3</sub> NH <sub>3</sub> <sup>+</sup>	1.39	1.22	1.06	0.99	0.92	1.13	1.17	1.15	1.14	1.16	1.19	1.21	1.13
	CH(NH <sub>2</sub> ) <sub>2</sub> <sup>+</sup>	1.53	1.34	1.17	1.10	1.02	1.25	1.29	1.27	1.26	1.28	1.32	1.34	1.25
	CH <sub>3</sub> CHNH <sub>3</sub> <sup>+</sup>	1.62	1.42	1.24	1.16	1.07	1.31	1.36	1.34	1.33	1.35	1.39	1.41	1.31
C <sub>3</sub> H <sub>3</sub> <sup>+</sup>	1.39	1.22	1.06	0.99	0.92	1.13	1.17	1.15	1.14	1.16	1.19	1.21	1.13	

Table A.1 continued.

		B-site cation												
		Pt <sup>+2</sup>	Cu <sup>+2</sup>	Ag <sup>+2</sup>	Zn <sup>+2</sup>	Cd <sup>+2</sup>	Hg <sup>+2</sup>	Ge <sup>+2</sup>	Sn <sup>+2</sup>	Pb <sup>+2</sup>	Tm <sup>+2</sup>	Sm <sup>+2</sup>	Yb <sup>+2</sup>	Dy <sup>+2</sup>
A-site cation	H <sup>+</sup>	0.57	0.59	0.53	0.58	0.54	0.53	0.59	0.49	0.49	0.51	0.48	0.51	0.50
	Li <sup>+</sup>	0.64	0.66	0.60	0.66	0.60	0.60	0.66	0.55	0.55	0.58	0.54	0.57	0.57
	Na <sup>+</sup>	0.77	0.80	0.72	0.79	0.73	0.72	0.80	0.66	0.66	0.70	0.65	0.69	0.68
	K <sup>+</sup>	0.90	0.93	0.84	0.92	0.85	0.84	0.93	0.77	0.77	0.81	0.75	0.80	0.80
	Rb <sup>+</sup>	0.95	0.98	0.89	0.97	0.90	0.89	0.98	0.81	0.81	0.85	0.80	0.85	0.84
	Cs <sup>+</sup>	1.00	1.03	0.93	1.02	0.94	0.93	1.03	0.86	0.86	0.90	0.84	0.89	0.88
	Fr <sup>+</sup>	1.04	1.07	0.97	1.07	0.98	0.97	1.07	0.89	0.89	0.94	0.87	0.93	0.92
	Pd <sup>+</sup>	0.64	0.66	0.60	0.66	0.60	0.60	0.66	0.55	0.55	0.58	0.54	0.57	0.57
	Cu <sup>+</sup>	0.59	0.61	0.56	0.61	0.56	0.56	0.61	0.51	0.51	0.54	0.50	0.53	0.53
	Ag <sup>+</sup>	0.66	0.69	0.62	0.68	0.63	0.62	0.69	0.57	0.57	0.60	0.56	0.59	0.59
	Au <sup>+</sup>	0.90	0.93	0.84	0.92	0.85	0.84	0.93	0.77	0.77	0.81	0.75	0.80	0.80
	Hg <sup>+</sup>	0.76	0.79	0.72	0.79	0.72	0.72	0.79	0.66	0.66	0.69	0.64	0.68	0.68
	Tl <sup>+</sup>	0.94	0.97	0.88	0.97	0.89	0.88	0.97	0.81	0.81	0.85	0.79	0.84	0.83
	NH <sub>4</sub>	0.93	0.96	0.87	0.95	0.88	0.87	0.96	0.80	0.80	0.84	0.78	0.83	0.82
	CH <sub>3</sub> NH <sub>3</sub> <sup>+</sup>	1.16	1.20	1.09	1.19	1.10	1.09	1.20	1.00	1.00	1.05	0.98	1.04	1.03
	CH(NH <sub>2</sub> ) <sub>2</sub> <sup>+</sup>	1.28	1.32	1.20	1.32	1.21	1.20	1.32	1.10	1.10	1.16	1.08	1.15	1.14
CH <sub>3</sub> CHNH <sub>3</sub> <sup>+</sup>	1.35	1.40	1.27	1.39	1.28	1.27	1.40	1.16	1.16	1.22	1.14	1.21	1.20	
C <sub>3</sub> H <sub>3</sub> <sup>+</sup>	1.16	1.20	1.09	1.19	1.10	1.09	1.20	1.00	1.00	1.05	0.98	1.04	1.03	

**Table A.2** Tolerance factors for  $ABCl_3$  perovskites. Tolerance factors were calculated using the Shannon radii.<sup>173,174</sup> Combinations that theoretically result in a distorted perovskite structure ( $tf < 0.8$ ) are highlighted in yellow. Combinations that theoretically result in a cubic perovskite structure ( $0.8 < tf < 1.0$ ) are highlighted in green. Combinations that theoretically do not result in a perovskite structure ( $tf > 1.0$ ) are highlighted in red. A-site cation radii were chosen as the smallest coordinated single charge ion whereas the B-site cation radii were chosen as the 6-coordinate radii. Not all combinations have been synthetically realized.

		B-site cation												
		Be <sup>+2</sup>	Mg <sup>+2</sup>	Ca <sup>+2</sup>	Sr <sup>+2</sup>	Ba <sup>+2</sup>	Ti <sup>+2</sup>	V <sup>+2</sup>	Cr <sup>+2</sup>	Mn <sup>+2</sup>	Fe <sup>+2</sup>	Co <sup>+2</sup>	Ni <sup>+2</sup>	Pd <sup>+2</sup>
A-site cation	H <sup>+</sup>	0.69	0.62	0.57	0.52	0.49	0.61	0.62	0.61	0.61	0.62	0.61	0.64	0.58
	Li <sup>+</sup>	0.75	0.68	0.62	0.57	0.54	0.67	0.68	0.67	0.67	0.68	0.66	0.7	0.64
	Na <sup>+</sup>	0.88	0.80	0.73	0.67	0.63	0.78	0.79	0.78	0.78	0.80	0.77	0.82	0.74
	K <sup>+</sup>	0.99	0.91	0.82	0.76	0.71	0.89	0.90	0.89	0.89	0.91	0.88	0.93	0.84
	Rb <sup>+</sup>	1.04	0.95	0.86	0.79	0.75	0.93	0.94	0.93	0.93	0.95	0.92	0.98	0.88
	Cs <sup>+</sup>	1.09	0.99	0.90	0.83	0.78	0.97	0.98	0.97	0.97	0.99	0.96	1.02	0.92
	Fr <sup>+</sup>	1.13	1.03	0.94	0.86	0.81	1.01	1.02	1.01	1.00	1.03	1.00	1.06	0.96
	Pd <sup>+</sup>	0.75	0.68	0.62	0.57	0.54	0.67	0.68	0.67	0.67	0.68	0.66	0.70	0.64
	Cu <sup>+</sup>	0.71	0.65	0.59	0.54	0.51	0.63	0.64	0.63	0.63	0.65	0.63	0.67	0.60
	Ag <sup>+</sup>	0.78	0.71	0.64	0.59	0.55	0.69	0.70	0.69	0.69	0.71	0.69	0.73	0.66
	Au <sup>+</sup>	0.99	0.91	0.82	0.76	0.71	0.89	0.90	0.89	0.89	0.91	0.88	0.93	0.84
	Hg <sup>+</sup>	0.87	0.79	0.72	0.66	0.62	0.78	0.78	0.78	0.77	0.79	0.77	0.82	0.74
	Tl <sup>+</sup>	1.04	0.94	0.86	0.79	0.74	0.93	0.93	0.93	0.92	0.94	0.92	0.97	0.88
	NH <sub>4</sub>	1.02	0.93	0.85	0.78	0.73	0.91	0.92	0.91	0.91	0.93	0.90	0.96	0.87
	CH <sub>3</sub> NH <sub>3</sub> <sup>+</sup>	1.24	1.13	1.03	0.95	0.89	1.11	1.12	1.11	1.11	1.13	1.10	1.16	1.05
	CH(NH <sub>2</sub> ) <sub>2</sub> <sup>+</sup>	1.36	1.24	1.12	1.03	0.97	1.21	1.22	1.21	1.21	1.24	1.20	1.27	1.15
	CH <sub>3</sub> CHNH <sub>3</sub> <sup>+</sup>	1.42	1.30	1.18	1.08	1.02	1.27	1.28	1.27	1.27	1.30	1.26	1.33	1.20
C <sub>3</sub> H <sub>3</sub> <sup>+</sup>	1.24	1.13	1.03	0.95	0.89	1.11	1.12	1.11	1.11	1.13	1.10	1.16	1.05	

Table A.2 continued.

		B-site cation												
		Pt <sup>+2</sup>	Cu <sup>+2</sup>	Ag <sup>+2</sup>	Zn <sup>+2</sup>	Cd <sup>+2</sup>	Hg <sup>+2</sup>	Ge <sup>+2</sup>	Sn <sup>+2</sup>	Pb <sup>+2</sup>	Tm <sup>+2</sup>	Sm <sup>+2</sup>	Yb <sup>+2</sup>	Dy <sup>+2</sup>
A-site cation	H <sup>+</sup>	0.59	0.61	0.56	0.61	0.59	0.59	0.61	0.52	0.55	0.57	0.55	0.58	0.54
	Li <sup>+</sup>	0.65	0.67	0.62	0.67	0.64	0.64	0.67	0.57	0.61	0.62	0.60	0.64	0.59
	Na <sup>+</sup>	0.76	0.78	0.72	0.78	0.75	0.75	0.78	0.67	0.71	0.72	0.70	0.74	0.69
	K <sup>+</sup>	0.86	0.89	0.82	0.88	0.85	0.85	0.89	0.76	0.80	0.82	0.79	0.84	0.78
	Rb <sup>+</sup>	0.90	0.93	0.86	0.92	0.89	0.89	0.93	0.80	0.84	0.86	0.83	0.88	0.82
	Cs <sup>+</sup>	0.94	0.97	0.89	0.96	0.93	0.93	0.97	0.83	0.88	0.90	0.87	0.92	0.85
	Fr <sup>+</sup>	0.98	1.00	0.93	1.00	0.97	0.97	1.00	0.86	0.91	0.93	0.90	0.96	0.89
	Pd <sup>+</sup>	0.65	0.67	0.62	0.67	0.64	0.64	0.67	0.57	0.61	0.62	0.60	0.64	0.59
	Cu <sup>+</sup>	0.61	0.63	0.58	0.63	0.61	0.61	0.63	0.54	0.57	0.59	0.57	0.60	0.56
	Ag <sup>+</sup>	0.67	0.69	0.64	0.69	0.66	0.66	0.69	0.59	0.63	0.64	0.62	0.66	0.61
	Au <sup>+</sup>	0.86	0.89	0.82	0.88	0.85	0.85	0.89	0.76	0.80	0.82	0.79	0.84	0.78
	Hg <sup>+</sup>	0.75	0.77	0.71	0.77	0.74	0.74	0.77	0.66	0.70	0.72	0.69	0.74	0.68
	Tl <sup>+</sup>	0.90	0.92	0.85	0.92	0.89	0.89	0.92	0.79	0.84	0.85	0.83	0.88	0.81
	NH <sub>4</sub>	0.89	0.91	0.84	0.91	0.88	0.88	0.91	0.78	0.83	0.84	0.82	0.87	0.80
	CH <sub>3</sub> NH <sub>3</sub> <sup>+</sup>	1.08	1.11	1.02	1.10	1.06	1.06	1.11	0.95	1.00	1.02	0.99	1.05	0.97
	CH(NH <sub>2</sub> ) <sub>2</sub> <sup>+</sup>	1.18	1.21	1.12	1.20	1.16	1.16	1.21	1.04	1.10	1.12	1.08	1.15	1.07
CH <sub>3</sub> CHNH <sub>3</sub> <sup>+</sup>	1.23	1.27	1.17	1.26	1.22	1.22	1.27	1.09	1.15	1.17	1.14	1.20	1.12	
C <sub>3</sub> H <sub>3</sub> <sup>+</sup>	1.08	1.11	1.02	1.10	1.06	1.06	1.11	0.95	1.00	1.02	0.99	1.05	0.97	

**Table A.3** Tolerance factors for  $ABBr_3$  perovskites. Tolerance factors were calculated using the Shannon radii.<sup>173,174</sup> Combinations that theoretically result in a distorted perovskite structure ( $tf < 0.8$ ) are highlighted in yellow. Combinations that theoretically result in a cubic perovskite structure ( $0.8 < tf < 1.0$ ) are highlighted in green. Combinations that theoretically do not result in a perovskite structure ( $tf > 1.0$ ) are highlighted in red. A-site cation radii were chosen as the smallest coordinated single charge ion whereas the B-site cation radii were chosen as the 6-coordinate radii. Not all combinations have been synthetically realized.

		B-site cation												
		Be <sup>+2</sup>	Mg <sup>+2</sup>	Ca <sup>+2</sup>	Sr <sup>+2</sup>	Ba <sup>+2</sup>	Ti <sup>+2</sup>	V <sup>+2</sup>	Cr <sup>+2</sup>	Mn <sup>+2</sup>	Fe <sup>+2</sup>	Co <sup>+2</sup>	Ni <sup>+2</sup>	Pd <sup>+2</sup>
A-site cation	H <sup>+</sup>	0.69	0.62	0.58	0.53	0.50	0.62	0.62	0.62	0.62	0.63	0.61	0.65	0.59
	Li <sup>+</sup>	0.75	0.67	0.63	0.58	0.54	0.68	0.68	0.67	0.67	0.68	0.67	0.71	0.64
	Na <sup>+</sup>	0.87	0.78	0.73	0.67	0.63	0.78	0.79	0.78	0.78	0.79	0.77	0.82	0.74
	K <sup>+</sup>	0.98	0.88	0.82	0.75	0.71	0.89	0.89	0.88	0.88	0.89	0.87	0.93	0.83
	Rb <sup>+</sup>	1.02	0.92	0.86	0.79	0.74	0.93	0.93	0.92	0.92	0.93	0.91	0.97	0.87
	Cs <sup>+</sup>	1.07	0.96	0.89	0.82	0.78	0.96	0.97	0.96	0.96	0.97	0.95	1.01	0.91
	Fr <sup>+</sup>	1.10	0.99	0.93	0.85	0.80	1.00	1.00	0.99	0.99	1.01	0.98	1.05	0.94
	Pd <sup>+</sup>	0.75	0.67	0.63	0.58	0.54	0.68	0.68	0.67	0.67	0.68	0.67	0.71	0.64
	Cu <sup>+</sup>	0.71	0.64	0.60	0.55	0.52	0.64	0.65	0.64	0.64	0.65	0.63	0.67	0.61
	Ag <sup>+</sup>	0.77	0.69	0.65	0.60	0.56	0.70	0.70	0.69	0.69	0.70	0.69	0.73	0.66
	Au <sup>+</sup>	0.98	0.88	0.82	0.75	0.71	0.89	0.89	0.88	0.88	0.89	0.87	0.93	0.83
	Hg <sup>+</sup>	0.86	0.77	0.72	0.66	0.63	0.78	0.78	0.77	0.77	0.78	0.77	0.82	0.73
	Tl <sup>+</sup>	1.02	0.91	0.85	0.78	0.74	0.92	0.92	0.91	0.91	0.93	0.90	0.96	0.87
	NH <sub>4</sub>	1.00	0.90	0.84	0.78	0.73	0.91	0.91	0.90	0.90	0.92	0.89	0.95	0.86
	CH <sub>3</sub> NH <sub>3</sub> <sup>+</sup>	1.21	1.09	1.02	0.93	0.88	1.10	1.10	1.09	1.09	1.10	1.08	1.15	1.03
	CH(NH <sub>2</sub> ) <sub>2</sub> <sup>+</sup>	1.32	1.18	1.11	1.02	0.96	1.19	1.20	1.18	1.18	1.20	1.17	1.25	1.13
	CH <sub>3</sub> CHNH <sub>3</sub> <sup>+</sup>	1.38	1.24	1.16	1.07	1.00	1.25	1.25	1.24	1.24	1.26	1.23	1.31	1.18
C <sub>3</sub> H <sub>3</sub> <sup>+</sup>	1.21	1.09	1.02	0.93	0.88	1.10	1.10	1.09	1.09	1.10	1.08	1.15	1.03	

Table A.3 continued.

		B-site cation												
		Pt <sup>+2</sup>	Cu <sup>+2</sup>	Ag <sup>+2</sup>	Zn <sup>+2</sup>	Cd <sup>+2</sup>	Hg <sup>+2</sup>	Ge <sup>+2</sup>	Sn <sup>+2</sup>	Pb <sup>+2</sup>	Tm <sup>+2</sup>	Sm <sup>+2</sup>	Yb <sup>+2</sup>	Dy <sup>+2</sup>
A-site cation	H <sup>+</sup>	0.60	0.62	0.57	0.61	0.61	0.61	0.62	0.53	0.56	0.55	0.59	0.60	0.56
	Li <sup>+</sup>	0.65	0.67	0.62	0.67	0.66	0.66	0.67	0.58	0.61	0.60	0.64	0.65	0.61
	Na <sup>+</sup>	0.76	0.78	0.72	0.77	0.77	0.77	0.78	0.67	0.71	0.70	0.74	0.76	0.70
	K <sup>+</sup>	0.85	0.88	0.81	0.87	0.87	0.87	0.88	0.76	0.80	0.79	0.83	0.85	0.79
	Rb <sup>+</sup>	0.89	0.91	0.85	0.91	0.90	0.90	0.91	0.79	0.84	0.82	0.87	0.89	0.83
	Cs <sup>+</sup>	0.93	0.95	0.89	0.95	0.94	0.94	0.95	0.83	0.87	0.86	0.91	0.93	0.86
	Fr <sup>+</sup>	0.96	0.99	0.92	0.98	0.98	0.98	0.99	0.85	0.90	0.89	0.94	0.96	0.90
	Pd <sup>+</sup>	0.65	0.67	0.62	0.67	0.66	0.66	0.67	0.58	0.61	0.60	0.64	0.65	0.61
	Cu <sup>+</sup>	0.62	0.64	0.59	0.63	0.63	0.63	0.64	0.55	0.58	0.57	0.61	0.62	0.58
	Ag <sup>+</sup>	0.67	0.69	0.64	0.69	0.68	0.68	0.69	0.60	0.63	0.62	0.66	0.67	0.63
	Au <sup>+</sup>	0.85	0.88	0.81	0.87	0.87	0.87	0.88	0.76	0.80	0.79	0.83	0.85	0.79
	Hg <sup>+</sup>	0.75	0.77	0.71	0.77	0.76	0.76	0.77	0.67	0.70	0.69	0.73	0.75	0.70
	Tl <sup>+</sup>	0.89	0.91	0.84	0.91	0.90	0.90	0.91	0.79	0.83	0.82	0.87	0.89	0.82
	NH <sub>4</sub>	0.88	0.90	0.83	0.90	0.89	0.89	0.90	0.78	0.82	0.81	0.86	0.88	0.81
	CH <sub>3</sub> NH <sub>3</sub> <sup>+</sup>	1.06	1.08	1.00	1.08	1.07	1.07	1.08	0.94	0.99	0.97	1.03	1.06	0.98
	CH(NH <sub>2</sub> ) <sub>2</sub> <sup>+</sup>	1.15	1.18	1.09	1.18	1.17	1.17	1.18	1.02	1.08	1.06	1.13	1.15	1.07
CH <sub>3</sub> CHNH <sub>3</sub> <sup>+</sup>	1.20	1.24	1.15	1.23	1.22	1.22	1.24	1.07	1.13	1.11	1.18	1.20	1.12	
C <sub>3</sub> H <sub>3</sub> <sup>+</sup>	1.06	1.08	1.00	1.08	1.07	1.07	1.08	0.94	0.99	0.97	1.03	1.06	0.98	

**Table A.4** Tolerance factors for  $ABl_3$  perovskites. Tolerance factors were calculated using the Shannon radii.<sup>173,174</sup> Combinations that theoretically result in a distorted perovskite structure ( $tf < 0.8$ ) are highlighted in yellow. Combinations that theoretically result in a cubic perovskite structure ( $0.8 < tf < 1.0$ ) are highlighted in green. Combinations that theoretically do not result in a perovskite structure ( $tf > 1.0$ ) are highlighted in red. A-site cation radii were chosen as the smallest coordinated single charge ion whereas the B-site cation radii were chosen as the 6-coordinate radii. Not all combinations have been synthetically realized.

		B-site cation												
		Be <sup>+2</sup>	Mg <sup>+2</sup>	Ca <sup>+2</sup>	Sr <sup>+2</sup>	Ba <sup>+2</sup>	Ti <sup>+2</sup>	V <sup>+2</sup>	Cr <sup>+2</sup>	Mn <sup>+2</sup>	Fe <sup>+2</sup>	Co <sup>+2</sup>	Ni <sup>+2</sup>	Pd <sup>+2</sup>
A-site cation	H <sup>+</sup>	0.69	0.62	0.58	0.54	0.51	0.64	0.63	0.63	0.62	0.63	0.62	0.66	0.60
	Li <sup>+</sup>	0.74	0.67	0.63	0.58	0.56	0.69	0.69	0.69	0.68	0.69	0.67	0.71	0.64
	Na <sup>+</sup>	0.85	0.76	0.72	0.67	0.64	0.79	0.78	0.78	0.77	0.78	0.77	0.81	0.74
	K <sup>+</sup>	0.95	0.86	0.81	0.75	0.71	0.88	0.88	0.88	0.86	0.88	0.86	0.91	0.82
	Rb <sup>+</sup>	0.99	0.89	0.84	0.78	0.74	0.92	0.91	0.91	0.90	0.91	0.89	0.95	0.86
	Cs <sup>+</sup>	1.03	0.93	0.88	0.81	0.77	0.96	0.95	0.95	0.94	0.95	0.93	0.99	0.89
	Fr <sup>+</sup>	1.07	0.96	0.91	0.84	0.80	0.99	0.98	0.98	0.97	0.98	0.96	1.02	0.92
	Pd <sup>+</sup>	0.74	0.67	0.63	0.58	0.56	0.69	0.69	0.69	0.68	0.69	0.67	0.71	0.64
	Cu <sup>+</sup>	0.71	0.64	0.60	0.56	0.53	0.66	0.65	0.65	0.64	0.65	0.64	0.68	0.61
	Ag <sup>+</sup>	0.77	0.69	0.65	0.60	0.57	0.71	0.70	0.70	0.69	0.70	0.69	0.73	0.66
	Au <sup>+</sup>	0.95	0.86	0.81	0.75	0.71	0.88	0.88	0.88	0.86	0.88	0.86	0.91	0.82
	Hg <sup>+</sup>	0.85	0.76	0.72	0.66	0.63	0.78	0.78	0.78	0.77	0.78	0.76	0.81	0.73
	Tl <sup>+</sup>	0.99	0.89	0.84	0.77	0.74	0.91	0.91	0.91	0.90	0.91	0.89	0.94	0.85
	NH <sub>4</sub>	0.98	0.88	0.83	0.77	0.73	0.90	0.90	0.90	0.89	0.90	0.88	0.93	0.85
	CH <sub>3</sub> NH <sub>3</sub> <sup>+</sup>	1.16	1.05	0.99	0.91	0.87	1.08	1.07	1.07	1.06	1.07	1.05	1.11	1.01
	CH(NH <sub>2</sub> ) <sub>2</sub> <sup>+</sup>	1.26	1.13	1.07	0.99	0.94	1.17	1.16	1.16	1.15	1.16	1.14	1.21	1.09
	CH <sub>3</sub> CHNH <sub>3</sub> <sup>+</sup>	1.32	1.18	1.12	1.03	0.98	1.22	1.21	1.21	1.20	1.21	1.19	1.26	1.14
C <sub>3</sub> H <sub>3</sub> <sup>+</sup>	1.16	1.05	0.99	0.91	0.87	1.08	1.07	1.07	1.06	1.07	1.05	1.11	1.01	

Table A.4 continued.

		B-site cation												
		Pt <sup>+2</sup>	Cu <sup>+2</sup>	Ag <sup>+2</sup>	Zn <sup>+2</sup>	Cd <sup>+2</sup>	Hg <sup>+2</sup>	Ge <sup>+2</sup>	Sn <sup>+2</sup>	Pb <sup>+2</sup>	Tm <sup>+2</sup>	Sm <sup>+2</sup>	Yb <sup>+2</sup>	Dy <sup>+2</sup>
A-site cation	H <sup>+</sup>	0.61	0.62	0.58	0.62	0.65	0.65	0.61	0.58	0.56	0.58	0.55	0.58	0.58
	Li <sup>+</sup>	0.66	0.67	0.63	0.67	0.70	0.70	0.66	0.62	0.61	0.63	0.60	0.63	0.62
	Na <sup>+</sup>	0.75	0.77	0.72	0.77	0.80	0.80	0.76	0.71	0.70	0.72	0.68	0.72	0.71
	K <sup>+</sup>	0.84	0.86	0.80	0.86	0.90	0.90	0.85	0.80	0.78	0.80	0.76	0.81	0.80
	Rb <sup>+</sup>	0.88	0.90	0.84	0.89	0.94	0.94	0.89	0.83	0.81	0.84	0.79	0.84	0.83
	Cs <sup>+</sup>	0.91	0.93	0.87	0.93	0.97	0.97	0.92	0.86	0.85	0.87	0.83	0.87	0.86
	Fr <sup>+</sup>	0.94	0.97	0.90	0.96	1.01	1.01	0.95	0.89	0.88	0.90	0.85	0.90	0.89
	Pd <sup>+</sup>	0.66	0.67	0.63	0.67	0.70	0.70	0.66	0.62	0.61	0.63	0.60	0.63	0.62
	Cu <sup>+</sup>	0.63	0.64	0.60	0.64	0.67	0.67	0.63	0.59	0.58	0.60	0.57	0.60	0.59
	Ag <sup>+</sup>	0.68	0.69	0.65	0.69	0.72	0.72	0.68	0.64	0.63	0.64	0.61	0.65	0.64
	Au <sup>+</sup>	0.84	0.86	0.80	0.86	0.90	0.90	0.85	0.80	0.78	0.80	0.76	0.81	0.80
	Hg <sup>+</sup>	0.75	0.77	0.71	0.76	0.80	0.80	0.75	0.71	0.69	0.71	0.68	0.72	0.71
	Tl <sup>+</sup>	0.87	0.89	0.83	0.89	0.93	0.93	0.88	0.83	0.81	0.83	0.79	0.84	0.83
	NH <sub>4</sub>	0.86	0.88	0.82	0.88	0.92	0.92	0.87	0.82	0.80	0.82	0.78	0.83	0.82
	CH <sub>3</sub> NH <sub>3</sub> <sup>+</sup>	1.03	1.05	0.98	1.05	1.10	1.10	1.04	0.97	0.95	0.98	0.93	0.98	0.97
	CH(NH <sub>2</sub> ) <sub>2</sub> <sup>+</sup>	1.11	1.14	1.07	1.14	1.19	1.19	1.13	1.06	1.04	1.06	1.01	1.07	1.06
CH <sub>3</sub> CHNH <sub>3</sub> <sup>+</sup>	1.16	1.19	1.11	1.19	1.24	1.24	1.18	1.10	1.08	1.11	1.06	1.12	1.10	
C <sub>3</sub> H <sub>3</sub> <sup>+</sup>	1.03	1.05	0.98	1.05	1.10	1.10	1.04	0.97	0.95	0.98	0.93	0.98	0.97	

## REFERENCES CITED

- [1] M. R. Allen, O. P. Dube, W. Solecki, F. Aragón-Durand, W. Cramer, S. Humphreys, M. Kainuma, J. Kala, N. Mahowald, Y. Mulugetta, R. Perez, M. Wairiu, K. Zickfeld, P. Dasgupta, H. Eakin, B. Hayward, D. Liverman, R. Millar, G. Raga, A. Ribes, M. Richardson, M. Rojas, R. Séférian, S. I. Seneviratne, C. Smith, W. Steffen and P. Thorne, *IPCC special report*, 2018, 49.
- [2] *When Fossil Fuels Run Out, What Then?*,  
<https://mahb.stanford.edu/library-item/fossil-fuels-run/>,  
Library Catalog: mahb.stanford.edu.
- [3] J. Tsao, N. Lewis and G. Crabtree, *Solar FAQs*, 2006.
- [4] NREL, *Solar Energy Basics*,  
<https://www.nrel.gov/research/re-solar.html>, Library Catalog:  
www.nrel.gov.
- [5] P. Hersch and K. Zweibel, *Basic Photovoltaic Principles and Methods*, NREL, 1982.
- [6] W. Shockley and H. J. Queisser, *J. Appl. Phys.*, 1961, **32**, 510.
- [7] W. Smith, *Nature*, 1873, **7**, 303.
- [8] H. Hertz, *Ann. Phys.*, 1887, **267**, 983.
- [9] E. Becquerel, *Comptes Rendus.*, 1839, **9**, 561.
- [10] *A Brief History of Solar Panels*, 2019,  
<https://www.smithsonianmag.com/sponsored/brief-history-solar-panels-180972006/>, Library Catalog: www.smithsonianmag.com  
Section: Articles, Innovation, Energy, Sponsored.
- [11] D. M. Chapin, C. S. Fuller and G. L. Pearson, *J. Appl. Phys.*, 1954, **25**, 676.
- [12] NREL, *Best Research-Cell Efficiency Chart Photovoltaic Research NREL*, 2019,  
<https://www.nrel.gov/pv/cell-efficiency.html>.

- [13] J. Zhao, A. Wang and M. A. Green, *Prog. Photovolt.*, 1999, **7**, 471.
- [14] M. A. Green, *Prog. Photovolt.*, 2009, **17**, 183.
- [15] K. Masuko, M. Shigematsu, T. Hashiguchi, D. Fujishima, M. Kai, N. Yoshimura, T. Yamaguchi, Y. Ichihashi, T. Mishima, N. Matsubara, T. Yamanishi, T. Takahama, M. Taguchi, E. Maruyama and S. Okamoto, *IEEE J. Photovolt.*, 2014, **4**, 1433.
- [16] D. D. Smith, P. Cousins, S. Westerberg, R. D. Jesus-Tabajonda, G. Aniero and Y.-C. Shen, *IEEE J. Photovolt.*, 2014, **4**, 1465.
- [17] E. Płaczek-Popko, *Opto-Electron. Rev.*, 2017, **25**, 55.
- [18] H. Sai, T. Matsui and K. Matsubara, *Appl. Phys. Lett.*, 2016, **109**, 183506.
- [19] T. D. Lee and A. U. Ebong, *Renew. Sustain. Energy Rev.*, 2017, **70**, 1286.
- [20] *Efficiency record isn't the biggest change for Alta Devices' GaAs solar technology*, <https://www.pv-magazine.com/2018/12/17/efficiency-record-isnt-the-biggest-change-for-alta-devices-gaas-solar-technology/>, Library Catalog: [www.pv-magazine.com](http://www.pv-magazine.com).
- [21] K. S. Jefferies, *Analysis of Costs of Gallium Arsenide and Silicon Solar Arrays for Space Power Applications*, NASA Technical Report NASA-TP-1811 19810011645, 1981.
- [22] *Topaz Solar Farm*, <http://www.firstsolar.com/Resources/Projects/TopazSolarFarm>, Library Catalog: [www.firstsolar.com](http://www.firstsolar.com).
- [23] *Topaz Solar Farm, California*, 2015, <https://earthobservatory.nasa.gov/images/85403/topaz-solar-farm-california>, Library Catalog: [earthobservatory.nasa.gov](http://earthobservatory.nasa.gov)  
Publisher: NASA Earth Observatory.
- [24] *ATSDR - Toxicological Profile: Cadmium*, 2012, <https://www.atsdr.cdc.gov/ToxProfiles/tp.asp?id=48&tid=15>, Library Catalog: [www.atsdr.cdc.gov](http://www.atsdr.cdc.gov).
- [25] *Cadmium Telluride Solar Cells*, <https://www.nrel.gov/pv/cadmium-telluride-solar-cells.html>, Library Catalog: [www.nrel.gov](http://www.nrel.gov).

- [26] *Solar Frontier Achieves World Record Thin-Film Solar Cell Efficiency of 23.35%*, 2019, [http://www.solar-frontier.com/eng/news/2019/0117\\_press.html](http://www.solar-frontier.com/eng/news/2019/0117_press.html).
- [27] B. O'Regan and M. Grätzel, *Nature*, 1991, **353**, 737.
- [28] A. Hagfeldt, G. Boschloo, L. Sun, L. Kloo and H. Pettersson, *Chem. Rev.*, 2010, **110**, 6595.
- [29] M.-E. Ragoussi and T. Torres, *Chem. Commun.*, 2015, **51**, 3957.
- [30] Z. Pan, H. Rao, I. Mora-Seró, J. Bisquert and X. Zhong, *Chem. Soc. Rev.*, 2018, **47**, 7659.
- [31] M. Hao, Y. Bai, S. Zeiske, L. Ren, J. Liu, Y. Yuan, N. Zarrabi, N. Cheng, M. Ghasemi, P. Chen, M. Lyu, D. He, J.-H. Yun, Y. Du, Y. Wang, S. Ding, A. Armin, P. Meredith, G. Liu, H.-M. Cheng and L. Wang, *Nat. Energy*, 2020, **5**, 79.
- [32] W. Wang, M. T. Winkler, O. Gunawan, T. Gokmen, T. K. Todorov, Y. Zhu and D. B. Mitzi, *Adv. Energy Mater.*, 2014, **4**, 1301465.
- [33] K. Pal, P. Singh, A. Bhaduri and K. B. Thapa, *Sol. Energy Mater. Sol. Cells*, 2019, **196**, 138.
- [34] A. Kojima, K. Teshima, Y. Shirai and T. Miyasaka, *J. Am. Chem. Soc.*, 2009, **131**, 6050.
- [35] *Perovskite Mineral Data*,  
<http://webmineral.com/data/Perovskite.shtml#.XvZz05NKgYw>.
- [36] H. L. Wells, *Am. J. Sci.*, 1893, **45**, 121.
- [37] A. K. Jena, A. Kulkarni and T. Miyasaka, *Chem. Rev.*, 2019, **119**, 3036.
- [38] S. D. Stranks, G. E. Eperon, G. Grancini, C. Menelaou, M. J. P. Alcocer, T. Leijtens, L. M. Herz, A. Petrozza and H. J. Snaith, *Science*, 2013, **342**, 341.
- [39] C. Wehrenfennig, G. E. Eperon, M. B. Johnston, H. J. Snaith and L. M. Herz, *Adv. Mater.*, 2014, **26**, 1584.
- [40] Q. Dong, Y. Fang, Y. Shao, P. Mulligan, J. Qiu, L. Cao and J. Huang, *Science*, 2015, **347**, 967.

- [41] J. Liang, C. Wang, Y. Wang, Z. Xu, Z. Lu, Y. Ma, H. Zhu, Y. Hu, C. Xiao, X. Yi, G. Zhu, H. Lv, L. Ma, T. Chen, Z. Tie, Z. Jin and J. Liu, *J. Am. Chem. Soc.*, 2016, **138**, 15829.
- [42] G. E. Eperon, G. M. Paternó, R. J. Sutton, A. Zampetti, A. A. Haghighirad, F. Cacialli and H. J. Snaith, *J. Mater. Chem. A*, 2015, **3**, 19688.
- [43] C. Liu, W. Li, C. Zhang, Y. Ma, J. Fan and Y. Mai, *J. Am. Chem. Soc.*, 2018, **140**, 3825.
- [44] M. M. Lee, J. Teuscher, T. Miyasaka, T. N. Murakami and H. J. Snaith, *Science*, 2012, **338**, 643.
- [45] Y. Zong, Y. Zhou, M. Ju, H. F. Garces, A. R. Krause, F. Ji, G. Cui, X. C. Zeng, N. P. Padture and S. Pang, *Angew. Chem. Int. Ed.*, 2016, **55**, 14723.
- [46] C. C. Stoumpos, L. Frazer, D. J. Clark, Y. S. Kim, S. H. Rhim, A. J. Freeman, J. B. Ketterson, J. I. Jang and M. G. Kanatzidis, *J. Am. Chem. Soc.*, 2015, **137**, 6804.
- [47] N. De Marco, H. Zhou, Q. Chen, P. Sun, Z. Liu, L. Meng, E.-P. Yao, Y. Liu, A. Schiffer and Y. Yang, *Nano Lett.*, 2016, **16**, 1009.
- [48] M. Saliba, T. Matsui, K. Domanski, J.-Y. Seo, A. Ummadisingu, S. M. Zakeeruddin, J.-P. Correa-Baena, W. R. Tress, A. Abate, A. Hagfeldt and M. Grätzel, *Science*, 2016, **354**, 206.
- [49] H. Tsai, R. Asadpour, J.-C. Blancon, C. C. Stoumpos, O. Durand, J. W. Strzalka, B. Chen, R. Verduzco, P. M. Ajayan, S. Tretiak, J. Even, M. A. Alam, M. G. Kanatzidis, W. Nie and A. D. Mohite, *Science*, 2018, **360**, 67.
- [50] B. Charles, M. T. Weller, S. Rieger, L. E. Hatcher, P. F. Henry, J. Feldmann, D. Wolverson and C. C. Wilson, *Chem. Mater.*, 2020, **32**, 2282.
- [51] E. Nakanishi, R. Nishikubo, A. Wakamiya and A. Saeki, *J. Phys. Chem. Lett.*, 2020, 4043.
- [52] J. J. He, Z. R. Zhou, Z. Q. Lin, B. Ge, H. W. Qiao, Y. Hou, S. Yang and H. G. Yang, *ACS Appl. Energy Mater.*, 2020, 4121.
- [53] G. E. Eperon, S. D. Stranks, C. Menelaou, M. B. Johnston, L. M. Herz and H. J. Snaith, *Energy Environ. Sci.*, 2014, **7**, 982.

- [54] F. Brivio, A. B. Walker and A. Walsh, *APL Mater.*, 2013, **1**, 042111.
- [55] T. W. Kasel, A. T. Murray and C. H. Hendon, *J. Phys. Chem. C*, 2018, **122**, 2041.
- [56] T. W. Kasel and C. H. Hendon, *J. Mater. Chem. C*, 2018, **6**, 4765.
- [57] M. C. Brennan, S. Toso, I. M. Pavlovets, M. Zhukovskiy, S. Marras, M. Kuno, L. Manna and D. Baranov, *ACS Energy Lett.*, 2020, **5**, 1465.
- [58] N. Rybin, D. Ghosh, J. Tisdale, S. Shrestha, M. Yoho, D. Vo, J. Even, C. Katan, W. Nie, A. J. Neukirch and S. Tretiak, *Chem. Mater.*, 2020, **32**, 1854.
- [59] F. Li, Y. Xie, Y. Hu, M. Long, Y. Zhang, J. Xu, M. Qin, X. Lu and M. Liu, *ACS Energy Lett.*, 2020, **5**, 1422.
- [60] Z. Yang, X. Zhang, W. Yang, G. E. Eperon and D. S. Ginger, *Chem. Mater.*, 2020, **32**, 2782.
- [61] Z. Zhao, F. Gu, Y. Li, W. Sun, S. Ye, H. Rao, Z. Liu, Z. Bian and C. Huang, *Adv. Sci.*, 2017, **4**, 1700204.
- [62] L. Protesescu, S. Yakunin, M. I. Bodnarchuk, F. Krieg, R. Caputo, C. H. Hendon, R. X. Yang, A. Walsh and M. V. Kovalenko, *Nano Lett.*, 2015, **15**, 3692.
- [63] A. Amat, E. Mosconi, E. Ronca, C. Quarti, P. Umari, M. K. Nazeeruddin, M. Grätzel and F. De Angelis, *Nano Lett.*, 2014, **14**, 3608.
- [64] M. A. Green, A. Ho-Baillie and H. J. Snaith, *Nat. Photonics*, 2014, **8**, 506.
- [65] S. Sun, T. Salim, N. Mathews, M. Duchamp, C. Boothroyd, G. Xing, T. C. Sum and Y. M. Lam, *Energy Environ. Sci.*, 2013, **7**, 399.
- [66] G. Barbose, N. Darghouth, S. Elmallah, S. Forrester, K. LaCommare, D. Millstein, J. Rand, W. Cotton, S. Sherwood and E. O'Shaughnessy, *Tracking the Sun: Pricing and Design Trends for Distributed Photovoltaic Systems in the United States*, Lawrence Berkeley National Laboratory, 2019.
- [67] G. Giorgi, J.-I. Fujisawa, H. Segawa and K. Yamashita, *J. Phys. Chem. Lett.*, 2013, **4**, 4213.
- [68] J. Even, L. Pedesseau and C. Katan, *J. Phys. Chem. C*, 2014, **118**, 11566.
- [69] D. W. de Quilettes, S. M. Vorpahl, S. D. Stranks, H. Nagaoka, G. E. Eperon, M. E. Ziffer, H. J. Snaith and D. S. Ginger, *Science*, 2015, **348**, 683.

- [70] J.-H. Im, I.-H. Jang, N. Pellet, M. Grätzel and N.-G. Park, *Nat. Nanotechnol.*, 2014, **9**, 927.
- [71] Y. Wu, D. Yan, J. Peng, T. Duong, Y. Wan, P. Phang, H. Shen, N. Wu, C. Barugkin, X. Fu, S. Surve, D. Walter, T. White, K. Catchpole and K. Weber, *Energy Environ. Sci.*, 2017, **11**, 2472.
- [72] F. Zheng, L. Z. Tan, S. Liu and A. M. Rappe, *Nano Lett.*, 2015, **15**, 7794.
- [73] J. Yin, P. Maity, L. Xu, A. M. El-Zohry, H. Li, O. M. Bakr, J.-L. Brédas and O. F. Mohammed, *Chem. Mater.*, 2018, **30**, 8538.
- [74] K. Frohna, T. Deshpande, J. Harter, W. Peng, B. A. Barker, J. B. Neaton, S. G. Louie, O. M. Bakr, D. Hsieh and M. Bernardi, *Nat Commun.*, 2018, **9**, 1.
- [75] K. Miyano, N. Tripathi, M. Yanagida and Y. Shirai, *Acc. Chem. Res.*, 2016, **49**, 303.
- [76] W.-J. Yin, T. Shi and Y. Yan, *Appl. Phys. Lett.*, 2014, **104**, 063903.
- [77] J. Haruyama, K. Sodeyama, L. Han and Y. Tateyama, *J. Phys. Chem. Lett.*, 2014, **5**, 2903.
- [78] Q. Wang, Y. Shao, H. Xie, L. Lyu, X. Liu, Y. Gao and J. Huang, *Appl. Phys. Lett.*, 2014, **105**, 163508.
- [79] B. Dou, J. B. Whitaker, K. Bruening, D. T. Moore, L. M. Wheeler, J. Ryter, N. J. Breslin, J. J. Berry, S. M. Garner, F. S. Barnes, S. E. Shaheen, C. J. Tassone, K. Zhu and M. F. A. M. van Hest, *ACS Energy Lett.*, 2018, **3**, 2558.
- [80] J. Shamsi, A. S. Urban, M. Imran, L. De Trizio and L. Manna, *Chem. Rev.*, 2019, **119**, 3296.
- [81] W. A. Dunlap-Shohl, Y. Zhou, N. P. Padture and D. B. Mitzi, *Chem. Rev.*, 2019, **119**, 3193.
- [82] S. D. Stranks and H. J. Snaith, *Nat. Nanotechnol.*, 2015, **10**, 391.
- [83] B. Yang, J. Chen, F. Hong, X. Mao, K. Zheng, S. Yang, Y. Li, T. Pullerits, W. Deng and K. Han, *Angew. Chem. Int. Ed.*, 2017, **56**, 12471.
- [84] P. Cheng, T. Wu, J. Zhang, Y. Li, J. Liu, L. Jiang, X. Mao, R.-F. Lu, W.-Q. Deng and K. Han, *J. Phys. Chem. Lett.*, 2017, **8**, 4402.

- [85] M. Pantaler, K. T. Cho, V. I. E. Queloz, I. García Benito, C. Fettkenhauer, I. Anusca, M. K. Nazeeruddin, D. C. Lupascu and G. Grancini, *ACS Energy Lett.*, 2018, **3**, 1781.
- [86] J. Huang, T. Lei, M. Siron, Y. Zhang, S. Yu, F. Seeler, A. Dehestani, L. N. Quan, K. Schierle-Arndt and P. Yang, *Nano Lett.*, 2020, 3734.
- [87] F. Hao, C. C. Stoumpos, D. H. Cao, R. P. H. Chang and M. G. Kanatzidis, *Nat. Photonics*, 2014, **8**, 489.
- [88] M. E. Kayesh, T. H. Chowdhury, K. Matsuishi, R. Kaneko, S. Kazaoui, J.-J. Lee, T. Noda and A. Islam, *ACS Energy Lett.*, 2018, **3**, 1584.
- [89] C.-M. Tsai, Y.-P. Lin, M. K. Pola, S. Narra, E. Jokar, Y.-W. Yang and E. W.-G. Diau, *ACS Energy Lett.*, 2018, **3**, 2077.
- [90] R. Kashikar, M. Gupta and B. R. K. Nanda, *Phys. Rev. B*, 2020, **101**, 155102.
- [91] T. Wang, Q. Tai, X. Guo, J. Cao, C.-K. Liu, N. Wang, D. Shen, Y. Zhu, C.-S. Lee and F. Yan, *ACS Energy Lett.*, 2020, 1741.
- [92] N. Aristidou, I. Sanchez-Molina, T. Chotchuangchutchaval, M. Brown, L. Martinez, T. Rath and S. A. Haque, *Angew. Chem. Int. Ed.*, 2015, **54**, 8208.
- [93] N. Aristidou, C. Eames, I. Sanchez-Molina, X. Bu, J. Kosco, M. S. Islam and S. A. Haque, *Nat. Commun.*, 2017, **8**, 1.
- [94] E. J. Juárez-Pérez, Z. Hawash, S. Ruiz Raga, L. Ono and Y. Qi, *Energy Environ. Sci.*, 2016, **9**, 3406.
- [95] B. Conings, J. Drikkoningen, N. Gauquelin, A. Babayigit, J. D'Haen, L. D'Olieslaeger, A. Ethirajan, J. Verbeeck, J. Manca, E. Mosconi, F. D. Angelis and H.-G. Boyen, *Adv. Energy Mater.*, 2015, **5**, 1500477.
- [96] Z. Song, A. Abate, S. C. Watthage, G. K. Liyanage, A. B. Phillips, U. Steiner, M. Graetzel and M. J. Heben, *Adv. Energy Mater.*, 2016, **6**, 1600846.
- [97] E. Mosconi, J. M. Azpiroz and F. De Angelis, *Chem. Mater.*, 2015, **27**, 4885.
- [98] A. Dualeh, P. Gao, S. I. Seok, M. K. Nazeeruddin and M. Gätzel, *Chem. Mater.*, 2014, **26**, 6160.
- [99] Q. Sun and W.-J. Yin, *J. Am. Chem. Soc.*, 2017, **139**, 14905.

- [100] J. M. Frost, K. T. Butler, F. Brivio, C. H. Hendon, M. van Schilfgaarde and A. Walsh, *Nano Lett.*, 2014, **14**, 2584.
- [101] E. L. da Silva, J. M. Skelton, S. C. Parker and A. Walsh, *Phys. Rev. B*, 2015, **91**, 144107.
- [102] E. L. Unger, E. T. Hoke, C. D. Bailie, W. H. Nguyen, A. R. Bowring, T. Heumüller, M. G. Christoforo and M. D. McGehee, *Energy Environ. Sci.*, 2014, **7**, 3690.
- [103] H. J. Snaith, A. Abate, J. M. Ball, G. E. Eperon, T. Leijtens, N. K. Noel, S. D. Stranks, J. T.-W. Wang, K. Wojciechowski and W. Zhang, *J. Phys. Chem. Lett.*, 2014, **5**, 1511.
- [104] J. M. Frost, K. T. Butler and A. Walsh, *APL Mater.*, 2014, **2**, 081506.
- [105] L. M. Garten, D. T. Moore, S. U. Nanayakkara, S. Dwaraknath, P. Schulz, J. Wands, A. Rockett, B. Newell, K. A. Persson, S. Trolrier-McKinstry and D. S. Ginley, *Sci. Adv.*, 2019, **5**, eaas9311.
- [106] I. Hwang, I. Jeong, J. Lee, M. J. Ko and K. Yong, *ACS Appl. Mater. Interfaces*, 2015, **7**, 17330.
- [107] Y. Wu, F. Xie, H. Chen, X. Yang, H. Su, M. Cai, Z. Zhou, T. Noda and L. Han, *Adv. Mater.*, 2017, **29**, 1701073.
- [108] L. Zuo, H. Guo, D. W. deQuilettes, S. Jariwala, N. D. Marco, S. Dong, R. DeBlock, D. S. Ginger, B. Dunn, M. Wang and Y. Yang, *Sci. Adv.*, 2017, **3**, 1700106.
- [109] J. Rodríguez-Romero, J. Sanchez-Diaz, C. Echeverría-Arrondo, S. Masi, D. Esparza, E. M. Barea and I. Mora-Seró, *ACS Energy Lett.*, 2020, **5**, 1013.
- [110] B. Kim and S. I. Seok, *Energy Environ. Sci.*, 2020, **13**, 805.
- [111] S. Kundu and T. L. Kelly, *EcoMat*, 2020, **2**, e12025.
- [112] R. V. Hoffman, *Acidity and Basicity*, John Wiley & Sons, Ltd, 2005, pp. 47–68.
- [113] C. Antoine, *C. R. Acad. Sci.*, 1888, **107**, 681, 778, 836.
- [114] NIST, *Acetone*, <https://webbook.nist.gov/cgi/cbook.cgi?ID=C67641&Units=SI&Mask=4&Type=ANTOINE&Plot=on#ANTOINE>.
- [115] D. Ambrose, C. H. S. Sprake and R. Townsend, *J. Chem. Thermodyn.*, 1974, **6**, 693.

- [116] NIST, *Methylamine*, <https://webbook.nist.gov/cgi/cbook.cgi?ID=C74895&Mask=4&Type=ANTOINE&Plot=on#ref-1>.
- [117] J. G. Aston, C. W. Siller and G. H. Messerly, *J. Am. Chem. Soc.*, 1937, **59**, 1743.
- [118] R. Wang, J. Xue, K.-L. Wang, Z.-K. Wang, Y. Luo, D. Fenning, G. Xu, S. Nuryyeva, T. Huang, Y. Zhao, J. L. Yang, J. Zhu, M. Wang, S. Tan, I. Yavuz, K. N. Houk and Y. Yang, *Science*, 2019, **366**, 1509.
- [119] L. Iagher and L. Etgar, *ACS Energy Lett.*, 2018, **3**, 366.
- [120] X. Zhang, X. Ren, B. Liu, R. Munir, X. Zhu, D. Yang, J. Li, Y. Liu, D.-M. Smilgies, R. Li, Z. Yang, T. Niu, X. Wang, A. Amassian, K. Zhao and S. F. Liu, *Energy Environ. Sci.*, 2017, **10**, 2095.
- [121] X. Yu, Y. Qin and Q. Peng, *J. Phys. Chem. A*, 2017, **121**, 1169.
- [122] D. P. Nenon, J. A. Christians, L. M. Wheeler, J. L. Blackburn, E. M. Sanehira, B. Dou, M. L. Olsen, K. Zhu, J. J. Berry and J. M. Luther, *Energy Environ. Sci.*, 2016, **9**, 2072.
- [123] Y.-R. Jo, J. Tersoff, M.-W. Kim, J. Kim and B.-J. Kim, *ACS Cent. Sci.*, 2020, 959.
- [124] M. M. Cerda, J. L. Mancuso, E. J. Mullen, C. H. Hendon and M. D. Pluth, *Use of Dithiasuccinoyl-Caged Amines Enables COS/H<sub>2</sub>S Release Lacking Electrophilic Byproducts*, 2020, <https://chemistry-europe.onlinelibrary.wiley.com/doi/full/10.1002/chem.201905577>.
- [125] M. E. Foster, K. Sohlberg, C. D. Spataru and M. D. Allendorf, *J. Phys. Chem. C*, 2016, **120**, 15001.
- [126] G. Skorupskii, B. A. Trump, T. W. Kasel, C. M. Brown, C. H. Hendon and M. Dincă, *Nat. Chem.*, 2020, **12**, 131.
- [127] A. M. Ganose, S. Matsumoto, J. Buckeridge and D. O. Scanlon, *Chem. Mater.*, 2018, **30**, 3827.
- [128] C. G. Van de Walle, *Phys. Rev. Lett.*, 2000, **85**, 1012.
- [129] G. Kresse and J. Hafner, *Phys. Rev. B*, 1993, **47**, 558.
- [130] G. Kresse and J. Hafner, *Phys. Rev. B*, 1994, **49**, 14251.

- [131] G. Kresse and J. Furthmüller, *Phys. Rev. B*, 1996, **54**, 11169.
- [132] G. Kresse and J. Furthmüller, *Comput. Mater. Sci.*, 1996, **6**, 15.
- [133] M. J. Frisch, G. W. Trucks, H. B. Schlegel, G. E. Scuseria, M. A. Robb, J. R. Cheeseman, G. Scalmani, V. Barone, G. A. Petersson, H. Nakatsuji, X. Li, M. Caricato, A. V. Marenich, J. Bloino, B. G. Janesko, R. Gomperts, B. Mennucci, H. P. Hratchian, J. V. Ortiz, A. F. Izmaylov, J. L. Sonnenberg, D. Williams-Young, F. Ding, F. Lipparini, F. Egidi, J. Goings, B. Peng, A. Petrone, T. Henderson, D. Ranasinghe, V. G. Zakrzewski, J. Gao, N. Rega, G. Zheng, W. Liang, M. Hada, M. Ehara, K. Toyota, R. Fukuda, J. Hasegawa, M. Ishida, T. Nakajima, Y. Honda, O. Kitao, H. Nakai, T. Vreven, K. Throssell, J. A. Montgomery, Jr., J. E. Peralta, F. Ogliaro, M. J. Bearpark, J. J. Heyd, E. N. Brothers, K. N. Kudin, V. N. Staroverov, T. A. Keith, R. Kobayashi, J. Normand, K. Raghavachari, A. P. Rendell, J. C. Burant, S. S. Iyengar, J. Tomasi, M. Cossi, J. M. Millam, M. Klene, C. Adamo, R. Cammi, J. W. Ochterski, R. L. Martin, K. Morokuma, O. Farkas, J. B. Foresman and D. J. Fox, *Gaussian16 Revision B.01*, 2016, Gaussian Inc. Wallingford CT.
- [134] N. J. B. Green, *Quantum mechanics 1: Foundations*, Oxford University Press, 1997.
- [135] E. Schrödinger, *Phys. Rev.*, 1926, **28**, 1049.
- [136] P. Atkins and J. d. Paula, *Physical Chemistry: Thermodynamics, Structure, and Change*, W. H. Freeman and Company, New York, 10th edn., 2014.
- [137] M. Born and R. Oppenheimer, *Ann. Phys.*, 1927, **389**, 457.
- [138] D. R. Hartree, *Math. Proc. Cambridge Philos. Soc.*, 1928, **24**, 426.
- [139] V. Fock, *Phys.*, 1930, **61**, 126.
- [140] J. C. Slater, *Phys. Rev.*, 1930, **36**, 57.
- [141] P. Hohenberg and W. Kohn, *Phys. Rev.*, 1964, **136**, B864.
- [142] W. Kohn and L. J. Sham, *Phys. Rev.*, 1965, **140**, 1133.
- [143] J. P. Perdew and Y. Wang, *Phys. Rev. B*, 1992, **45**, 13244.
- [144] J. P. Perdew, K. Burke and M. Ernzerhof, *Phys. Rev. Lett.*, 1996, **77**, 3865.

- [145] J. P. Perdew, A. Ruzsinszky, G. I. Csonka, O. A. Vydrov, G. E. Scuseria, L. A. Constantin, X. Zhou and K. Burke, *Phys. Rev. Lett.*, 2008, **100**, 136406.
- [146] J. P. Perdew, J. A. Chevary, S. H. Vosko, K. A. Jackson, M. R. Pederson, D. J. Singh and C. Fiolhais, *Phys. Rev. B*, 1992, **46**, 6671.
- [147] J. Tao, J. P. Perdew, V. N. Staroverov and G. E. Scuseria, *Phys. Rev. Lett.*, 2003, **91**, 146401.
- [148] Y. Zhao and D. G. Truhlar, *Theor. Chem. Acc.*, 2008, **120**, 215.
- [149] M. Ernzerhof and G. E. Scuseria, *J. Chem. Phys.*, 1999, **110**, 5029.
- [150] J. Heyd, G. E. Scuseria and M. Ernzerhof, *J. Chem. Phys.*, 2003, **118**, 8207.
- [151] P. E. Blöchl, *Phys. Rev. B*, 1994, **50**, 17953.
- [152] F. Bloch, *Z. Phys.*, 1929, **52**, 555.
- [153] R. Hoffmann, *Solids and Surfaces: A Chemist's View of Bonding in Extended Structures*, Wiley-VCH, 1998.
- [154] M. I. Aroyo, D. Orobengoa, G. de la Flor, E. S. Tasci, J. M. Perez-Mato and H. Wondratschek, *Acta Crystallogr. A*, 2014, **70**, 126.
- [155] L. D. Whalley, J. M. Frost, B. J. Morgan and A. Walsh, *Phys. Rev. B*, 2019, **99**, 085207.
- [156] Y. Kang and S. Han, *Phys. Rev. Appl.*, 2018, **10**, 044013.
- [157] V. Ariel, *Effective Mass and Energy-Mass Relationship*, 2012,  
<http://arxiv.org/abs/1205.3995>.
- [158] S. Baroni, S. de Gironcoli, A. Dal Corso and P. Giannozzi, *Rev. Mod. Phys.*, 2001, **73**, 515.
- [159] H. Hellmann, *Einführung in die Quantenchemie*, Leipzig : F. Deuticke, 1937.
- [160] R. P. Feynman, *Phys. Rev.*, 1939, **56**, 340.
- [161] D. J. Chadi and R. M. Martin, *Solid State Commun.*, 1976, **19**, 643.
- [162] H. Wendel and R. M. Martin, *Phys. Rev. B*, 1979, **19**, 5251.
- [163] M. T. Yin and M. L. Cohen, *Phys. Rev. B*, 1982, **26**, 3259.

- [164] A. Rahman, *Phys. Rev.*, 1964, **136**, A405.
- [165] R. W. Boyd, *Nonlinear Optics 3<sup>rd</sup> edition*, Academic Press as an imprint of Elsevier, 2008.
- [166] C. J. Cramer, *Essentials of Computational Chemistry: Theories and Models*, John Wiley & Sons, Ltd, 2nd edn., 2004.
- [167] M. Ferrero, M. Rérat, R. Orlando and R. Dovesi, *J. Chem. Phys.*, 2008, **128**, 014110.
- [168] M. Ferrero, M. Rérat, R. Orlando and R. Dovesi, *J. Comput. Chem.*, 2008, **29**, 1450.
- [169] R. Dovesi, V. R. Saunders, C. Roetti, R. Orlando, C. M. Zicovich-Wilson, F. Pascale, B. Civalleri, K. Doll, N. M. Harrison, I. J. Bush, P. D'Arco, M. Llunell, M. Causà, Y. Noël, L. Maschio, A. Erba, M. Rérat and S. Casassa, *CRYSTAL17 User's Manual*, University of Torino, Torino, 2017.
- [170] R. Dovesi, A. Erba, R. Orlando, C. M. Zicovich-Wilson, B. Civalleri, L. Maschio, M. Rérat, S. Casassa, J. Baima, S. Salustro and B. Kirtman, *WIREs Comput. Mol. Sci.*, 2018, **8**, e1360.
- [171] N. N. Greenwood and A. Earnshaw, *Chemistry of the Elements*, Butterworth-Heinemann, 2nd edn., 1997.
- [172] G. Kieslich, S. Sun and A. K. Cheetham, *Chem. Sci.*, 2015, **6**, 3430.
- [173] *Shannon Radii*, <http://abulafia.mt.ic.ac.uk/shannon/ptable.php>.
- [174] R. D. Shannon, *Acta Crystallogr. A*, 1976, **32**, 751.
- [175] W. Travis, E. Glover, H. Bronstein, D. Scanlon and R. Palgrave, *Chem. Sci.*, 2016, **7**, 4548.
- [176] S. Liu, F. Zheng, N. Z. Koocher, H. Takenaka, F. Wang and A. M. Rappe, *J. Phys. Chem. Lett.*, 2015, **6**, 693.
- [177] Y. Kutes, L. Ye, Y. Zhou, S. Pang, B. D. Huey and N. P. Padture, *J. Phys. Chem. Lett.*, 2014, **5**, 3335.

- [178] F. Brivio, J. M. Frost, J. M. Skelton, A. J. Jackson, O. J. Weber, M. T. Weller, A. R. Goñi, A. M. A. Leguy, P. R. F. Barnes and A. Walsh, *Phys. Rev. B*, 2015, **92**, 144308.
- [179] M. T. Weller, O. J. Weber, P. F. Henry, A. M. Di Pumpo and T. C. Hansen, *Chem. Commun. (Cambridge, U. K.)*, 2015, **51**, 4180.
- [180] C. H. Hendon, R. Xi Yang, L. A. Burton and A. Walsh, *J. Mater. Chem. A*, 2015, **3**, 9067.
- [181] C. N. Savory, A. Walsh and D. O. Scanlon, *ACS Energy Letters*, 2016, **1**, 949.
- [182] W. M. Lauer, *J. Am. Chem. Soc.*, 1960, **82**, 5259.
- [183] R. Breslow, J. T. Groves and G. Ryan, *J. Am. Chem. Soc.*, 1967, **89**, 5048.
- [184] R. C. Kerber and C.-M. Hsu, *J. Am. Chem. Soc.*, 1973, **95**, 3239.
- [185] D. C. Law, S. W. Tobey and R. West, *J. Org. Chem.*, 1973, **38**, 768.
- [186] Z.-I. Yoshida, S. Hirota and H. Ogoshi, *Spectrochim. Acta*, 1974, **30A**, 1105.
- [187] Z.-I. Yoshida, H. Ogoshi and S. Hirota, *Tetrahedron Lett.*, 1973, **11**, 869.
- [188] R. Breslow and J. T. Groves, *J. Am. Chem. Soc.*, 1970, **92**, 984.
- [189] T. L. Jacobs and W. F. Brill, *J. Am. Chem. Soc.*, 1953, **75**, 1314.
- [190] B. D. Kelly and T. H. Lambert, *J. Am. Chem. Soc.*, 2009, **131**, 13930.
- [191] C. M. Vanos and T. H. Lambert, *Angew. Chem. Int. Ed.*, 2011, **50**, 12222.
- [192] J. S. Bandar, A. Tanaset and T. H. Lambert, *Chem. - Eur. J.*, 2015, **21**, 7365.
- [193] Y. Jiang, J. L. Freyer, P. Cotanda, S. D. Brucks, K. L. Killops, J. S. Bandar, C. Torsitano, N. P. Balsara, T. H. Lambert and L. M. Campos, *Nat. Commun.*, 2015, **6**, 5950.
- [194] A. Binek, F. C. Hanusch, P. Docampo and T. Bein, *J. Phys. Chem. Lett.*, 2015, **6**, 1249.
- [195] C. C. Stoumpos, C. D. Malliakas and M. G. Kanatzidis, *Inorg. Chem.*, 2013, **52**, 9019.
- [196] C. Quarti, E. Mosconi and F. De Angelis, *Chem. Mater.*, 2014, **26**, 6557.

- [197] M. T. Weller, O. J. Weber, J. M. Frost and A. Walsh, *J. Phys. Chem. Lett.*, 2015, **6**, 3209.
- [198] F. Brivio, K. T. Butler, A. Walsh and M. van Schilfgaarde, *Phys. Rev. B*, 2014, **89**, 155204.
- [199] D. Yang, W. Ming, H. Shi, L. Zhang and M.-H. Du, *Chem. Mater.*, 2016, **28**, 4349.
- [200] A. Fonari and C. Sutton, <https://github.com/afonari/emc>, 2012, Accessed: 11/27/2017.
- [201] A. Togo and I. Tanaka, *Scr. Mater.*, 2015, **108**, 1.
- [202] X. Zheng, B. Chen, J. Dai, Y. Fang, Y. Bai, Y. Lin, H. Wei, X. C. Zeng and J. Huang, *Nat. Energy*, 2017, **2**, 17102.
- [203] L. Gao, I. Spanopoulos, W. Ke, S. Huang, I. Hadar, L. Chen, X. Li, G. Yang and M. G. Kanatzidis, *ACS Energy Lett.*, 2019, **4**, 1763.
- [204] S. Yang, S. Chen, E. Mosconi, Y. Fang, X. Xiao, C. Wang, Y. Zhou, Z. Yu, J. Zhao, Y. Gao, F. D. Angelis and J. Huang, *Science*, 2019, **365**, 473.
- [205] B.-w. Park, N. Kedem, M. Kulbak, D. Y. Lee, W. S. Yang, N. J. Jeon, J. Seo, G. Kim, K. J. Kim, T. J. Shin, G. Hodes, D. Cahen and S. I. Seok, *Nat. Commun.*, 2018, **9**, 1.
- [206] M. E. Kamminga, H.-H. Fang, M. R. Filip, F. Giustino, J. Baas, G. R. Blake, M. A. Loi and T. T. M. Palstra, *Chem. Mater.*, 2016, **28**, 4554.
- [207] M. Xiao, F. Huang, W. Huang, Y. Dkhissi, Y. Zhu, J. Etheridge, A. Gray-Weale, U. Bach, Y.-B. Cheng and L. Spiccia, *Angew. Chem. Int. Ed.*, 2014, **126**, 10056.
- [208] F. Finocchi, A. Barbier, J. Jupille and C. Noguera, *Phys. Rev. Lett.*, 2004, **92**, 136101.
- [209] A. J. Logsdail, D. O. Scanlon, C. R. A. Catlow and A. A. Sokol, *Phys. Rev. B*, 2014, **90**, 155106.
- [210] C. C. Stoumpos, D. H. Cao, D. J. Clark, J. Young, J. M. Rondinelli, J. I. Jang, J. T. Hupp and M. G. Kanatzidis, *Chem. Mater.*, 2016, **28**, 2852.
- [211] L. Zhao, R. A. Kerner, Z. Xiao, Y. L. Lin, K. M. Lee, J. Schwartz and B. P. Rand, *ACS Energy Lett.*, 2016, **1**, 595.

- [212] V. K. Ravi, G. B. Markad and A. Nag, *ACS Energy Lett.*, 2016, **1**, 665.
- [213] Y. C. Kim, N. J. Jeon, J. H. Noh, W. S. Yang, J. Seo, J. S. Yun, A. Ho-Baillie, S. Huang, M. A. Green, J. Seidel, T. K. Ahn and S. I. Seok, *Adv. Energy Mater.*, 2016, **6**, 1502104.
- [214] T. J. Jacobsson, J.-P. Correa-Baena, E. Halvani Anaraki, B. Philippe, S. D. Stranks, M. E. F. Bouduban, W. Tress, K. Schenk, J. Teuscher, J.-E. Moser, H. Rensmo and A. Hagfeldt, *J. Am. Chem. Soc.*, 2016, **138**, 10331.
- [215] F. Liu, Q. Dong, M. K. Wong, A. B. Djurišić, A. Ng, Z. Ren, Q. Shen, C. Surya, W. K. Chan, J. Wang, A. M. C. Ng, C. Liao, H. Li, K. Shih, C. Wei, H. Su and J. Dai, *Adv. Energy Mater.*, 2016, **6**, 1502206.
- [216] T. P. Gujar, T. Unger, A. Schönleber, M. Fried, F. Panzer, S. v. Smaalen, A. Köhler and M. Thelakkat, *Phys. Chem. Chem. Phys.*, 2017, **20**, 605.
- [217] A. Sashchiuk, L. Langof, R. Chaim and E. Lifshitz, *J. Cryst. Growth*, 2002, **240**, 431.
- [218] M. Brumer, A. Kigel, L. Amirav, A. Sashchiuk, O. Solomesch, N. Tessler and E. Lifshitz, *Adv. Funct. Mater.*, 2005, **15**, 1111.
- [219] E. Lifshitz, M. Brumer, A. Kigel, A. Sashchiuk, M. Bashouti, M. Sirota, E. Galun, Z. Burshtein, A. Q. Le Quang, I. Ledoux-Rak and J. Zyss, *J. Phys. Chem. B*, 2006, **110**, 25356.
- [220] J. Heyd, G. E. Scuseria and M. Ernzerhof, *J. Chem. Phys.*, 2006, **124**, 219906.
- [221] S. Steiner, S. Khmelevskyi, M. Marsmann and G. Kresse, *Phys. Rev. B*, 2016, **93**, 224425.
- [222] N. Shuichi, *J. Chem. Phys.*, 1984, **81**, 511.
- [223] N. Shuichi, *Prog. Theor. Phys. Suppl.*, 1991, **103**, 1.
- [224] D. M. Bylander and L. Kleinman, *Phys. Rev. B*, 1992, **46**, 13756.
- [225] H.-Y. Ye, Y.-Y. Tang, P.-F. Li, W.-Q. Liao, J.-X. Gao, X.-N. Hua, H. Cai, P.-P. Shi, Y.-M. You and R.-G. Xiong, *Science*, 2018, **361**, 151.
- [226] P. A. Franken, A. E. Hill, C. W. Peters and G. Weinreich, *Phys. Rev. Lett.*, 1961, **7**, 118.

- [227] G. D. Stucky, M. L. F. Phillips and T. E. Gier, *Chem. Mater.*, 1989, **1**, 492.
- [228] D. F. Eaton, *Science*, 1991, **253**, 281.
- [229] J. L. Brédas, C. Adant, P. Tackx, A. Persoons and B. M. Pierce, *Chem. Rev.*, 1994, **94**, 243.
- [230] P. S. Halasyamani and K. R. Poeppelmeier, *Chem. Mater.*, 1998, **10**, 2753.
- [231] T. Schneider, *Nonlinear Optics in Telecommunications*, Springer Berlin Heidelberg, 2004.
- [232] H. Wu, H. Yu, Z. Yang, X. Hou, X. Su, S. Pan, K. R. Poeppelmeier and J. M. Rondinelli, *J. Am. Chem. Soc.*, 2013, **135**, 4215.
- [233] J. M. Rondinelli and E. Kioupakis, *Annu. Rev. Mater. Res.*, 2015, **45**, 491.
- [234] T. T. Tran, H. Yu, J. M. Rondinelli, K. R. Poeppelmeier and P. S. Halasyamani, *Chem. Mater.*, 2016, **28**, 5238.
- [235] P. S. Halasyamani and J. M. Rondinelli, *Nat. Commun.*, 2018, **9**, 2972.
- [236] D. Cyranoski, *Nature*, 2009, **457**, 953.
- [237] *Niobium Price*, <https://www.metalary.com/niobium-price>.
- [238] E. A. Olivetti, G. Ceder, G. G. Gaustad and X. Fu, *Joule*, 2017, **1**, 229.
- [239] G. B. Olson, *Science*, 2000, **288**, 993.
- [240] I. Chung and M. G. Kanatzidis, *Chem. Mater.*, 2013, **26**, 849.
- [241] N. R. Goud, X. Zhang, J.-L. Brédas, V. Coropceanu and A. J. Matzger, *Chem*, 2018, **4**, 150.
- [242] A. P. Wilkinson, A. K. Cheetham and R. H. Jarman, *J. Appl. Phys.*, 1993, **74**, 3080.
- [243] J. Zyss, D. S. Chemla and J. F. Nicoud, *J. Chem. Phys.*, 1981, **74**, 4800.
- [244] P. N. Prasad and D. J. Williams, *Introduction to Nonlinear Optical Effects in Molecules and Polymers 1<sup>st</sup> Edition*, John Wiley & Sons, 1991.
- [245] T. Kaino and S. Tomaru, *Adv. Mater.*, 1993, **5**, 172.

- [246] F. Pan, G. Knöpfle, C. Bosshard, S. Follonier, R. Spreiter, M. S. Wong and P. Günter, *Appl. Phys. Lett.*, 1996, **69**, 13.
- [247] I. D. L. Albert, T. J. Marks and M. A. Ratner, *J. Am. Chem. Soc.*, 1998, **120**, 11174.
- [248] M.-h. Jiang and Q. Fang, *Adv. Mater.*, 1999, **11**, 1147.
- [249] W.-J. Kuo, G.-H. Hsiue and R.-J. Jeng, *Macromolecules*, 2001, **34**, 2373.
- [250] C. Bosshard, R. Spreiter, L. Degiorgi and P. Günter, *Phys. Rev. B*, 2002, **66**, 205107.
- [251] O. R. Evans and W. Lin, *Acc. Chem. Res.*, 2002, **35**, 511.
- [252] S. R. Marder, *Chem. Commun.*, 2006, 131.
- [253] C. Wang, T. Zhang and W. Lin, *Chem. Rev.*, 2011, **112**, 1084.
- [254] H. Wu, S. Pan, K. R. Poeppelmeier, H. Li, D. Jia, Z. Chen, X. Fan, Y. Yang, J. M. Rondinelli and H. Luo, *J. Am. Chem. Soc.*, 2011, **133**, 7786.
- [255] M. Veithen and P. Ghosez, *Phys. Rev. B*, 2002, **65**, 214302.
- [256] W. Zhang, H. Yu, H. Wu and P. S. Halasyamani, *Chem. Mater.*, 2017, **29**, 2655.
- [257] J. Zyss and I. Ledoux, *Chem. Rev.*, 1994, **94**, 77.
- [258] G. A. Magel, M. M. Fejer and R. L. Byer, *Appl. Phys. Lett.*, 1990, **56**, 108.
- [259] Z. Lin, X. Jiang, L. Kang, P. Gong, S. Luo and M.-H. Lee, *J. Phys. D: Appl. Phys.*, 2014, **47**, 253001.
- [260] D. N. Nikogosyan, *Properties of Optical and Laser-Related Materials*, Wiley-Blackwell, 1997.
- [261] H. Wang, H. Liu, Z. Zhang, Z. Liu, Z. Lv, T. Li, W. Ju, H. Li, X. Cai and H. Han, *npj Comput. Mater.*, 2019, **5**, 17.
- [262] K. T. Butler, J. M. Frost and A. Walsh, *Mater. Horiz.*, 2015, **2**, 228.
- [263] T. Yamada, I. Aoki, H. Miki, C. Yamada and A. Otomo, *Mater. Chem. Phys.*, 2013, **139**, 699.
- [264] <https://www.tcichemicals.com/pdf/FF051E.pdf>.

- [265] K. T. Butler, *J. Mater. Chem. C*, 2018, **6**, 12045.
- [266] G. Kieslich, J. M. Skelton, J. Armstrong, Y. Wu, F. Wei, K. L. Svane, A. Walsh and K. T. Butler, *Chem. Mater.*, 2018, **30**, 8782.
- [267] S. Grimme, J. Antony, S. Ehrlich and H. Krieg, *J. Chem. Phys.*, 2010, **132**, 154104.
- [268] G. Kresse and D. Joubert, *Phys. Rev. B*, 1999, **59**, 1758.
- [269] V. Lacivita, M. Rérat, B. Kirtman, M. Ferrero, R. Orlando and R. Dovesi, *J. Chem. Phys.*, 2009, **131**, 204509.
- [270] C. Adamo and V. Barone, *J. Chem. Phys.*, 1999, **110**, 6158.
- [271] M. F. Peintinger, D. V. Oliveira and T. Bredow, *J. Comput. Chem.*, 2012, **34**, 451.
- [272] J. Laun, D. V. Oliveira and T. Bredow, *J. Comput. Chem.*, 2018, **39**, 1285.
- [273] <http://www.tc.uni-koeln.de/PP/clickpse.en.html>.